Highly Efficient and Data Compressed Ultrafast Single-Pixel Imaging based on Photonic Time-Stretch

A Thesis Submitted to The University of Kent for the Degree of Doctor of Philosophy in Electronic Engineering

By

Guoqing Wang

June, 2018

ABSTRACT

The research presented in this thesis is focused on highly efficient and data compressed ultrafast single pixel imaging (SPI) systems based on photonic time stretch (PTS) technique. Three ultrafast SPI systems are presented and analysed with unique features of low-cost, compact, highly efficient and optical data compression.

The first ultrafast SPI system is a highly efficient, fibre-compatible ultrafast imaging system based on PTS using a 45° tilted fibre grating (45° TFG). The 45° TFG serves as an in-fibre lateral diffraction element, replacing bulky and lossy free-space diffraction gratings in conventional PTS imaging systems. This new design significantly reduces the volume of conventional PTS imaging systems, improves energy efficiency and system stability. A proof-of-principle demonstration of our proposed PTS imaging system is performed for the first time with improved spatial resolution and ultrafast detecting speed of 46 m/s.

Secondly, data compressed ultrafast photonic time stretch imaging is investigated with the help of a spatial mask for spatial domain compressed sensing. In practice, a spatial light modulator (SLM) is utilized as a passive optical random pattern modulator, namely, spatial mask, in spatial domain. This combines the benefit of compressed sensing (CS) and PTS techniques. And a high speed CS imaging system is obtained with a compression ratio of 55.6%. Besides, time-domain CS applied in ultrafast real-time optical coherent tomography (OCT) is experimentally demonstrated as well.

Finally, an all-optical CS imaging system based on PTS and multimode interference using a multimode fibre (MMF) is demonstrated. The MMF acts as a low-cost random optical speckle pattern generator based on ultrafast wavelength tuning in PTS. Each wavelength of the optical light generates a repeatable and stable random optical speckle pattern, which has the feature of low-correlated relation between different optical speckle patterns. This technique can overcome the speed limit in existing CS photonic time stretch imaging, where imaging speed is much lower than the pulse repetition rate.

ACKNOWLEDGEMENT

I owe much gratitude to my principal supervisor Dr. Chao Wang for his support, instructions, priceless advices and suggestions throughout my Ph.D., his standard of high quality research work enlightened and pushed me to perform best and achieve best throughputs.

I would like to thank my supervisor Prof Nathan Gomes for his valuable, constructive and insightful comments and contributions. His suggestions greatly helped and improved the quality of this thesis.

I would like to thank our cooperated groups from different universities, especially Prof Lin Zhang from Aston University, Dr Zhijun Yan from Huazhong University of Science and Technology, Dr Lei Su from Queen Mary University of London, and Dr Stuart Gibson, Mr Fangliang Bai, Prof Adrian Podoleanu, Dr Manuel Marques from School of Physics Science, University of Kent.

I would also like to thank the visiting teachers in our group, Dr Dejun Feng, Dr Shenggui Fu, Dr Xin Liu, Dr Lei Yang and Dr Xiaojuan Liu, who gave me a lot of suggestions and contributed my research.

My gratitude goes to Mr Chaitanya Mididoddi, Mr Eamonn Ahmad and Mr Usman Habib for the cooperated work, which contributed my research a lot. I would also like to thank Dr Antony Aighobahi, Miss Shabnam Noor for the useful discussions and sharing of laboratory equipment.

My gratitude goes to all staff in the School of Engineering and Digital Arts and in particular Yan Zhang, Edwin Lui, Simon Jakes and Frankie Powers for their help throughout my research.

Finally, I would like to show my greatest love to my parents and siblings for their support, understanding, and encouragement throughout my years of study.

CONTENTS

LIST OF PUBLICATIONS

Peer review articles:

[1] **Guoqing Wang**, Chao Wang, Zhijun Yan, Lin Zhang, Lei Yang, Improved Resolution Optical Time Stretch Imaging Based on High Efficiency In-Fibre Diffraction, *Scientific Reports*, vol. 8, no. 600, pp. 1-9, 2018.

[2] **Guoqing Wang**, Usman Habib, Zhijun Yan, Nathan Gomes, Qingmei Sui, Junbo Wang, Lin Zhang, Chao Wang. Highly Efficient Optical Beam Steering Using an In-Fibre Diffraction Grating for Full Duplex Indoor Optical Wireless Communication, *Journal of Lightwave Technology*, accepted (DOI: 10.1109/ JLT.2018.2832200).

[3] **Guoqing Wang**, Chao Wang, Zhijun Yan and Lin. Zhang. Highly efficient spectrally encoded imaging using a 45° tilted fibre grating, Optics Letters, vol. 41, no. 11, pp. 2398-2401, 2016.

[4] Chaitanya K. Mididoddi, Fangliang Bai, **Guoqing Wang**, Jinchao Liu, Stuart Gibson, and Chao Wang, High Throughput Photonic Time Stretch Optical Coherence Tomography with Data Compression, IEEE Photonics Journal, vol. pp, no. 99, 2017.

Conferences:

[1] Chaitanya K Mididoddi, **Guoqing Wang**, Chao Wang. Ultrafast single-pixel optical imaging based on multimode interference and compressed sensing, 2018 SPIE Photonics Europe, 22-26 Apr. 2018, Strasbourg, France.

[2] **Guoqing Wang**, Usman Habib, Chao Wang, Nathan Gomes, Zhijun Yan, Lin Zhang. In-Fibre Diffraction Grating Based Beam Steering for Full Duplex Optical Wireless Communication, MWP 2017, China.

[3] Chaitanya K Mididoddi, **Guoqing Wang**, Lei Su, Chao Wang, Photonic Time-Stretch Optical Coherence Tomography With Data Compression And Improved Resolution, CLEO-PR, OECC and PGC 2017, 31 July- 4 Aug 2017, Singapore.

[4] Qin Huabao, Yan Zhijun, Sun Qizhen, **Guoqing Wang**, Chao Wang, Liu Deming, Zhang Lin, Theoretical Analysis Of Diffraction Grating Based On 45°-tilted Fibre Gratings, CLEO-PR, OECC and PGC 2017, 31 July- 4 Aug 2017, Singapore.

[5] **Guoqing Wang**, Usman Habib, Chao Wang, Nathan Gomes, Zhijun Yan, Lin Zhang. Beam Steering for Free-Space Indoor Optical Wireless Transmission Using in-Fibre Diffraction Grating. Conference on Lasers and Electro-Optics (CLEO) 2017, paper SF1L.5, 14-19 May 2017, San Jose, California, USA.

[6] **Guoqing Wang**, Chao Wang. Diffraction Limited Optical Time-Stretch Microscopy Using an In-Fibre Diffraction Grating. OSA 2016 Frontiers in Optics/Laser Science, **Postdeadline paper**, FF2A.5, 17-21 Oct 2016, Rochester, USA.

[7] Chaitanya K Mididoddi, **Guoqing Wang**, and Chao Wang. Data Compressed Real-Time Optical Coherence Tomography. 2016 IEEE Photonics Conference (IPC), 2-6 Oct 2016, Waikoloa, Hawaii, USA.

[8] **Guoqing Wang**, Chao Wang, Zhijun Yan and Lin. Zhang. A fibre-compatible spectrally encoded imaging system using a 45° tilted fibre grating, 2016 SPIE Photonics Europe, Proc. SPIE 9896, 98960J, 3-7 Apr. 2016, Brussels, Belgium.

LIST OF ABBREVIATIONS

1D	1 Dimensional
2D	2 Dimensional
2D	3 Dimensional
4G	Fourth generation of wireless communications
5G	Fifth generation of wireless communications
ASE	Amplified spontaneous emission
AST	Anamorphic stretch transformation
AWG	Arbitrary waveform generator
AWG	Arrayed waveguide grating
BER	Bits Error Rate
BP	Beam profiler
bps	Bit per second
BW	Bandwidth
CCD	Charge-coupled device
CFBG	Chirped fibre Bragg grating
CM	Collimator matrix
CMOS	Complementary metal-oxide-semiconductor
CP	Cyclic prefix
CS	Compressed sensing
CW	Continuous-wave
DAC	Digital-to-analogue converters
dB	decibel
DFB	Distributed feedback
DCF	Dispersive compensating fibre
DFB	Distributed Feedback
DFT	Dispersive Fourier transform
DMD	Digital micromirror devices
EDFA	Erbium-doped fibre amplifier
EVM	Error vector magnitude
Ex-TFG	Excessively tilted fibre grating

FBG	Fibre Bragg grating
FFT	Fast Fourier transform
FOV	Field-of-view
F-P	Fabry - Perot
FST	Free-space transmission
FTTH	Fibre-to-the-home
FWHM	Full-width at half maximum
Gbps	Gigabits per second
GHz	Gigahertz
GVD	Group velocity dispersion
IEEE	Institute of Electrical and Electronics Engineers
IF	Intermediate frequency
IFFT	Inverse fast Fourier transform
KHz	Kilohertz
LED	Light emitting diode
LPFG	Long period fibre grating
Mbps	Megabits per second
MHz	Megahertz
MLL	Mode-locked-laser
MMF	Multimode fibre
mW	Mili-Watt
MZM	Mach-Zehnder modulator
MZI	Mach-Zehnder Interferometry
NA	Numerical aperture
nm	Nano-metre
OCT	Optical coherence tomography
OFDM	Orthogonal Frequency Division Multiplexing
OPD	Optical path difference
OSA	Optical society of America
OSA	Optical spectrum analyser
PC	Personal computer
PC	Polarization controller

PD	Photo-detector
PDM	Polarization-division multiplexing
PDL	Polarization dependent loss
PM	Phase modulator
PolM	Polarization modulator
PPG	Pulse pattern generator
PRBS	Pseudorandom bit sequence
PSF	Point spread function
PTS	Photonic time-stretch
QAM	Quadrature amplitude modulation
RDG	Random data generator
RF	Radio frequency
RFA	Radio frequency amplifier
RTFG	Radially tilted fibre grating
RFSG	Radio frequency signal generator
SEI	Spectrally encoded imaging
SETS	Spectrally encoded and time encoded
SLM	Spatial light modulator
SMF	Single-mode fibre
SNR	Signal-to-noise ratio
SPA	Stationary-phase-approximation
SPI	Single-pixel imaging
SRI	Surrounding refraction index
STEAM	Serial time-encoded amplified microscopy
TFG	Tilted fibre grating
TFBG	Tilted fibre Bragg grating
TL	Tunable laser
VIPA	Virtually imaged phased array
VLC	Visible light communication
WSL	Wavelength swept laser

LIST OF FIGURES

CHAPTER 1: INTRODUCTION

1.1. Background

Single-pixel imaging (SPI) is an emerging imaging paradigm that allows images to be detected via using a single point detector, and has received drastically increasing attentions in recent years [1]. Conventional SPI has obtained widely applications in optical coherence tomography [2], confocal optical microscopy [3], tomographic terahertz imaging [4] and ghost imaging [5] at visible/infrared wavelengths.

SPI has the advantages of low-cost imaging systematic infrastructure, which uses a single pixel detector instead of expensive cameras. This allows it applied extensively in low light conditions. Also, SPI is combined with compressed sensing (CS) and / or photonic time-stretch (PTS) to achieve better performance with the purpose of data compression and ultrafast imaging, these techniques enhanced the applications of SPI scheme in terms of efficiency, imaging quality and imaging speed.

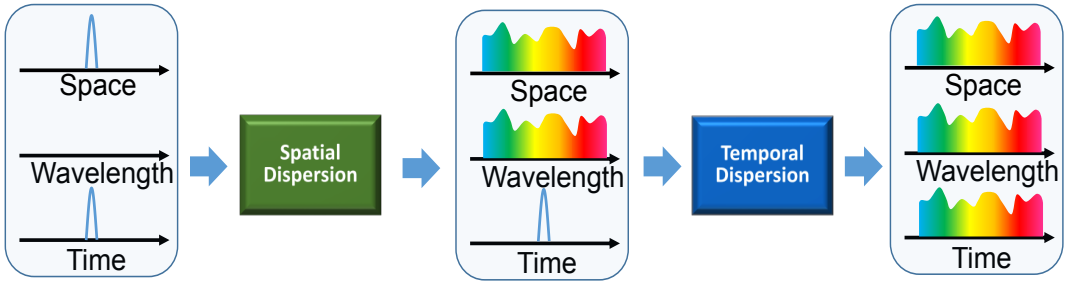

Figure 1.1 One of the most popular traditional ultrafast SPI system with space to wavelength conversion and wavelength to time conversion [6].

Compared to conventional imaging systems using charge-coupled device (CCD) or complementary metal-oxide-semiconductor (CMOS), which can achieve at a maximum speed of 40MHz [7], ultrafast SPI systems based on PTS can easily demonstrate with a frame rate of tens of hundreds of MHz or even tens of GHz [8–

12]. Besides, the ultrafast SPI draws extensive attention due to its advantage of enabling images acquiring with a single point detector [6,13–17] at a low-cost.

Figure 1.1 shows one of the most popular traditional ultrafast SPI systems, which has two steps: space to wavelength conversion and wavelength to time conversion. First of all, the imaging information in the spatial domain has to be encoded to optical light wavelength domain via a spatial disperser, which can perform uniform one-to-one mapping between the space and wavelength. Then, the converted wavelength information is further converted into time domain via a temporal disperser, which has the feature of uniform one-to-one mapping between wavelength and time. Thus, uniform one-to-one mapping between space and time is obtained, and the spatial imaging information can be detected in temporal domain, and a single-pixel photo-detector (PD) can be applied for imaging. Note in this system the sequence of two steps can be reversed.

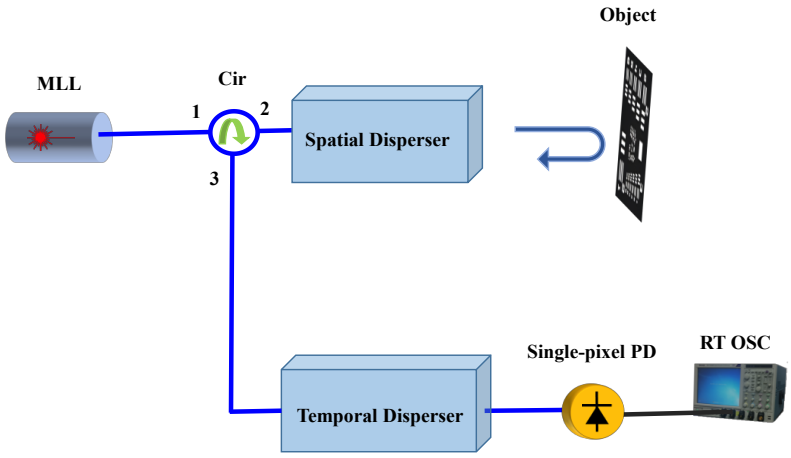

Figure 1.2 Ultrafast SPI system based on spatial disperser and temporal disperser.

Figure 1.2 illustrates the ultrafast SPI system based on spatial disperser and temporal disperser. An optical pulse with broadband spectrum from mode-locked laser (MLL) will propagate into the spatial disperser after circulator. The spatial disperser is one kind of diffractive optical elements, such as commonly used diffraction grating for 1dimonsional (1D) imaging [18] and virtually imaged phased array (VIPA) for 1dimonsional (2D) imaging [19]. Uniform one-to-one mapping between spectrum and space is obtained in spatial disperser. When the pulse is reflected by the object (note the system can also work in transmission

mode, i.e. light transmitted through the object), image information in spatial domain is mapped into spectrum domain. After transmitted through the temporal disperser, uniform one-to-one mapping between the spectrum and time is achieved via the application of dispersive compensating fibre (DCF). Thus, the imaging information in the spatial domain is converted into temporal waveform in time domain. A single-pixel PD is utilized to detect the temporal waveform and followed by a real-time oscilloscope to receive the signal. Also, in such a system the order of spatial disperser and temporal disperser can be reversed.

Nowadays several of ultrafast optical imaging methods using the PTS technique were proposed and implemented. In early stage, such as in [20], an ultrafast displacement sensing and barcode reading experiment was demonstrated; a hybrid dispersion laser scanner [6] was presented with applications of high-speed surface 3 dimensional (3D) vibrometry and flow cytometry using the technology named serial time-encoded amplified microscopy (STEAM); In [16,21], STEAM was applied with the ultrafast measurement of dynamic phenomena, such as ultrafast imaging, laser ablation and microfluidics for medical applications. Recently, more and more techniques were combined with PTS based ultrafast SPI systems. Structured illumination [22] was cooperated to improve the resolution of the imaging system. CS [23] method was applied to solve the big data issue with the utilization of passive pattern. In order to replace the expensive mode-locked laser, an amplified spontaneous emission (ASE) source with Fabry - Perot (F-P) filter and Mach - Zehnder modulator (MZM) were applied [24]. In [25], distributed feedback (DFB) laser array consists of lasers of varied wavelengths, arrayed waveguide grating (AWG) and MZM are used to replace the mode-locked laser. In order to detect the transparent imaging object, STEAM with interferometric structure was employed in [26]. Another method of detecting of transparent object was achieved via using Nomarski prism in STEAM [27]. Also, ultrafast surface imaging based polarization-division multiplexing (PDM) and STEAM was presented in [28] with enhanced spatial resolution. Another phase-shifting method based on STEAM was proposed in [29] with the application of ultrafast imaging detection. These imaging techniques have widely been applied in the biomedical applications, such as flow cytometry.

1.2. Challenges and aims

With the development of ultrafast SPI technique, fast imaging speed is achieved along with the disadvantages of more complexed system [24,25], lower optical/energy efficiency, and most of all, expensive devices, larger volume / weight [17,28].

Many of the techniques focus on how to make the PTS based ultrafast SPI system with fast imaging speed [30], more dimensional detection or observation with multiplexing methods [28]. However, the current methods haven't been combined the features of low-cost and energy efficient, and high stability with reduced volume and weight for proposed system.

Currently, there are two challenges. Challenge one: in order to perform the uniform one-to-one mapping between spectrum/wavelength and space, bulky diffraction gratings in imaging systems [15–17,22–24] are applied, which leads to a few problems. The usage of bulky diffraction gratings has the drawback of high cost and high insert loss of optical light due to its intrinsic diffraction nature and the light coupling between the fibre and open space. Also, it increases the difficulty of deploying imaging system and limits the potential practical applications where portability and low cost are required. However, few new devices, which potentially could simplify the existing imaging systems with high efficiency, low cost, high stability and compact size or light weight, have been applied or reported in the PTS based ultrafast SPI systems. Challenge two: large amount of data needs to be processed at unprecedented speed owing to the ultrafast speed of PTS based ultrafast SPI systems. Great pressure on the hardware when considering processing such large amount of data in limited time. As a result, data compressing methods are need to be applied in ultrafast imaging methods.

Based on the challenge of the research, the aims of this thesis are mainly classified into two categories. One aim is to improve the efficiency and reduce the volume and cost of conventional ultrafast SPI system, simplify the system and improve the stability of the system via using new devices. To achieve this aim, a titled in-fibre grating is applied as the objective. By the utilisation of in-fibre grating, the

enhanced efficiency and miniature size of ultrafast imaging system can be obtained. The other aim is to tackle with the large amount of data, namely, big data issue, that is induced by the PTS based imaging systems for real-time ultrafast imaging information detection and corresponding data processing. The objective to achieve this aim is via the application of the CS method, which reduces the volume of data that are detected by PD and are acquired by data acquisition card, and reduces the cost of the system via using low-cost slow speed PDs and low bandwidth data acquisition cards.

1.3. Contributions of this Thesis

The distinct contributions of this thesis include:

- A novel highly efficient and fibre compatible PTS based ultrafast SPI system using a 45° tilted fibre grating (45° TFG) is presented for the first time. The 45° TFG, which could reduce the volume and high light insert loss via replacing the traditional bulky grating, is utilised as the in-fibre diffractive grating device. The imaging system that using 45° TFG has the benefit of compact size, highly efficient and low light loss via eliminating the optical light insert loss between the fibre and open space. This new proposal could greatly reduce volume, enhance the efficiency and stability of the imaging system. The 45° TFG is for the first time experimentally demonstrated in the SPI system and an ultrafast unprecedented imaging speed of 46m/s is performed. Also, the 45° TFG can be regarded as a highly efficient beam steering device. Two free-space optical wireless communication systems using the 45° TFG are experimentally demonstrated with a data rate of 9.6 Gbps per wavelength/beam using 2.4 GHz bandwidth signals at a transmission range of 1.4m.

- To tackle the big data issue in the traditional ultrafast SPI system, a CS method is presented. A CS system using passive optical random mask based traditional STEAM structure is experimentally demonstrated. The spatial light modulator (SLM) here is acted as a passive random mask in spatial domain, which

potentially could increase the CS imaging speed when combined with galvometer. Note the passive random mask is not limited to SLM, the SLM here is only acted as an example. This proposal combines the benefit of CS and PTS techniques in the ultrafast SPI system, reducing the volume of the data that need to be processed. A proof-of-principle experimental results show a high speed CS imaging system with a data compression ratio of 55.6%.

- A new low cost ultrafast SPI system combined PTS and CS techniques using multimode fibre (MMF) is presented in simulation and experiment. This proposal reduces the volume of massive data. When a beam of light is transmitted through a single capsuled MMF, different wavelengths of the optical light will induce different, repeatable and random optical speckle patterns, which have low correlation and experimentally confirmed suitable for the CS method. Thus the MMF can be regarded as an all-optical random speckle pattern generator with the benefit of low cost while maintaining high bandwidth / ultrafast speed. With the utilization of PTS, ultrafast SPI system is performed using CS method. In simulation, a 27 × 27 pixels image is reconstructed with 500 measurements (a compression ratio of 68.59%). Besides, the image resolution of the proposed SPI system is analysed, and the result is 42 × 42 pixels when considering the random optical speckle patterns utilised in the experiment. Also, a proposal combines the CS and PTS techniques is applied in optical coherent tomography (OCT) and experimentally demonstrated.

1.4. Thesis Outline

Chapter 2 presents a detailed background research of PTS based ultrafast SPI system with varied techniques applied in the ultrafast imaging systems. First, the principle of STEAM is introduced. The STEAM contains two steps: space to spectrum/wavelength conversion and time to spectrum/wavelength conversion. In addition, different types of tilted fibre gratings are introduced and analysed, and their performances and applications are stated. Furthermore, the literature review of MMF is presented with different types and modes analysis of MMF, as well as its

application for imaging and communications. Finally, the CS method is introduced, and the benefit, fulfilment and applications of the CS method are stated.

Chapter 3 presents the 45° TFG for PTS based ultrafast SPI systems and indoor free-space optical wireless communication. The theoretical and experimental analysis of the 45° TFG is presented in imaging applications. A spatial resolution improved highly efficient SPI system based on the 45° TFG is performed. The PTS based ultrafast SPI system using the 45° TFG is obtained with an unprecedented imaging speed. Also, a 45° TFG is exploited in the free-space optical wireless communication system as the beam steering device and a full-duplex bidirectional indoor free-space optical wireless communication system is experimentally demonstrated.

Chapter 4 states a CS method based STEAM structure using passive random optical mask to tackle the big data issue. The SLM is performed as one type of passive random optical masks in spatial domain. The presented system, which combines PTS and CS techniques using a SLM as the passive random optical mask, is experimentally demonstrated with a data compression rate of 55.6%. Also, an OCT system combined with PTS and CS techniques is experimentally demonstrated with a data compression rate of 66%.

Chapter 5 states an ultrafast SPI system with the combination of the CS and PTS techniques based on multimode interference using MMF. The MMF is acted as a low cost all-optical random speckle pattern generator. The performance of the proposed imaging system with different data compression ratio is computationally investigated. Besides, the pixel resolution, speckle correlation, speckle temporal stability and mode dispersion in MMF is analysed.

Chapter 6 presents the conclusions from the above investigations and potential proposals for the future research.

CHAPTER 2: BACKGROUND STUDY AND LITERATURE REVIEW

2.1. Introduction

In this Chapter, the most intensively utilized imaging system, namely STEAM, consists of two fundamental steps, which are uniform-one-to-one mapping between space and wavelength/spectrum and uniform-one-to-one mapping between wavelength/spectrum and time, is reviewed in principle and applications. A detail-stated background of optical devices, techniques and system structures in PTS based ultrafast SPI systems are presented, such as the in-fibre grating device is introduced with its various potential application fields. The resurging ultrafast SPI systems based on MMF using new techniques surmounting the disadvantage of instability and randomization of MMF is reviewed as a low cost CS ultrafast imaging configuration. Finally, the performance of data compression technique (CS and nonlinear time-stretch) in ultrafast imaging systems reported in previous works is reviewed (which has the advantage of addressing the improvement in data process, reducing the high volume of data that needs to be processed in the ultrafast SPI systems).

2.2. Photonics time stretch

Continuous ultrafast optical imaging, which allows new discoveries in science and engineering [13], at unprecedented speed of tens of million frames per second is invented with a great deal of attraction. This new type of imaging technology, also known as STEAM [16], overcomes fundamental trade-off between imaging speed and sensitivity in ultrafast imaging by combining the unique mapping from the spatial information (image) to a serial time-domain data stream via continuous broadband spectrum waveform using spatial and temporal dispersions, as well as low noise optical amplification and high-speed single-pixel detection (single point

detection). Two major indispensable steps are in STEAM, one is unique uniform one-to-one mapping between spatial information and continuous broadband spectrum waveform using spatial dispersion, the other is unique uniform one-to-one mapping between continuous broadband spectrum waveform and serial time-domain data stream using temporal dispersion. The theory of these two steps is stated below. In this thesis, the amplification part of STEAM is not introduced based on the implementation of our system.

2.2.1. Space to spectrum conversion

Space (spatial information) to spectrum (continuous broadband spectrum waveform) conversion, which maps transverse spatial coordinates of the object into wavelength of the illuminating light, is based on unique one-to-one mapping between space and optical wavelength. This unique one-to-one mapping is achieved by spatial dispersion using optical diffraction devices, such as a diffraction grating [18] for one dimensional imaging and the joint use of a virtually imaged phased array (VIPA) [19,31,32] and a diffraction grating for two dimensional (2D) imaging.

An imaging system based on space to spectrum conversion, is called spectrally encoded imaging (SEI) [33], which has attracted considerable research interest due to its features of wide options of illumination wavelength beyond visible light and a great number of resolvable points thanks to the broad spectral bandwidth of the light source and high angular dispersion of the diffraction element.

For 1D imaging, the most commonly used diffraction element is the bulky high groove density diffraction gratings due to their high angular dispersion. The investigation about diffraction gratings is presented in [34].

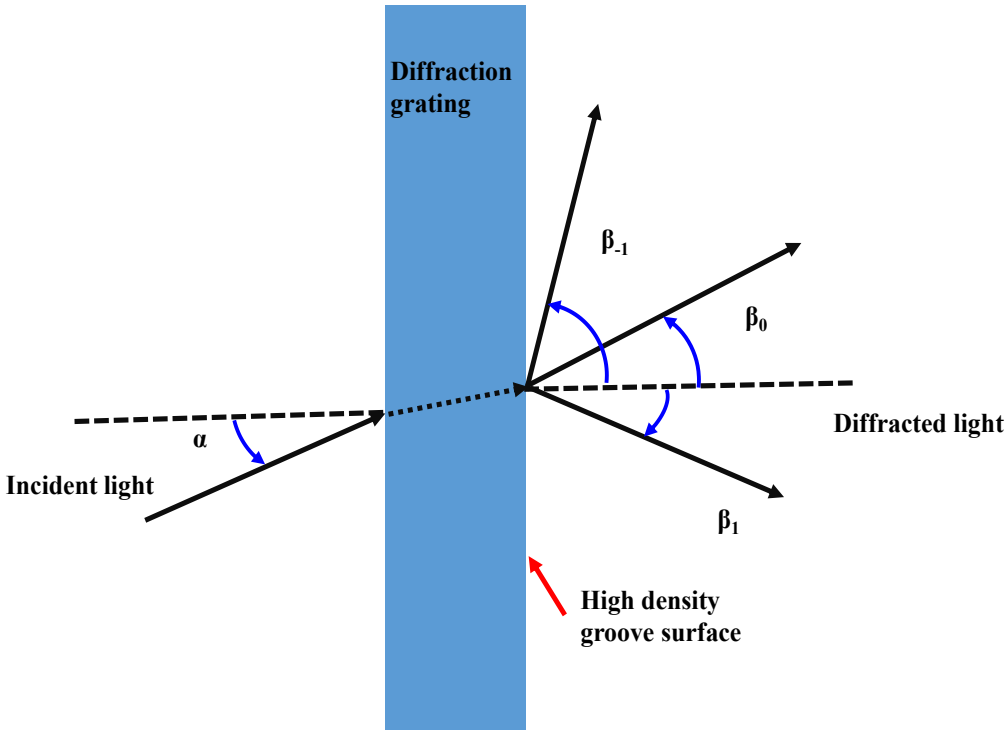

Figure 2.1 Light diffraction at a transmission plane diffraction grating with one side of high density groove surface.

Figure 2.1 shows the process when a beam of monochromatic light is incident at wavelength λ with an angle of α propagating through the transmission diffraction grating, which has a groove period d, also called the pitch or period, rays are diffracted with different discrete paths at the angles of β_m (m is the order of diffraction) emitted from the other side of the plane grating. The angles of β_m are measured by the grating normal, as in this case the plane grating is in transmission mode, the incident light and diffraction light could be regarded as mirror-rays. Therefore, the sign conversion for angles of β_m has to be opposite to their original sign. Here, $\alpha > 0$ is defined via measuring counter-clockwise from the grating normal, which is shown by arrows in Figure 2. 1, and diffracted rays of $\beta_1 > 0$, $\beta_{-1} < 0$, and $\beta_0 < 0$.

The relationships among grating period d, incident angle α, diffraction angles β_m, diffraction order m and wavelength λ are describe by [34]

$$m\lambda = d(\sin\alpha + \sin\beta) \tag{2.1}$$

$G=1/d$ is the groove density, also called groove frequency or grooves per mm. Thus, equation (2.1) can be rewritten as

$$Gm\lambda = \sin\alpha + \sin\beta \tag{2.2}$$

The angular dispersion (D) of a diffraction grating at a diffraction order m can be obtained from equation (2.1) via differentiating, the incident angle α is regarded as a constant, thus

$$D = \frac{\partial\beta}{\partial\lambda} = \frac{m \cdot \partial\beta}{d \cdot \partial(\sin\alpha + \sin\beta)} = \frac{m}{d\cos\beta} = \frac{m}{d}\sec\beta \tag{2.3}$$

For 2D imaging, 1D diffraction grating is usually combined with VIPA, whose schematic is shown in Figure 2.2. In this setup, the dispersion in x-axis and y-axis can be regarded as independent, the angular dispersion of diffraction grating is employed to perform y-axis spatial dispersion, and x-axis spatial dispersion is obtained by using a VIPA disperser. The theory of 2D spatial disperser investigation is in [19,31,32], based on the previous analysis, the spatial dispersion of VIPA in x-axis is given by

$$\lambda_p - \lambda_0 = -\lambda_0\left[\frac{\tan\theta_{in}\cos\theta_i}{n_r\cos\theta_i}\cdot\frac{x}{f} + \frac{x^2}{2n_r^2 f^2}\right] \tag{2.4}$$

where $\lambda_p(x)$ is a wavelength whose intensity peak at the position of x, n_r is the refractive index of VIPA, θ_{in} is the incident light angle goes to VIPA and θ_i is the incident beam angle inside of VIPA, which follows $n_r\sin\theta_i = \sin\theta_{in}$, f is the focal length of the lens after VIPA.

The spatial dispersion of diffraction grating in y-axis in the 2D spatial disperser is given by

$$\lambda_p - \lambda_0 = -d\cos\alpha\cdot\frac{y - y_0}{f} \tag{2.5}$$

where $d(\sin\alpha + \sin\beta) = \lambda_0$ when m=1, and wavelength λ_0 has intensity peak at position y_0.

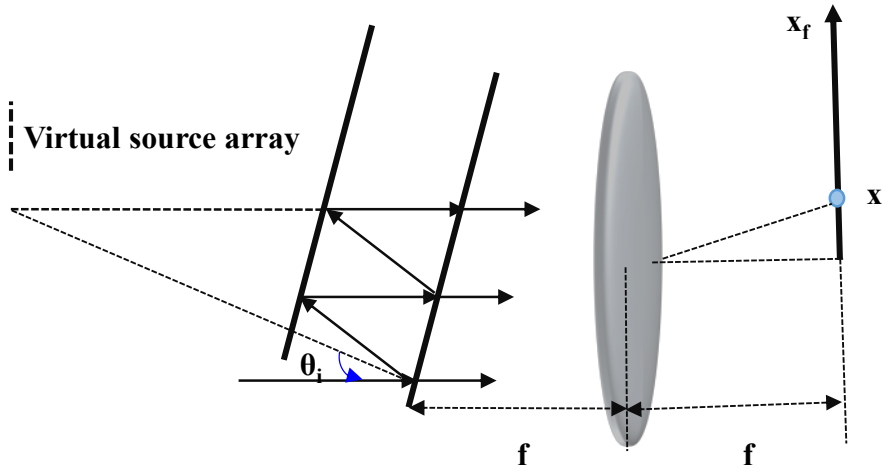

Figure 2.2 Schematic of VIPA spectral disperser geometry.

By exploiting the spatial dispersion devices of diffraction gratings for 1D mapping or diffraction gratings combined with VIPAs for 2D mapping, the unique uniform one-to-one mapping between spatial position and spectrum of incident broadband light can be obtained.

2.2.2. Spectrum to time conversion

To achieve ultrafast optical imaging, the space to spectrum conversion is not adequate because of no such equipment could detect spectrum of incident broadband light at ultrafast speed. Therefore, spectrum to time conversion technique, also known as wavelength to time mapping, photonic time-stretch (PTS), dispersive Fourier transform (DFT), real-time Fourier transform [12,13,16] is introduced.

The theory behind spectrum to time conversion is based on temporal dispersion. When a beam of broadband short-pulsed light propagating through a dispersive nonlinear medium, which indicates the refractive index varies for different

wavelengths, light of different wavelengths will travel at different speeds in that medium, as a result, different wavelengths can be separated after a certain distance.

Assuming an input short-pulsed light $e_{in}(t)$ with its spectrum $E_{in}(\omega)$, ω is the angular frequency. The spectral phase information $\psi(\omega)$ is added after propagating through a dispersive medium, the output of the pulse is expressed as [35]

$$e_{out}(t) = \frac{1}{2\pi}\int d\omega E_{in}(\omega)\exp(j\omega t)exp(j\psi(\omega)) \tag{2.6}$$

The phase information will change due to propagating through a dispersive medium at a distance of L, the relation can be given by

$$\psi(\omega) = -\beta(\omega)\cdot L \tag{2.7}$$

where $\beta(\omega)$ is called propagation constant in the medium. The Taylor series expansions of $\psi(\omega)$ and $\beta(\omega)$ are expressed as

$$\psi(\omega) = \psi_0 + \psi_1(\omega-\omega_0) + \frac{\psi_2}{2}(\omega-\omega_0)^2 + \frac{\psi_3}{6}(\omega-\omega_0)^3 + \cdots \tag{2.8}$$

$$\beta(\omega) = \beta_0 + \beta_1(\omega-\omega_0) + \frac{\beta_2}{2}(\omega-\omega_0)^2 + \frac{\beta_3}{6}(\omega-\omega_0)^3 + \cdots \tag{2.9}$$

where $\psi_n = \frac{\partial^n \psi}{\partial \omega^n}$, $\beta_n = \frac{\partial^n \beta}{\partial \omega^n}$, when $\omega = \omega_0$. Also from equation (2.7), we can obtain $\psi_n = \beta_n \cdot L$.

If $\beta(\omega)$ is a linear function of ω, then

$$\beta(\omega) = \beta_0 + \beta_1(\omega-\omega_0) = \beta_0 + \beta_1\varpi \tag{2.10}$$

where $\varpi=\omega-\omega_0$, and if $E_{in}(\omega)$ is replaced by $A(\varpi)$, the equation (2.6) can be expressed as

$$e_{out}(t) = \mathrm{Re}\{\exp(j(\omega_0 t - \beta_0 t)) \cdot a_{out}(t)\} \tag{2.11}$$

where

$$a_{out}(t) = \frac{1}{2\pi}\int d\varpi \cdot A(\varpi) \cdot \exp\{j[\varpi t - (\beta_1 \varpi + \frac{\beta_2}{2}\varpi^2 + \frac{\beta_3}{6}\varpi^3 \cdots)L]\} \tag{2.12}$$

When $\beta(\omega)$ is a linear function of ω as in the equation (2.10), the result of $a_{out}(t)$ can be expressed as

$$a_{out}(t) = a_{in}(t - \beta_1 L) \tag{2.13}$$

The equation (2.13) shown the output of the pulse travels at the velocity of $1/\beta_1$, is the intact replica of the input pulse. This velocity is called group velocity v_g, also known as modulation or envelope of the pulse, which defines the overall shape of the pulses' amplitudes when propagating through the medium. Considering a pulse has a time delay τ in the scheme of $\beta(\omega) = \beta_0 + \beta_1(\omega - \omega_0)$, from equation (2.7) and equation (2.10), the result of τ can be described as

$$\tau = -\frac{\partial \psi(\omega)}{\partial \omega} = \beta_1 L = \frac{L}{v_g} \tag{2.13}$$

When light propagating through a medium whose propagating constant $\beta(\omega)$ has a linear function of ω, the output of the pulse can be regarded as a replica of the input pulse.

If $\beta(\omega)$ is not a linear function of ω, $a_{out}(t)$ varies to $a_{in}(t)$. The part of $\beta(\omega)$ apart from β_0 and β_1 is called dispersion. If $\beta(\omega) \approx \beta_0 + \beta_1(\omega - \omega_0) + \frac{\beta_2}{2}(\omega - \omega_0)^2$, $\beta_2 = \frac{\partial^2 \beta}{\partial \omega^2}$, named second order of propagation constant or group velocity delay (GVD), is the term leading to a linear variation in delay with frequency resulting from a quadratic spectral phase variation. This could be regarded as a linear chirp to the output pulse. If $\beta(\omega) \approx \beta_0 + \beta_1(\omega - \omega_0) + \frac{\beta_2}{2}(\omega - \omega_0)^2 + \frac{\beta_3}{6}(\omega - \omega_0)^3$, $\beta_3 = \frac{\partial^3 \beta}{\partial \omega^3}$, named third order of propagation constant, is the term leading to quadratic variation in delay with

frequency resulting from a cubic spectral phase variation, which produces an asymmetrically oscillatory distortion within the pulse.

Here, considering the nonlinear group delay response effect of propagation constant, $\beta(\omega)$ is redefined as

$$\beta(\omega) = \frac{\omega n(\omega)}{c} \tag{2.14}$$

And the group velocity v_g can be rewritten as

$$v_g = \frac{c}{n + \omega(\partial n / \partial \omega)} = \frac{c}{n - \lambda(\partial n / \partial \lambda)} \tag{2.15}$$

For a frequency component of ω in a short pulse, the propagating time of through a dispersive medium with a length of L is $L / v_g(\omega)$, the difference of propagation time between ω *and* ω_0, is expressed as

$$\Delta\tau(\omega) = \tau(\omega) - \tau(\omega_0) = \beta_2(\omega - \omega_0)L = \left(2\frac{\partial n}{\partial \omega} + \omega\frac{\partial^2 n}{\partial \omega^2}\right)\frac{(\omega - \omega_0)L}{c} \tag{2.16}$$

By substituting equation (2.15) to equation (2.16), the difference of propagation time between ω *and* ω_0, is rewritten as

$$\Delta\tau(\omega) = \frac{\lambda^3 L(\omega - \omega_0)}{2\pi c^2}\frac{\partial^2 n}{\partial \lambda^2} \tag{2.17}$$

In fibre optics, the frequency is usually substituted by wavelength, the wavelength offset $\Delta\lambda = \lambda - \lambda_0$, the time varies is expressed as

$$\Delta\tau(\lambda) = \frac{-2\pi c\beta_2 \Delta\lambda L}{\lambda^2} = D\Delta\lambda L \tag{2.18}$$

where D is the dispersion parameter with units of *ps/(nm*km)*, which is defined as

$$D = \frac{-2\pi c\beta_2}{\lambda^2} = \frac{-\lambda}{c}\frac{\partial^2 n}{\partial \lambda^2} \tag{2.19}$$

Thus, the second-order spectral phase can be given as

$$\psi_2 = -\beta_2 L = \frac{-\partial\tau(\omega)}{\partial\omega} = \frac{-\lambda^3 L}{2\pi c^2}\frac{\partial^2 n}{\partial \lambda^2} \tag{2.20}$$

And third-order spectral phase can be given as

$$\psi_3 = -\beta_3 L = \frac{-\partial^2\tau(\omega)}{\partial\omega^2} = \frac{\lambda^4 L}{4\pi^2 c^3}\left(2\frac{\partial^2 n}{\partial \lambda^2} + \lambda\frac{\partial^3 n}{\partial \lambda^3}\right) \tag{2.21}$$

GVD is the term used to describe how the dispersive medium would affect the short pulse when propagating through it. The GVD can be defined as

$$GVD = \frac{\partial}{\partial\omega}\left(\frac{1}{v_g(\omega)}\right) = \frac{\partial\beta_1}{\partial\omega} = \beta_2 = \frac{2}{c}\frac{\partial n}{\partial\omega} + \frac{\omega}{c}\frac{\partial^2 n}{\partial\omega^2} \quad when \quad \omega = \omega_0 \tag{2.22}$$

The GVD can be expressed in three domains: wavelength λ, angular frequency ω, and frequency v,

$\beta_2(\lambda)$ in *ps/(nm*km)* is given by

$$\beta_2(\lambda) = \frac{\partial\tau}{\partial\lambda} = \frac{2\tau}{\lambda} - \frac{\lambda^2}{2\pi c}\frac{\partial^2\beta}{\partial\lambda^2} \tag{2.23}$$

$\beta_2(\omega)$ in $ps^2/(rad*km)$ is given by

$$\beta_2(\omega) = \frac{\partial\tau}{\partial\omega} = \frac{\partial^2\beta}{\partial\omega^2} \tag{2.24}$$

$\beta_2(v)$ in ps^2/km is given by

$$\beta_2(v) = \frac{\partial\tau}{\partial v} = 2\pi\frac{\partial\tau}{\partial\omega} = 2\pi\beta_2(\omega) \tag{2.25}$$

The relationship among these three coefficient are given by

$$\beta_2(\lambda) = -\frac{2\pi c}{\lambda^2}\beta_2(\omega) = -\frac{c}{\lambda^2}\beta_2(v) \tag{2.26}$$

So the linear frequency to time mapping relationship can be expressed as

$$\Delta t = \beta_2(v)\Delta v = 2\pi\beta_2(\omega)\Delta v = \beta_2(\omega)\Delta\omega = \beta_2(\lambda)\Delta\lambda \tag{2.27}$$

When a short pulse travelling through the medium with linear group delay response, linear variation in delay with frequency will be obtained, thus one-to-one mapping between the wavelength and time can be achieved. The process of short pulse propagating through the dispersive medium is shown in Figure 2. 3.

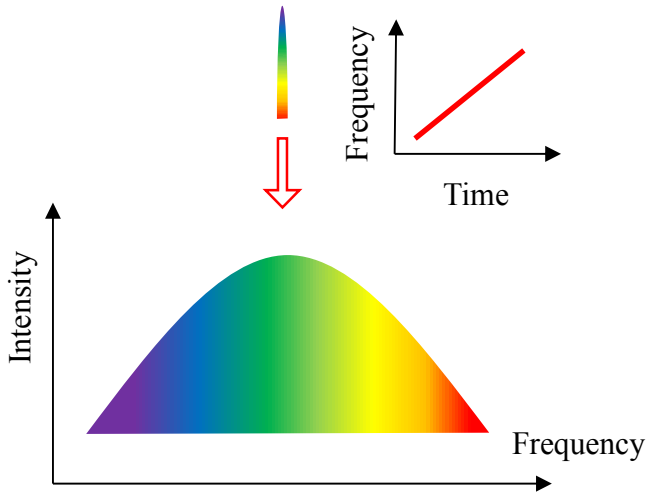

$$\beta(\omega) \approx \beta_0 + \beta_1(\omega - \omega_0) + \frac{\beta_2}{2}(\omega - \omega_0)^2$$

Figure 2.3 Diagram of linear group delay responsive medium lead to linear variation in delay with frequency when a short pulse propagating through it.

There are different type of medium are employed to perform linear mapping between wavelength and time.

For example, Figure 2.4 (a) shows the mostly common used dispersive compensating fibre (DCF) as the medium with nonlinear effect, also normal single

mode fibre can be presented as a substitute depending on the needs of dispersion amount, bandwidth of spectrum and optical loss. The DCF has a GVD of ~-120ps/nm/km, which is much larger than normal SMF-28 fibre (a GVD of ~17.4ps/nm/km). The dispersion slope of DCF is negative while that of SMF-28 fibre is positive. The DCF has the excellent performance of dispersion-to-loss ratio and bandwidth compared to SMF-28 fibre. However, DCF is only available in the fibre-optic communication band around 1550nm while SMF-28 fibre can work in the wide spectral band of 1200-1600nm.

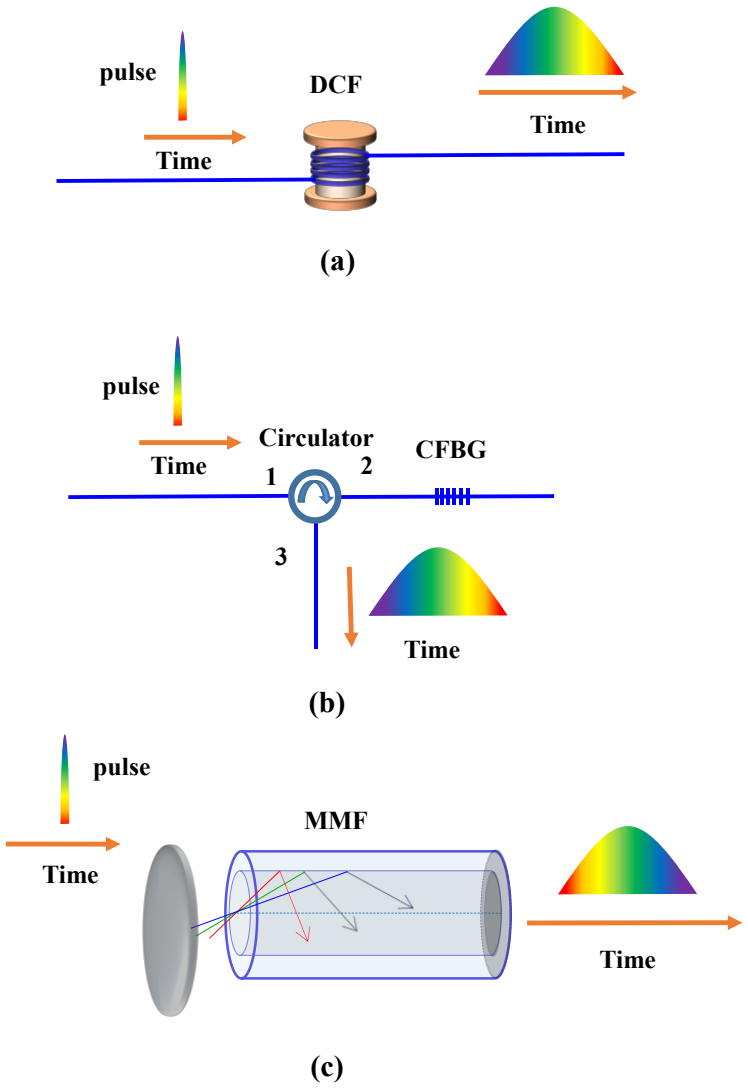

Figure 2.4 Different types of methods to obtain linear mapping between wavelength and time, i.e. PTS, using (a) DCF: dispersive compensating fibre; (b) CFBG: chirped fibre Bragg grating; (c) MMF: multimode fibre.

Figure 2.4 (b) shows the chirped fibre Bragg grating (CFBG) is utilized to perform this process based on the structure of CFBG and chirped fibre Bragg reflection. The periodic variation in the refractive index of fibre core leading to dielectric mirror. The refractive index of CFBG is chirped so different wavelengths are reflected at different time delays. Thus the linear mapping between time and wavelength is obtained via reflecting different wavelengths at different time. The benefit of CFBG for dispersion is its short length and easily customized GVD amount for the specified requirement. The drawback of CFBG for dispersion is it has group-velocity ripples that can converted to unwanted fast temporal modulation, also it cannot provide internal optical amplification.

Figure 2.4 (c) shows MMF is exploited to perform the linear mapping process via modal dispersion when the rainbow optical light emitted into MMF, different wavelengths of light will travel as different modal profiles in the MMF. In this setup, the input facet of MMF is placed at the lens focus so varied wavelength of light are coupled into varied fibre mode with different optical path difference and different travel time. The advantages of this method are its ability of providing large GVD in any spectral band and tuning the amount of GVD. While the disadvantages are its nonlinear dispersion slope and its challenge of optical amplification and implementability in MMF.

Considering the third order differential of $\beta(\omega)$,

$$\beta_3(\lambda) = \frac{\partial \beta_2(\lambda)}{\partial \lambda} \quad \beta_3(\omega) = \frac{\partial \beta_2(\omega)}{\partial \omega} \quad \beta_3(\mathrm{v}) = \frac{\partial \beta_2(\mathrm{v})}{\partial \mathrm{v}} \tag{2.28}$$

The relationship among these three high-order coefficient are given by

$$\beta_3(\lambda) = \frac{4\pi^2 \mathrm{c}^2}{\lambda^4} \beta_3(\omega) = \frac{\mathrm{c}^2}{\lambda^4} \beta_3(\mathrm{v}) \tag{2.29}$$

The third order of propagation constant will lead to quadratic variation of spectral phase in delay with frequency, thus asymmetrically oscillatory distortion within the envelope of the time-stretched pulse is obtained. The chirped effect of the nonlinear

group delay responsive medium is shown in Figure 2. 5 when a short pulse propagating through it.

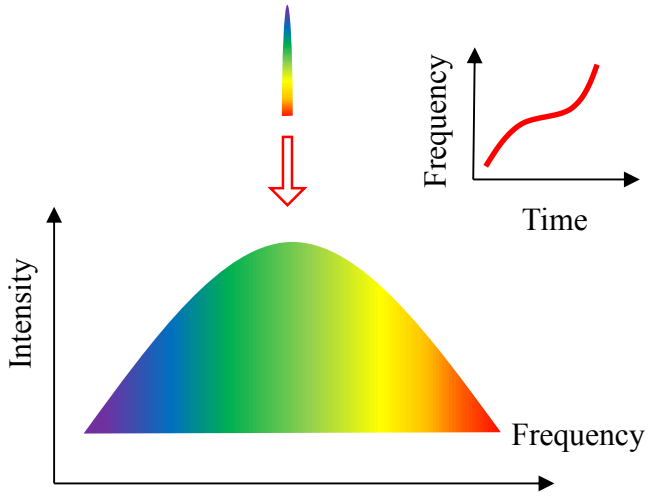

$$\beta(\omega) \approx \beta_0 + \beta_1(\omega - \omega_0) + \frac{\beta_2}{2}(\omega - \omega_0)^2 + \frac{\beta_3}{6}(\omega - \omega_0)^3$$

Figure 2.5 Diagram of effect of third order propagation constant in nonlinear group delay responsive medium when a short pulse propagating through it.

In this thesis, only linear mapping between wavelength and time is experimentally demonstrated. The nonlinear mapping between wavelength and time can be used for anamorphic time stretch transformation [36], which is another solution for big data issue.

2.2.3. STEAM based systems

There are two configurations of STEAM based systems that widely used.

First one is laser scanner [6], which puts PTS before wavelength to space conversion. The diagram of the system is shown in Figure 2. 6. The short femto-second pulse from Mode-locked-laser (MLL) propagated through the dispersive medium, such as dispersive compensating fibre (DCF), to perform one-to-one mapping between wavelength and time. After passed the diffractive devices, such as diffractive grating, where one-to-one mapping between time and space is

obtained, the time-encoded spectral information reached the imaging target. The transmitted or reflected information can be detected by a single-pixel photodetector in time serial. In such a system, the waveform of varied wavelength reached the varied spatial points of target at varied time. And in this setup it can be regarded as an ultrafast laser scanning system with low light intensity, which has the potential of protecting light-sensitive samples. The drawback of this configuration is when the sample is flowing at a certain speed in another dimension, a chirped effect is induced due to the different wavelength of light reached the sample at different time.

The second one is traditional imaging system, which put PTS after the wavelength to space conversion, the spectrum of the time waveform reached the spatial imaging target at the same time. The schematic of this system is shown in Figure 2. 7. The advantage of this configuration is different wavelength of light reached the sample at same time so when the sample is moving in another dimension no distortion is induced.

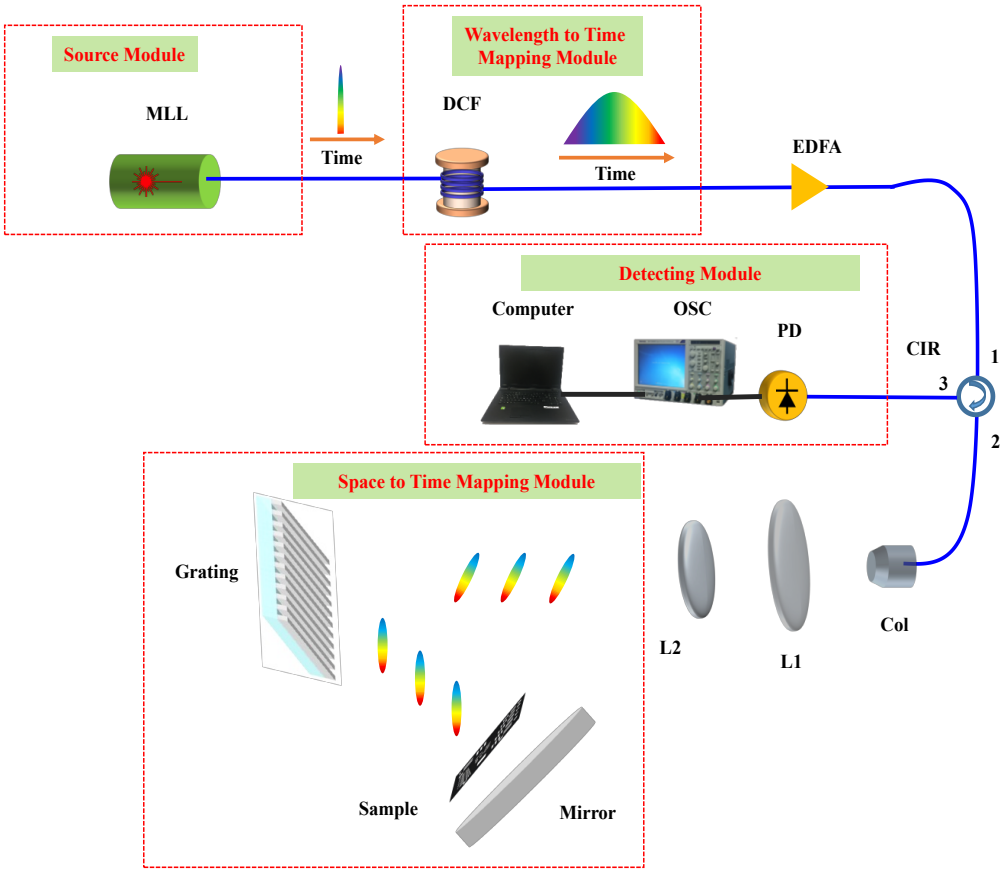

Figure 2.6 Diagram of laser scanner based on STEAM.

Recently there are several of transformed STEAM systems, for example, reducing the cost via replacing the expensive devices, such as replacing MLL [24,25], using better optical source in PTS based ultrafast SPI system to achieve faster imaging speed [37], more dimensional detection or observation with multiplexing methods, detecting transparent object via adding interferometric structure [26,27], performing STEAM system in another wavelength band, such as 1 micro-meter [38], dealing with big data issue using CS method [39].

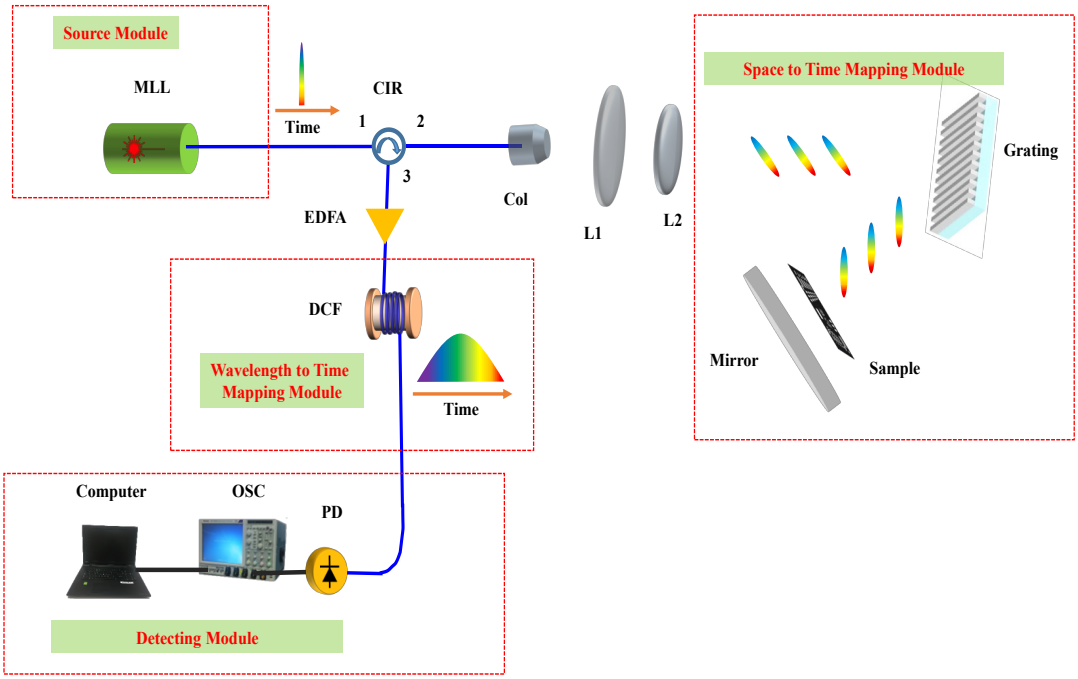

Figure 2.7 Schematic of traditional STEAM imaging system.

In [24], an amplified spontaneous emission (ASE) source approach for substituting the expensive MLL source in the STEAM system is presented. This approach consists of an ASE source, Fabry-Perot (F-P) filter, MZM, and arbitrary waveform generator (AWG), the continuous light from ASE was spectrally shaped in the F-P filter and the spectrally shaped broadband wavelength was temporally shaped into short pulses after MZM, which was modulated by an AWG. Its diagram of ASE source approach for substituting MLL is illustrated in Figure 2. 8.

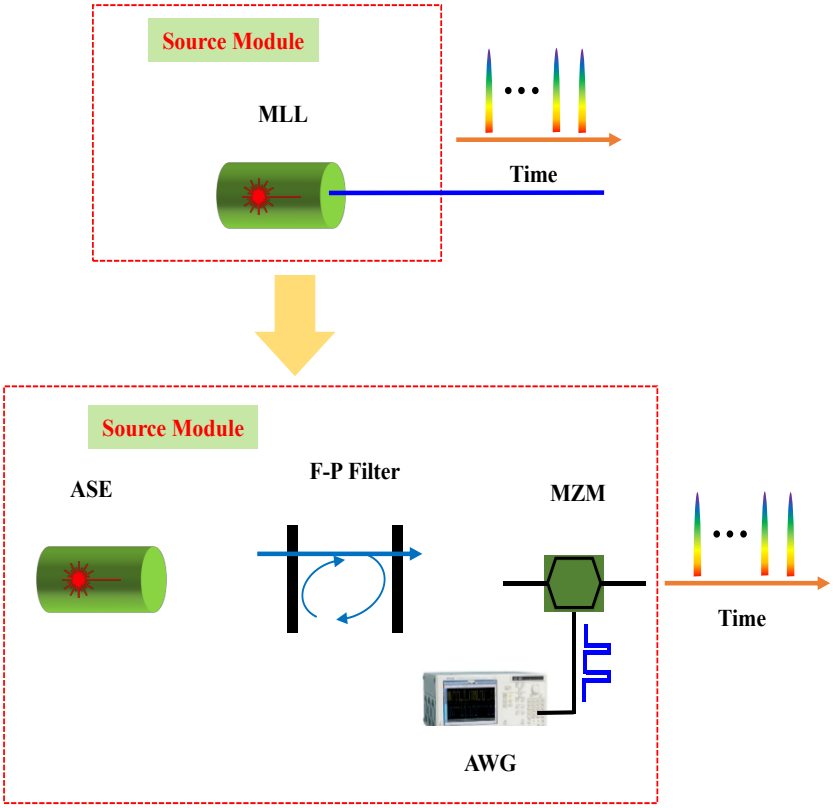

Figure 2.8 An ASE source approach, which consisting of an ASE source, F-P filter, MZM and AWG, for substituting the expensive MLL source in the STEAM system.

Another approach that substituting MLL source is presented in [25], which was achieved via using distributed feedback (DFB) laser array, arrayed waveguide grating (AWG), MZM and pulse pattern generator (PPG). Single wavelength DFB lasers are combined after the AWG, thus continuous multi-wavelength broadband laser is formed. After propagating through the MZM, which is modulated by a PPG, the temporally shaped multi-wavelength broadband pulses that could be used for imaging application in STEAM system are obtained. The schematic of DFB laser array approach for substituting MLL is illustrated in Figure 2. 9.

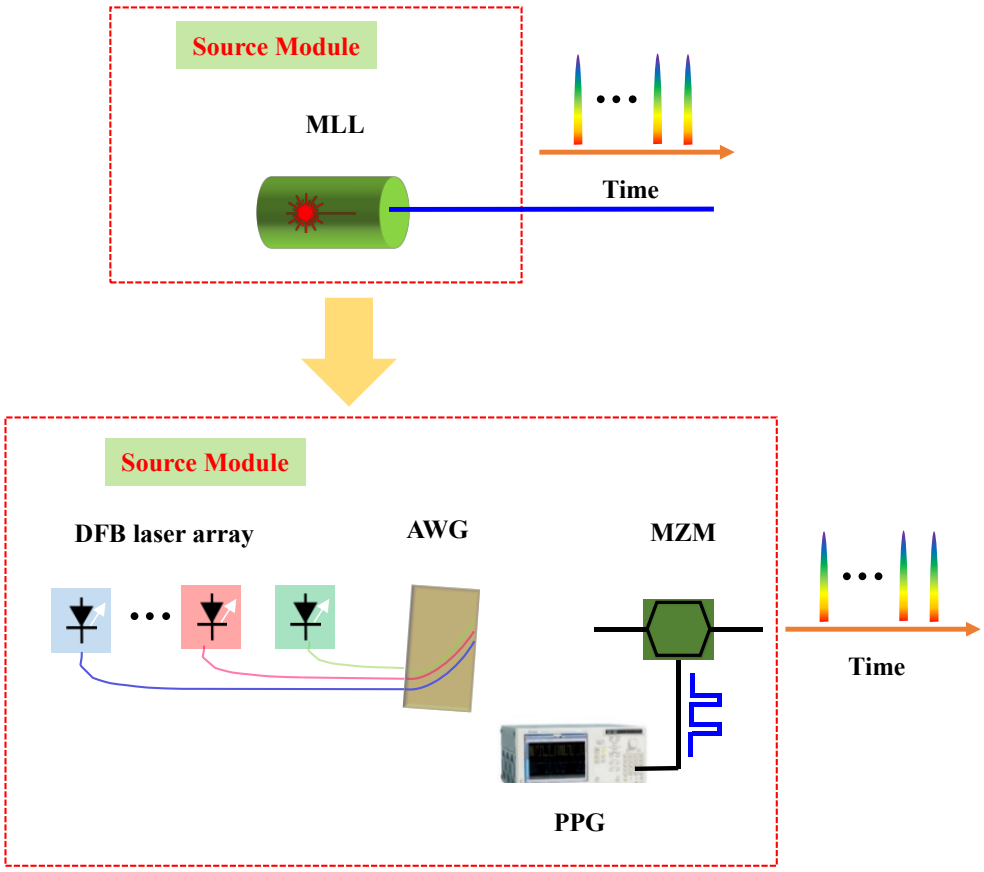

Figure 2.9 The schematic of DFB laser array approach, which consisting of a DFB laser array, AWG, MZM and PPG, for substituting the expensive MLL source in the STEAM system.

The transparent object detection based on phase-contrast STEAM system is investigated. Traditional intensity-contrast STEAM system cannot observe transparent object easily due to lack of phase information, however, if added interferometric structure in intensity-contrast STEAM system then phase information and transparent object detection is obtained [26]. The schematic of interferometric structure of STEAM system is shown in Figure 2. 10. A beam splitter is inserted before the diffraction grating, where wavelength to space linear mapping is obtained, and mirrors are used to reflect the pulses, thus a reference arm consisting of a beam splitter and two mirrors is performed. And the differential phase information is converted into intensity modulation when the pulses are recombined after beam splitter.

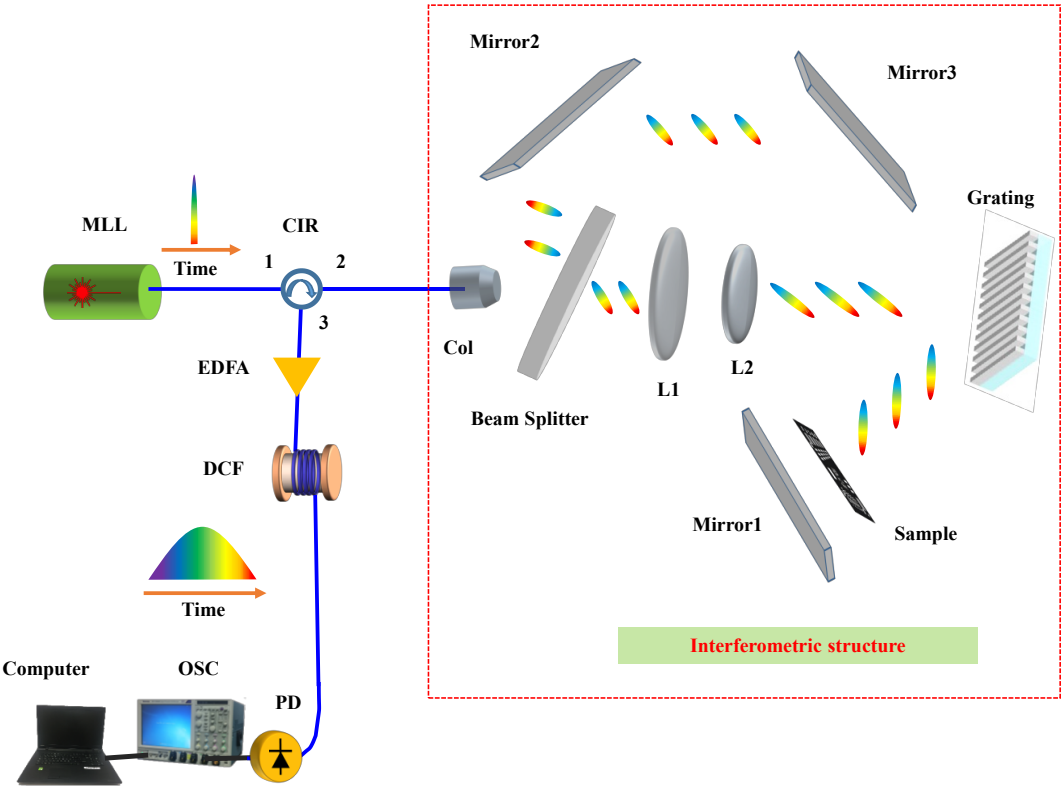

Figure 2.10 Diagram of interferometric structure to detect transparent objects based on phase-contrast STEAM systems.

Another approach that using a Nomarski prism to perform polarization multiplexing, which has the benefit of increasing the contrast of imaging and detecting transparent objects, is presented in [27] and its schematic is shown in Figure 2.11. In this approaching method, two adjacent points of the transparent objects are illuminated with two orthogonally-polarized pulses of same wavelength via using a Nomarski prism. The pulses of same wavelength experienced with different phase shifts, which are induced by optical path difference (OPD), on the transparent object of two adjacent points. After reflected by the mirror and recombined by the same Nomarski prism, the phase information of the transparent object is converted into intensity information.

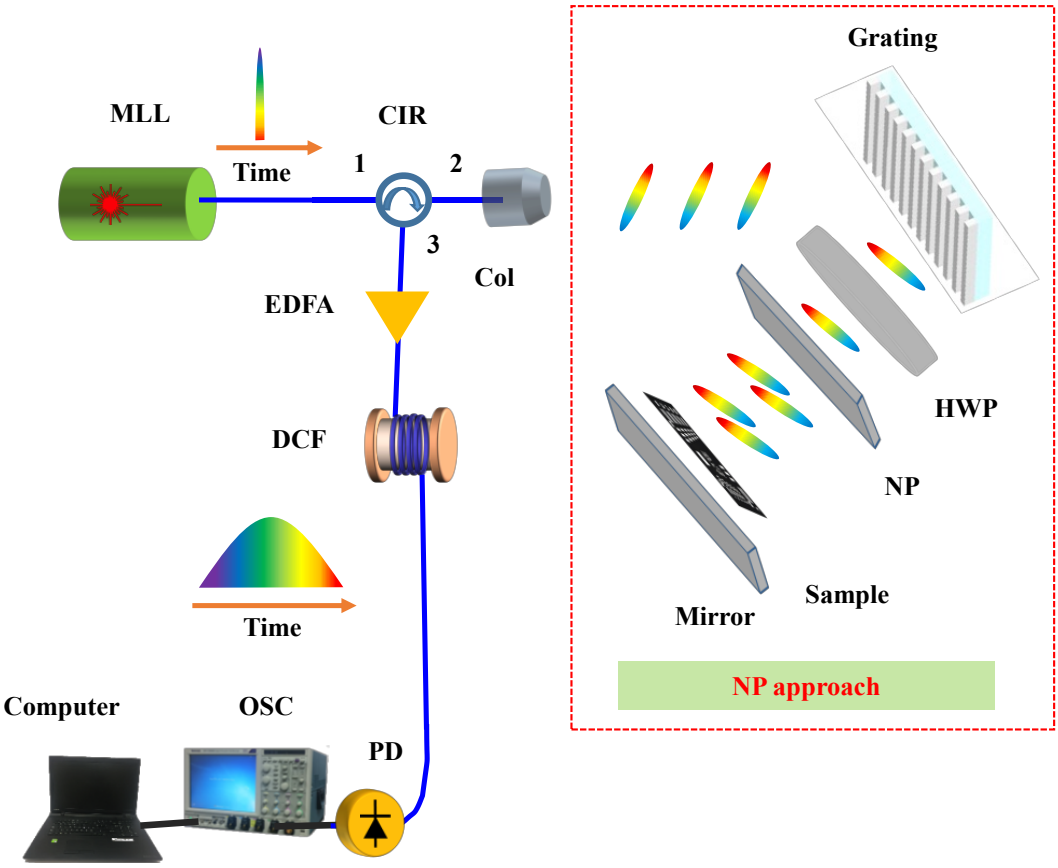

Figure 2.11 Diagram of Nomarski prism approaching to detect transparent objects based on STEAM systems.

In order to deal with the big data issue in the high-throughput STEAM system, CS method is applied to compress the data and reduce the cost via using a low-cost low-speed PD [39]. This is made possible by the principle of CS method, which could reduce the acquisition speed from originally tens of GHz to tens of MHz (one data per frame). Therefore, a large amount of data volume is saved and the cost of system is reduced. The schematic of proposed system is shown in Figure 2. 12. The AWG and MZM is exploited to modulate the stretched optical pulses, sinusoidal signals from AWG is used to drive MZM and time-stretched optical pulses with sinusoidal envelope are obtained to perform CS imaging process.

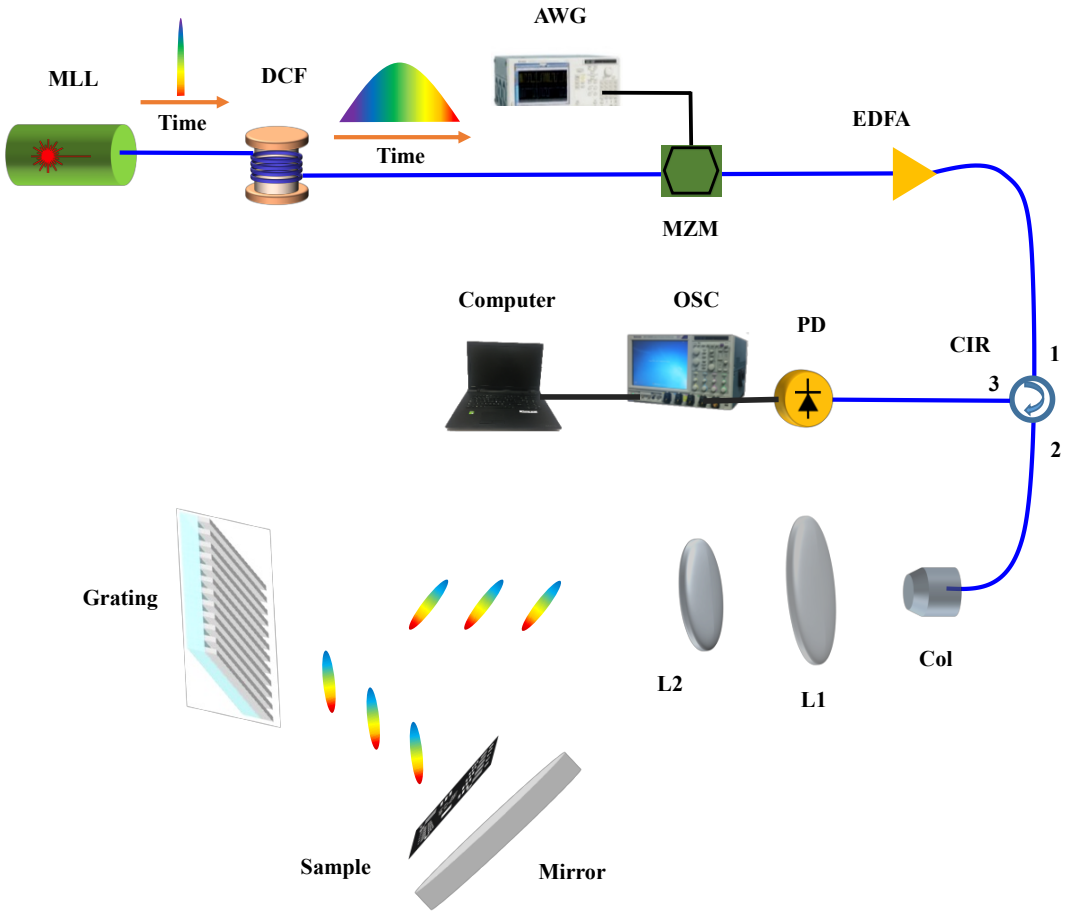

Figure 2.12 Diagram of CS method for data compression based on STEAM systems.

2.3. Titled fibre grating (TFG) and its applications

TFG is one type of fibre gratings with special features. The concept of TFG was first proposed by Meltz et al. in 1990 [40], and its mode matching mechanism was described by Erdogan and Sipe [41]. Like normal fibre Bragg gratings, TFGs have periodical refractive index variation in axial direction, but its boundary surface of the varied index is tilted with respect to the fibre axis instead of perpendicular to it, which endows it with unique optical properties compared to normal fibre Bragg gratings (FBGs) and long period fibre gratings (LPFGs).

2.3.1. Types and analysis of TFGs

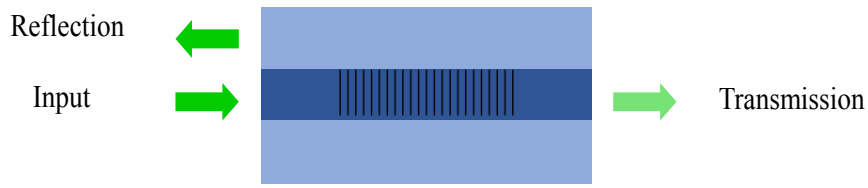

Figure 2.13 Structure of a typical uniform FBG.

The structure of uniform FBG is shown in Figure 2. 13, when optical broadband spectrum propagates it, only spectrum of certain particular wavelength is reflected back due to its inherent grating structure of periodical refractive fringes perpendicular to the fibre axis, while the majority of the spectrum transmits through it. Hence, it is widely used as an inline wavelength-specific reflector, optical filter to block certain wavelengths [42,43], distributed arrays of strain, acoustic, and temperature sensors and wavelength multiplexing device in communication system [44].

The fundamental theory of FBG is based on Fresnel reflection, which indicates that light of broadband spectrum propagates media with different refractive indices may have reflection and refraction at the interface. The reflected wavelength (λ_B) is given by [34]

$$\lambda_B = 2n_{e,core}\Lambda \tag{2.30}$$

where λ_B is also called Bragg wavelength, $n_{e,core}$ is the effective refractive index of the fibre core and Λ is the grating period. The bandwidth of reflected Bragg wavelength ($\Delta\lambda_B$) is defined by the relationship [34]

$$\Delta\lambda_B = \frac{2\delta n_0 \eta_{core}}{\pi} \cdot \lambda_B \tag{2.31}$$

where δn_0 is the difference of refractive index between the core and the grating, η_{core} is the fraction power in the core. In this thesis, only uniform structure of FBG and TFG is discussed.

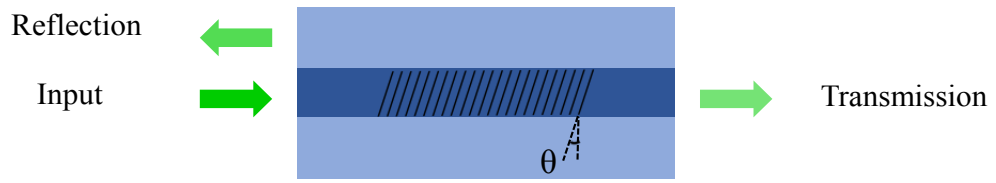

Figure 2.14 Structure of TFBG.

As promising passive components, the TFGs can be classified into three different type of categories, which are tilted fibre Bragg grating (TFBG), radially tilted fibre grating (RTFG) and excessively tilted fibre grating (Ex-TFG).

The first type is TFBG, whose structure is shown in Figure 2. 14. In TFBG, light of broadband spectrum from the forward propagating core mode is coupled into backward propagating core and cladding mode in specific wavelengths due to its tilted angle between grating fringes and fibre axis. TFBG also shows good surrounding refraction index (SRI) sensitivity due to light travelling in the cladding region. These features endow TFBGs with a wide range of practical applications.

The mode coupling mechanism in TFBG is analysed using phase matching condition, which is a parameter to illustrate the strongest wavelength mode coupling behaviour between the core and cladding modes. By the same way as FBG, the transmitted resonance wavelength that satisfying Bragg condition in the fibre core mode are determined by phase matching condition, which could be expressed as [45–48]

$$\lambda_B = 2n_{e,core}\Lambda_g \tag{2.32}$$

where Λ_g is the period of TFBG, in such case, Λ_g is defined by

$$\Lambda_g = \Lambda \cdot \cos\theta \tag{2.33}$$

where θ is the tilted angle of the TFBG.

As there is light reflection in cladding mode of TFBG, the cladding modes resonance wavelength ($\lambda_{clad,\ i}$), which also needs to meet the phase matching condition, can be expressed as

$$\lambda_{clad,i} = (n_{e,core} + n_{e,clad,i}) \cdot \Lambda_g \tag{2.34}$$

where $n_{e,clad,\,i}$ is the effective refractive index of the fibre cladding mode of TFBG, i indicates the order of cladding mode.

Similarly, the bandwidth of reflected Bragg wavelength ($\Delta\lambda_B$) in the core mode of TFBG is same as equation (2.31), while the bandwidth of cladding modes resonance wavelength ($\Delta\lambda_{clad,\,i}$) in TFBG is given by

$$\Delta\lambda_{clad,i} = \frac{(\delta n_0 \eta_{core} + \delta n_{e,clad,i} \eta_{clad})}{\pi} \cdot \lambda_{clad,i} \tag{2.35}$$

where η_{clad} is the fraction power in the cladding mode.

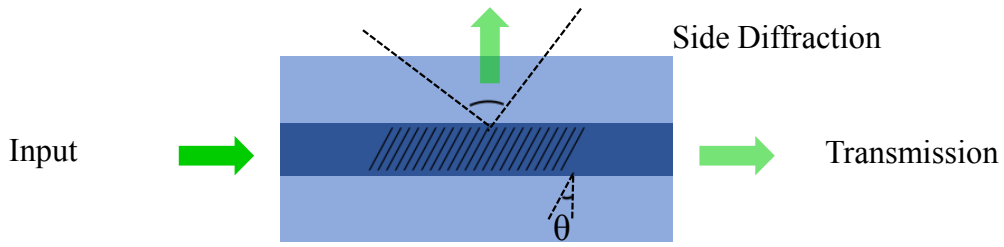

Figure 2.15 Structure of RFTG.

The second type of TFG is RTFG, whose structure is shown in Figure 2. 15. The light will be emitted into open space via fibre cladding when light transmitted through the fibre core in the RTFG, that is to say, forward transmission core mode is coupled into radiation mode when light of broadband spectrum propagating through it. The tilted angle of RTFG is between 23.1° and 66.9° [49].

In the past, the radiation in RTFG sometimes is regards as a nuisance. However, the radiation mode has found various applications. The theoretical analysis of RTFG was done in the last few years using phase matching condition. The scattering angle (β) of radiation mode in the fibre can be expressed as [50]

$$\cot\beta = \cot\theta - \frac{n\Lambda_g}{\lambda \sin\theta} \tag{2.36}$$

where n is the refractive index of the fibre core and λ is the wavelength of the light that scattered, Λ_g is the period of RTFG, θ is the tilted angle of the RTFG, β is the scattering angle of radiation mode that from core mode to cladding mode. When the light is scattered into open space, the refraction between fibre cladding and air at the interface should be taken into consideration. Hence, the scattering angle (α) of radiation mode outside of the fibre can be described as

$$\sin\alpha = \frac{n\cdot(\cot\theta - \frac{n\Lambda_g}{\lambda\sin\theta})}{\sqrt{1+\left(\cot\theta - \frac{n\Lambda_g}{\lambda\sin\theta}\right)^2}} \tag{2.37}$$

where α is the scattering angle of radiation mode that from fibre core to air. The angular dispersion of RTFG is investigated by [51]

$$\frac{\partial\beta}{\partial\lambda} = \frac{n\Lambda_g\sin\theta}{n^2\Lambda^2 - 2n\lambda\Lambda_g\cos\theta + \lambda^2} \tag{2.38}$$

In RTFG, the period Λ_g and the tilted angle θ of RTFG has the relationship of

$$\Lambda_g\cos\theta = \frac{\lambda}{2n} \tag{2.39}$$

Therefore, substitute equation (2.39) into equation (2.38), the angular dispersion of equation (2.38) can be rewritten as

$$\frac{\partial\beta}{\partial\lambda} = -\frac{\sin(2\theta)}{\lambda} \tag{2.40}$$

From the above equation, when the tilted angle θ is 45°, the angular dispersion of RTFG has the maximum value, which enables compact imaging application as an in-fibre diffractive device.

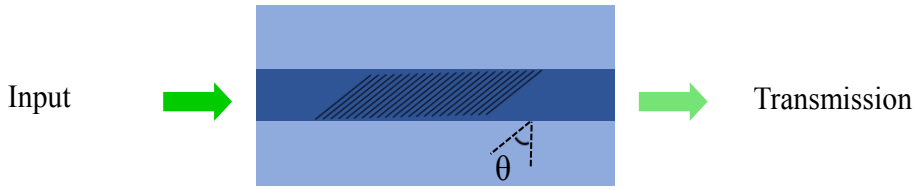

Figure 2.16 Structure of Ex-TFG.

The third type of TFG is Ex-TFG, whose structure is shown in Figure 2. 16. In Ex-TFG, light of broadband spectrum from forward propagating core mode will be coupled into forward propagating core and cladding modes. This characteristic of Ex-TFG endows it with lots of sensing applications.

In order to meet the phase matching condition, Ex-TFGs not only have core and cladding mode information, but also have the polarization states information. Thus, the phase matching condition of an Ex-TFG could be expressed as [52,53]

$$\lambda = (n_{e,core} - n_{e,clad}^{m,i}) \cdot \frac{\Lambda_g}{\cos\theta} \qquad i = TE \quad or \quad TM \tag{2.41}$$

where λ is the resonance wavelength, and Λ_g, θ is the period, tilted angle of the Ex-TFG, respectively, m is the m^{th} TE/TM cladding mode.

2.3.2. Applications of TFGs

The TFGs have a wide range of applications due to their special features. TFBGs, as the first type of TFGs, are found to have extensive sensing and measurement applications as inline compact sensors in review papers [46,54] thanks to their core and cladding backward propagating modes. TFBGs are used as refractive index sensors [55,56], temperature-independent strain sensors [57], temperature-self-calibrated biological sensing probes [47], directional bending sensors [58], simultaneous temperature and strain sensors [59], and humidity sensors [60] due to the cladding modes are sensitive to the surroundings. Also, they are utilized as temperature-calibrated high-precision inline refractometers [48,61] based on

cladding to core recoupling, wideband-adjustable reflection-suppressed rejection filters [62] based on core mode backward propagating, add-drop wavelength-division multiplexers [63] based on their mode coupling.

RTFGs can be exploited to use in different applications thanks to their special features. For example, RTFGs can be performed as in fibre linear polarizers in polarization sensitive optical system [64], also they are employed in optical spectrum analysers [51] as indispensable devices. As polarization sensitive compact inline devices, they are widely used in recently all-optical fibre ultrafast laser systems [65–67]. Besides, the angular dispersion feature of RTFGs can be utilized to perform imaging applications, such as in [68], an inline compact fibre spectrometer is designed and experimentally demonstrated using a RTFG as the inline compact diffraction device based on the optical coherence tomography (OCT) structure. In [11,69], two high-efficient, low-cost, compact diffraction limited imaging systems with the purpose of 1D and 2D imaging is designed and experimentally performed using a 45° TFG, which is regarded as a high-efficient inline compact diffraction device, and in [12], a resolution improved ultrafast optical imaging system based on 45° TFG is presented for the first time with unpreceded imaging speed of 46 m/s.

Ex-TFGs demonstrate forward propagation, thus this characteristic entrusts them with a series of applications. An in-fibre twist sensor [70] is performed using an Ex-TFG due to the polarization dependent coupling behaviour of polarization states changes together with fibre twist. An in-fibre directional transverse loading sensor [71] is experimentally demonstrated using an Ex-TFG because of polarized modes change when transverse load is applied to it. Highly sensitive refractive index sensors [72] based on Ex-TFGs is experimentally analysed and demonstrated and based on the surrounding-sensitive feature of Ex-TFGs, biosensors in the detection of glucose [73] and water level sensors based refractive index [74] are presented, respectively.

2.4. Multimode fibre (MMF) for imaging applications

With the development of technology single-mode fibre reaching its bottleneck, MMF experienced resurging attraction due to its feature of higher capacity and larger numerical aperture. Light experienced randomization of phase, polarization and optical speckle pattern intensity distribution when travelling in MMF, which has extensive applications in imaging [75–81] and communications [82,83].

2.4.1 Types of MMF

There are mainly two types of MMFs and both of them has varied characteristics. The first type is step-index MMF, which has uniform core refractive index and uniform cladding index and an index-step between the core and cladding. The second one is graded-index MMF, which has graded-reduced refractive index from the centre of core to its larger radius of core. The mode dispersion in graded-index MMF is smaller than in step-index MMF.

The mode of the fibre is defined as its potential path that propagating through the MMF. MMF can support from few modes to tens of thousands of modes depending on the core/cladding regions, refractive index, numerical aperture (NA), and wavelengths. The lower-order modes confines light spatially transmitting in the core of the fibre, while the higher-order modes confines light spatially transmitting near the interface between core and cladding of the fibre. The number of mode (M) can be estimated using normalized optical frequency, also called V-number, which is expressed as

$$V = \frac{2\pi a}{\lambda} NA \tag{2.42}$$

where a is the radius of the fibre core, λ is the wavelength of the light, NA is numerical aperture. The number of modes in MMF can be expressed as

$$M \approx \frac{V^2}{2} \tag{2.43}$$

2.4.2. MMF for imaging applications

When light travelling in MMF, randomization of phase, polarization and optical speckle pattern intensity distribution is obtained. Hence, MMF has attracted extensive attention in the applications of imaging.

Wavefront shaping, which is of great importance for imaging applications, is a useful technique that can be used to manipulate light. In [84], wavefront shaping with adaptive optimization is achieved and light is controlled and focused when propagating through a nonlinear scattering medium, such as MMF. In [85], not only wavefront shaping with iterative optimization, but also additional amplification, which improved the signal-to-noise ratio (SNR), is obtained using a rare-earth-doped MMF.

The spatio-temporal phenomenon in MMF is studied in various groups. In [86], strong nonlinear coupling and low modal dispersion is obtained when nonlinear ultrashort pulse propagating in a graded-index MMF. It also attest that spatiotemporal effects of MMF has several interest applications, and spatiotemporal dynamics and phenomena can be observed using a MMF. The spatiotemporal effect, intermodal interactions, and disorder of MMF, which is integrated as a whole unity, is studied in [83], and it indicates MMF is a useful device in complex science.

Light transmitting in MMF is very sensitive to the variation of geometry and the randomization of phase, polarization and intensity distribution, which normally make imaging unstable, and to some extent, impossible. However, in [80], a S-shaped MMF with a bending length of 25 mm is simulated to be limited effect on the imaging performance, which illustrates MMF can be an potential imaging device. Also, in [79], in contrary to conventional view of MMF as a unstable device, with a complex accurate theoretical model, light propagation can be predicted over 300 mm in a largely distorted parts of MMF, which opens the away for high-depth-imaging inside of human tissue.

Several of other imaging methods are based on MMFs. For example, in [87], wavelength to time mapping is achieved using a tapered single-mode multicore

fibre, which paves the way for future imaging applications. In [76], a high-resolution 3D two-photon fluorescence imaging through a MMF is demonstrated. In [78], light propagating through the MMF is investigated via an experimental geometry, which is utilized in biophotonical imaging. In [77], the resolution of MMF based imaging system is investigated and the result is indicated that the number of resolvable pixels in the image equals four times of that of spatial modes in each polarization state.

2.5. Optical data compression

The utilization of PTS enables millions of frames per second imaging and offers cancer cell detection with unprecedented high-throughput and speed. However, one of its nettlesome consequence in high-throughput imaging data acquisition is the great volume of data (hundreds of gigabits even terabits of data per second) that generated by the imaging system needs to be processed. Thus, to solve this big data issue, big data compression technique is desired. CS is a promising technique for big data compression and it is based on the theory that the sparse information in a transformation domain can be recovered from a reduced number of measurements, which conquer the traditional Nyquist-Shannon sampling theorem [88,89]. Hence, it got pervasive attention in radio frequency (RF) signal detection [90,91], biomedical applications [92–94] and CS-based imaging [23,95–100].

2.5.1. Photonic compressed sensing

CS, which aims at reducing the number of measurements via utilizing the sparsity of the desired imaging or signal information, is an extensively used sampling modal that offers a high-efficient data acquisition process. Figure 2. 17 shows the process of CS. A piece of sparse imaging or signal information with a data length of N is measured iteratively M times ($M < N$), then the data is acquired and the image is reconstructed via using a recovery algorithm.

Based on the CS algorithm, which can be expressed as [101]

$$\hat{X} = \arg\min \|v\|_{l_1} \quad \text{subject to } Av = Y \tag{2.45}$$

where $\|v\|_{l_1}$ indicates that the number of nonzero entries in vector **v**. **X** is a N × 1 matrix representing the input sparse information with a data length of N, **Y** is a M × 1 matrix denoting the measured results, M is the number of measurements, **A** is the measurement matrix, has a dimension of M × N, is defined as **A=DIR**, in which matrix **D** is a M × N matrix denoting a down sampling process, **I** is a N × N matrix indicating the low-pass filter response, **R** is a diagonal N × N matrix denoting a random sequence. The compression ratio is M/N in this CS method.

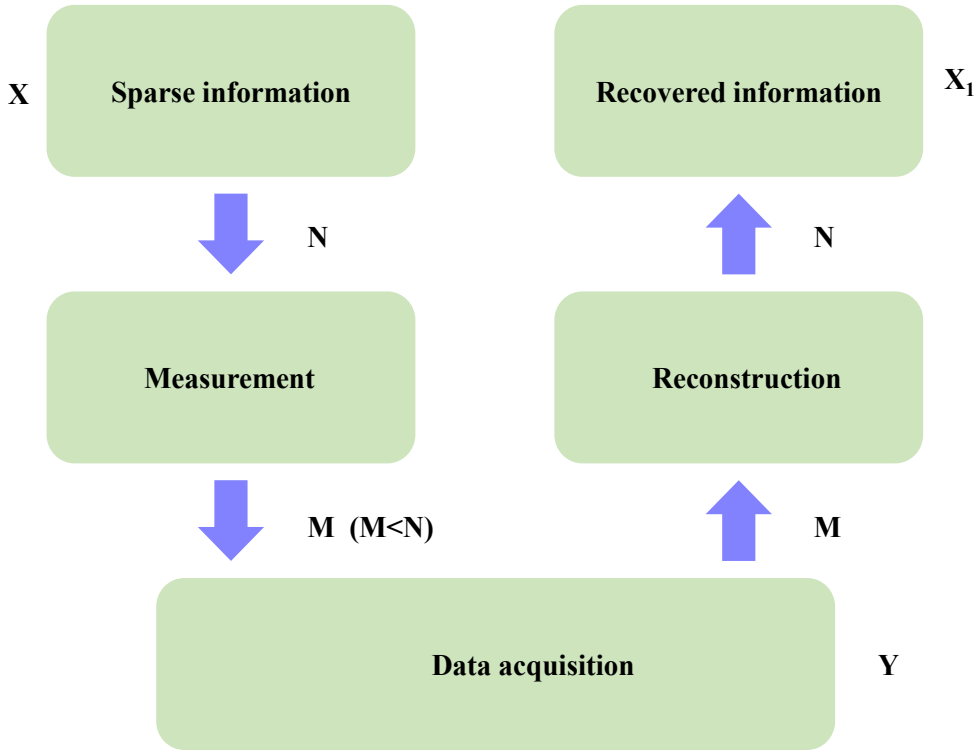

Figure 2.17 The process of CS [90].

To reconstruct the $\mathbf{X_1}$, l_1-minimization is employed and it can be expressed as

$$\hat{X} = \min \|v\|_{l_1} \quad \text{subject to } \|Y - Av\|_2 \le \sigma \tag{2.46}$$

The above case considered the noise of the system, for example, $\mathbf{Y}=\mathbf{AX}_1+\mathbf{e}$, where **e** is the noised induced by unknown perturbation bounded by $\|e\|_2 \leq \sigma$.

In CS method, a pseudorandom bit sequence (PRBS) is a necessity in the algorithm, this type of CS method is defined as time domain CS, which could perform an ultrafast speed of tens of GHz [95,97,98], with the sacrifice of using expensive devices. Traditionally, spatial light modulator (SLM) or digital micromirror devices (DMD) is employed to perform free-space all-optical imaging [8,102], this could be defined as spatial domain CS. Although the cost of such CS system is lower, the speed of such system is limited to tens of KHz.

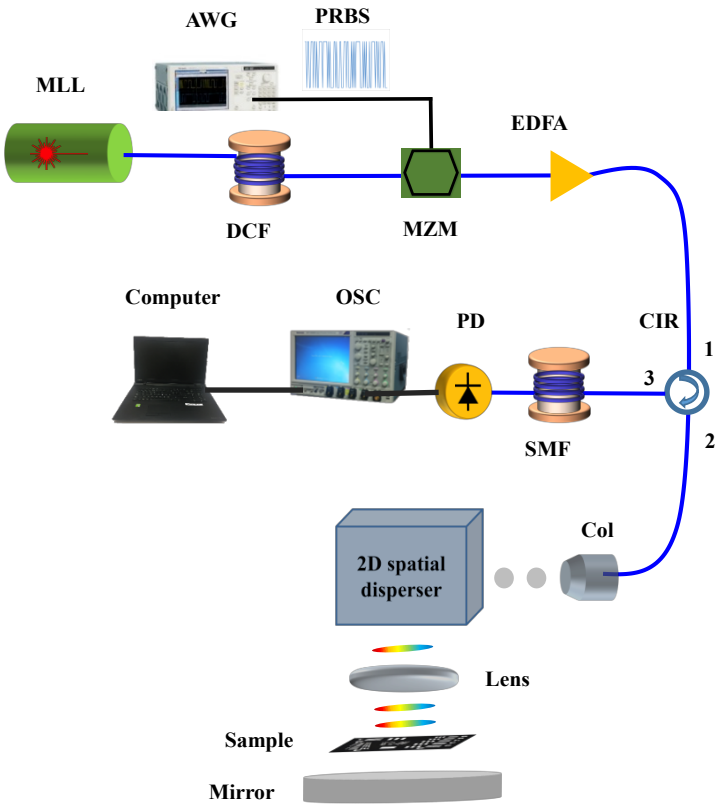

Figure 2.18 Diagram of CS imaging based on STEAM systems [98].

Due to the sparse feature of nature images, CS technique is widely used in the imaging fields, especially when the imaging system is combined with PTS, where a massive amount of data in the imaging system is produced. Figure 2. 18 shows the diagram of CS technique applied in the PTS based STEAM imaging system [98]. In the system, a random and iterative PRBS signal train from AWG is used to drive

MZM, where the time-stretched optical pulses are modulated by the PRBS signal train. Another difference compared to normal STEAM imaging system is after the circulator, a matched certain length of single mode fibre (SMF) to compensating DCF is exploited to compress each time-stretched pulse to one data, therefore, a low bandwidth PD and oscilloscope can be utilized for pulse train detection.

2.5.2. Anamorphic stretch transformation

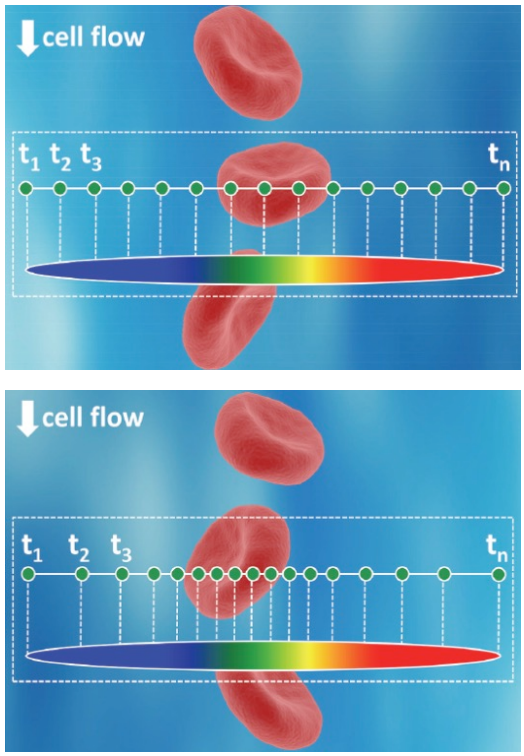

Figure 2.19 Schematic of (a) linear and (b) nonlinear wavelength to time mapping process [103].

Another data compression method based on the nonlinear mapping between wavelength and time using CFBG is presented in chapter 2.2.2 when the third order coefficient of propagation constant is considered. This approach is called anamorphic time stretch transformation [36,103,104], which is another solution for data compression.

In chapter 2.2.2, the nonlinear mapping between wavelength and time is discussed, where indicating this effect could be exploited in data compression. In Figure 2. 19,

the contrast of linear (a) and nonlinear (b) mapping of wavelength to time processed is illustrated. The nonlinear time-stretch between wavelength and time is also known as anamorphic stretch transformation (AST) [103], which could be induced via using a CFBG. Figure 2. 19 shows how to use AST for imaging based on the sparse characteristic of the imaging, part of the imaging with more information will be detected with more data component, vice versa. In other words, AST changed the sampling rate from uniform to a varied form depending on the distribution of imaging information, as a result, data compression is obtained.

2.6. Summary

A detailed background study on optical devices, techniques and system structures in PTS based ultrafast SPI systems are presented. The TFG, which is a novel in-fibre device with the various potential applications, is introduced with classification of TFBG, RTFG, and Ex-TFG. It's also discussed that in RTFG, the 45° TFG, which has maximum angular dispersion as an in-fibre diffractive device, could substitute the traditional bulky grating in PTS based imaging system. As a result, a stable, simplified and compact ultrafast SPI system can be obtained via the utilization of 45° TFG.

In addition, the STEAM based ultrafast imaging systems are investigated in principle and applications. The STEAM system contains two fundamental steps, which are uniform one-to-one mapping between space and wavelength / spectrum and uniform one-to-one mapping between wavelength / spectrum and time. The uniform mapping of space and wavelength, namely, space to spectrum conversion, which is normally based on the feature of diffractive devices, such as traditional bulky gratings, is investigated. The uniform mapping of wavelength and time, also known as linear wavelength to time conversion, is demonstrated. The wavelength to time conversion process is achieved via the dispersion of optical medium, such DCF. The chirped mapping between wavelength and time is discussed, which is induced by the third order of propagation constant, such as CFBG. The STEAM

systems are investigated to be in a various range of imaging applications, such as opaque or transparent biomedical objects ultrafast imaging.

Besides, the MMF is reviewed in classification and analysis. Step-index MMF and graded-index MMF with the estimation of maximum number of modes that can be supported by it is investigated. Light travelling in MMF will lead to randomization of phase, polarization and distribution of intensity profile, which could be utilized in imaging systems. MMF for the imaging applications, such as wavefront shaping, spatio-temporal investigation, and stable light transmission in MMF, are also reviewed.

Finally, Data compression optical system are introduced. CS technique, which is widely used in imaging applications in order to perform data compression due to the sparse feature of nature images, is investigated in theory and examples. The process of CS algorithm is reviewed in details. In imaging applications, CS needs random patterns, which could be produced via a SLM, DMD or MZM combined with signal generator. The performance of CS technique in ultrafast imaging systems reported in previous works is reviewed, which has the advantage of addressing the improvement in data process, reducing the high volume of data that needs to be processed in the traditional ultrafast SPI systems. Nonlinear mapping between wavelength and time, namely, AST, can also obtain data compression via using a CFBG based on nonlinear sampling rate, the examples of such technique is also reviewed.

CHAPTER 3: HIGHLY EFFICIENT TIME STRETCH IMAGING BASED ON 45° TFG

3.1. Introduction

In this chapter, we tested the character of 45° TFG in experiment confirming it has great potential to replace the bulky diffraction grating in traditional STEAM imaging system with the advantages of high efficiency and compact size. For the first time we employed the 45° TFG for highly efficient, in-fibre compact size and low-cost 1D and 2D spectrally encoded imaging systems. Then an ultrafast optical imaging system based STEAM structure using the 45° TFG with ultrafast optical imaging speed achieved and the experimental result shows it has better spatial resolution compared to the usage of bulky diffraction grating under same system setup. Finally, the 45° TFG is treated as a beam steering device using in free-space optical wireless communication system.

3.2. Performance of 45° TFG as a diffractive device for imaging application

In 45° TFG, the forward propagating light is coupled into radiation modes owing to its largely tilted facet angle, leading to direct side lateral diffraction into free space. Its wide operation window (several hundred nm) and wavelength dependent diffraction angle make the 45° TFG an excellent candidate for in-fibre lateral diffraction. The concept of 45° TFG is shown in Figure 3. 1 (a) and (b). Figure 3.1 (a) illustrates its structure with feature of wavelength-dependent side lateral diffraction when broadband incident forward propagating light propagated through it. As the investigation of RTFG in previous chapter, the wavelength-dependent lateral diffraction of 45° TFG, namely, angular dispersion of 45° TFG, which

characterizes the change of diffraction angle corresponding to a small change in wavelength, is given by [51]

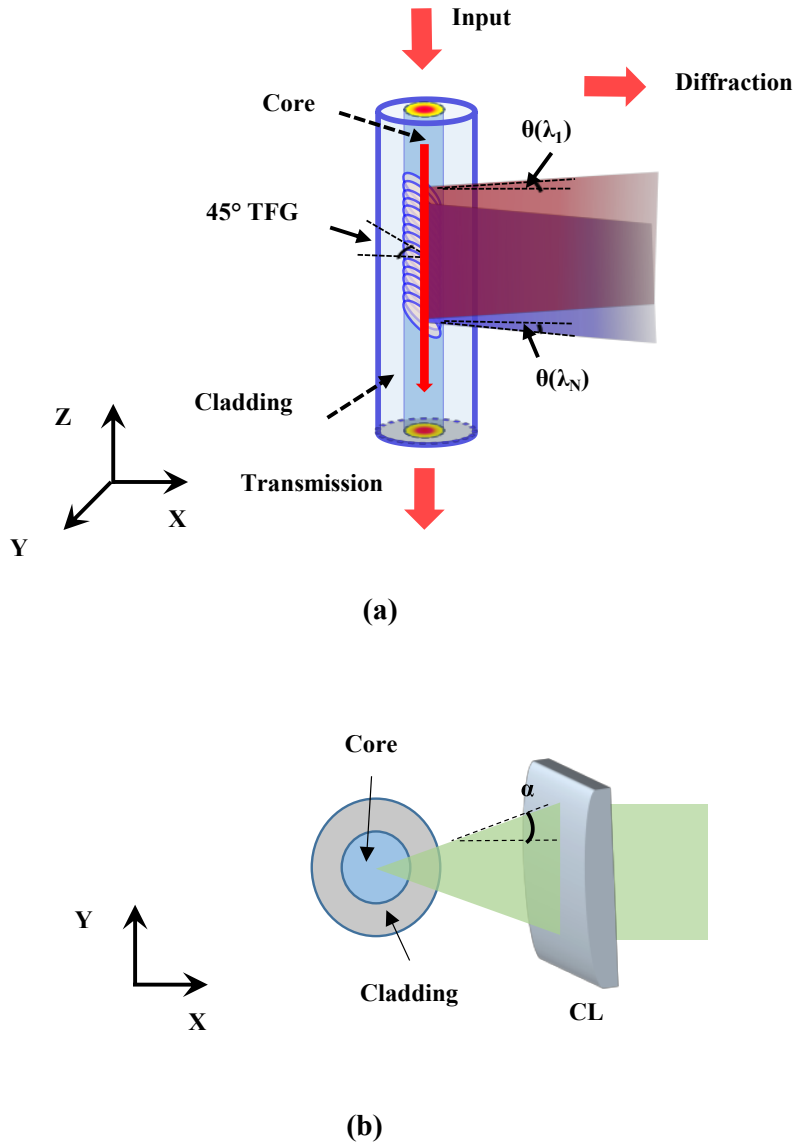

Figure 3.1 Diagram showing the structure of the 45° TFG as an in-fibre diffractive element and (a) broadband incident light is diffracted from fibre core into free space with wavelength-dependent lateral diffraction, (b) Divergent output characteristics in radial plane.

$$D = \frac{d\theta(\lambda)}{d\lambda} = \frac{\sin(2\theta)}{\lambda} = \frac{1}{\lambda} \tag{3.1}$$

where λ is the wavelength of incident light and θ is the angle of lateral diffraction. Apparently, a tilt angle of 45° ensures the maximum angular dispersion for a given

optical wavelength. For light of 1550 nm, the theoretical result in the fibre core is approximately 0.037°/nm.

Figure 3. 1(b) shows the radial plane view of its divergent output characteristics, i.e. lateral diffraction. The emitted light beam is divergent in the radial direction due to the cylindrical shape of the fibre. For imaging purpose, a cylindrical lens is therefore required to collimate the light beam in the vertical (Y) direction.

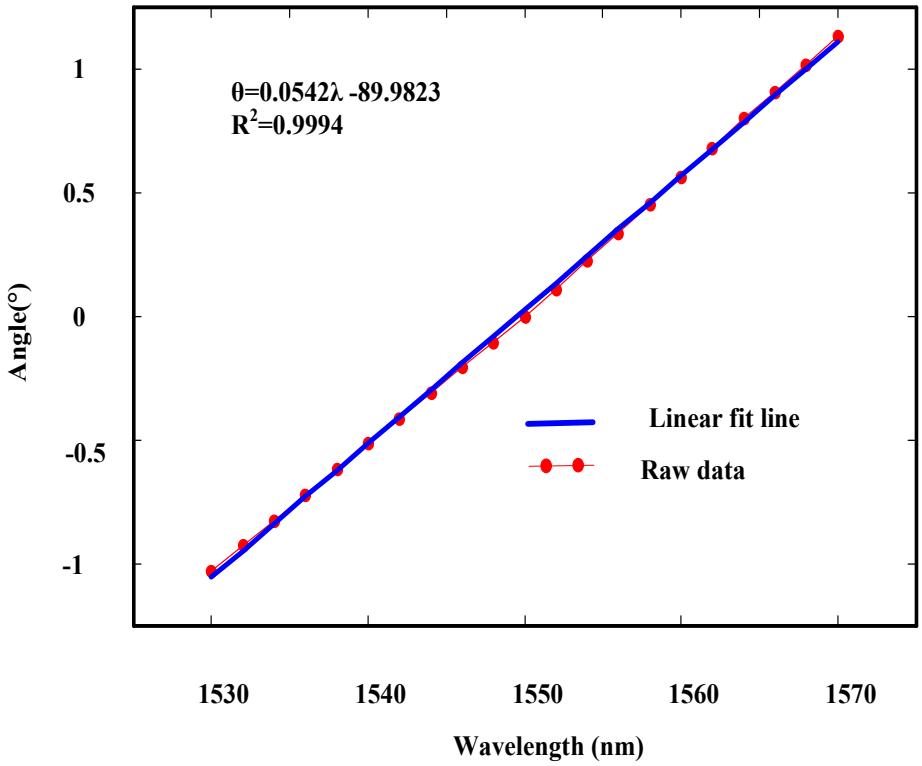

Figure 3.2 Measured angular dispersion of the 45° TFG (red-dotted black line) with linear fitting result (blue line).

The angular dispersion of 45° TFG is experimentally measured using a 45° TFG with a period of 748 nm. The system setup is based on Figure 3.1 (a), that each wavelength reaches different points when propagating 1 meter. By measuring the distance among wavelengths, the angular dispersion can be calculated. Figure 3. 2 shows the relation between the diffraction angle and the illuminating wavelength (red-dotted line) within a 40 nm spectral band (1530–1570 nm). A linear fitting (blue line) is also plotted in the Figure 3. 2, which confirms that the diffraction angle and the illuminating wavelength has very good linear relation, with a correlation coefficient of 0.9994. The angular dispersion of the 45° TFG is thus

estimated to be 0.054°/nm in the free space from the measured results. However, the theoretical value of angular dispersion of 45° TFG is 0.037°/nm. This is because the refraction at the interfaces among fibre core (refraction index of 1.448), fibre cladding (refraction index of 1.444), and air (refraction index of 1) and are not taking into consideration. When considering these interfaces by

$$n_1 \sin\theta_1 = n_2 \sin\theta_2 = n_3 \sin\theta_3 \tag{3.2}$$

where n_1, n_2 and n_3, θ_1, θ_2 and θ_3 is the refractive index, refractive angle of fibre core, fibre cladding and air respectively. After recorrected by considering the diffraction among interfaces, the theoretical value of angular dispersion of 45° TFG in the free space is 0.053°/nm, which is in good agreement and very close to the experimental result of 0.054°/nm.

The 45° tilted grating structure generates cylindrical asymmetry in the fibre core, making the 45° TFG a highly polarization dependent device. One unique feature of 45° TFGs is that only s-polarized light can be significantly radiated out of the fibre core, and p-polarized light has a zero transmission loss, making the polarization dependent loss (PDL) as high as ~40 dB [105]. This unique characteristic allows us to develop it as a highly efficient diffractive optical fibre element [11,12,69] with the potential application as in-line fibre polarizer [65]. To ensure high diffraction efficiency, the input light beam should be linearly polarized.

A 45° TFG with a period of 748 nm was fabricated to function as an efficient in-fibre diffractive element. The 45° TFG was written directly into a standard telecom single-mode fibre (SMF-28) using the standard scanning phase mask technique with continuous-wave UV-light at 244 nm. To achieve the required 45° slanted grating fringes, the phase mask was rotated by 33.3°. The fabricated 45° TFG is 24 mm long, ensuring high efficiency of diffraction. There is an exponential decay for the emitted intensity profile along the propagation direction.

To measure the diffraction efficiency of the 45° TFG, an experiment is performed and the result is illustrated in Figure 3. 3.

As there is no Bragg reflection nor coupling to cladding modes in the 45° TFG, when the incident light propagates through the TFG, a portion of it (s-polarized light) is diffracted into open space while the remaining part (p-polarized light) keeps propagating in the fibre core. Therefore, diffraction efficiency of the TFG can be estimated by the ratio between the diffracted optical power and the sum of diffracted and transmitted power, which can be expressed as

$$\eta = \frac{P_{diff}(\lambda)}{P_{in}(\lambda)} = \frac{P_{diff}(\lambda)}{P_{diff}(\lambda) + P_{trans}(\lambda)} \tag{3.3}$$

where $P_{in}(\lambda)$, $P_{diff}(\lambda)$, and $P_{trans}(\lambda)$, are the total input and diffracted and transmitted optical power, respectively.

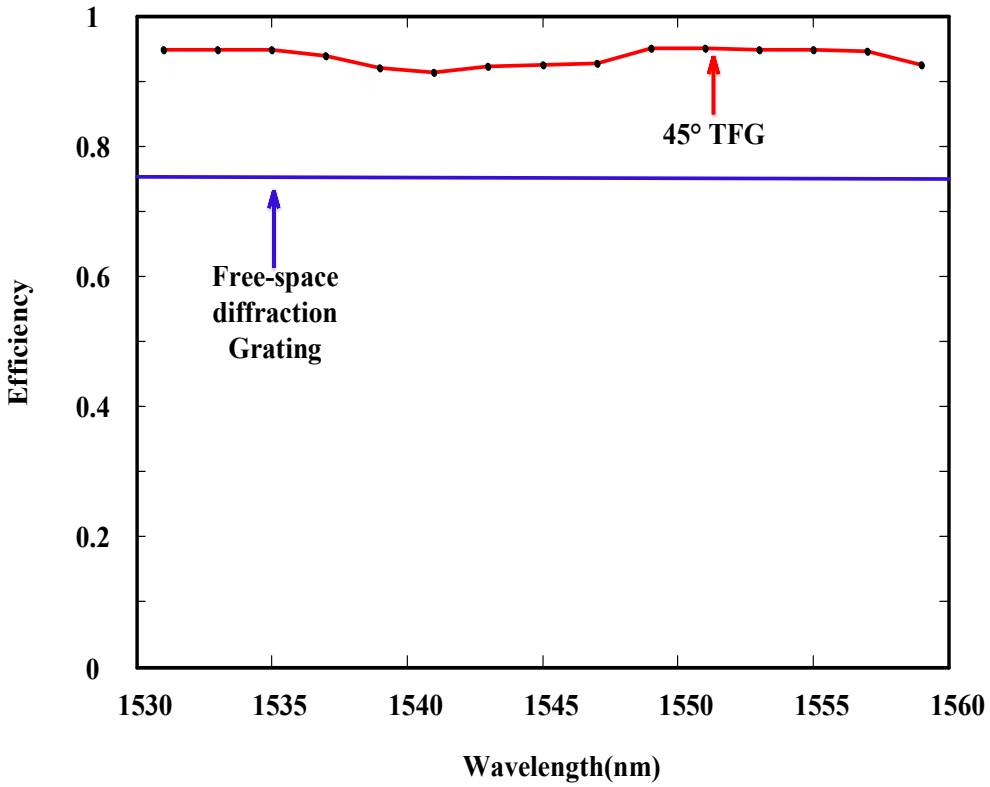

Figure 3.3 Measured maximum lateral diffraction efficiency of the 45° TFG at a properly controlled polarization state (red line), efficiency of normal free-space diffraction gratings (blue line).

As the 45° TFG has a strong sensitivity to the polarization state of the incident light due to circular asymmetric structure of the fibre core, the power of lateral diffraction from the 45° TFG is largely dependent on the polarization state of the incident light with respect to the tilted grating structures. Figure 3.3 shows the

measured maximum diffraction efficiency of 45° TFG at a properly controlled polarization state of the linearly polarized incident light (red line). The average diffraction efficiency of the TFG is as high as 97% with an average value of 93.5% across the broad wavelength range from 1530 to 1560 nm, which is much higher than that of normal free-space diffraction gratings (up to 75%, blue line [106]). This verifies the utility of the 45° TFG as a highly efficient in-fibre diffractive element.

Noting that the diffraction efficiency of a 45° TFG is also dependent on the length of the 45° TFG. The longer the 45° TFG is, the higher the efficiency is, and vice versa. However, there is an exponential decay in propagation direction for the emitted intensity profile. The diffracted beam pattern from the side of the 45° TFG for a single input wavelength of 1545 nm is measured using a highly sensitive infrared sensor card and is shown in the inset of Figure 3.4. It can be seen that our 24 mm long TFG offers strong diffraction as well as exponential decay.

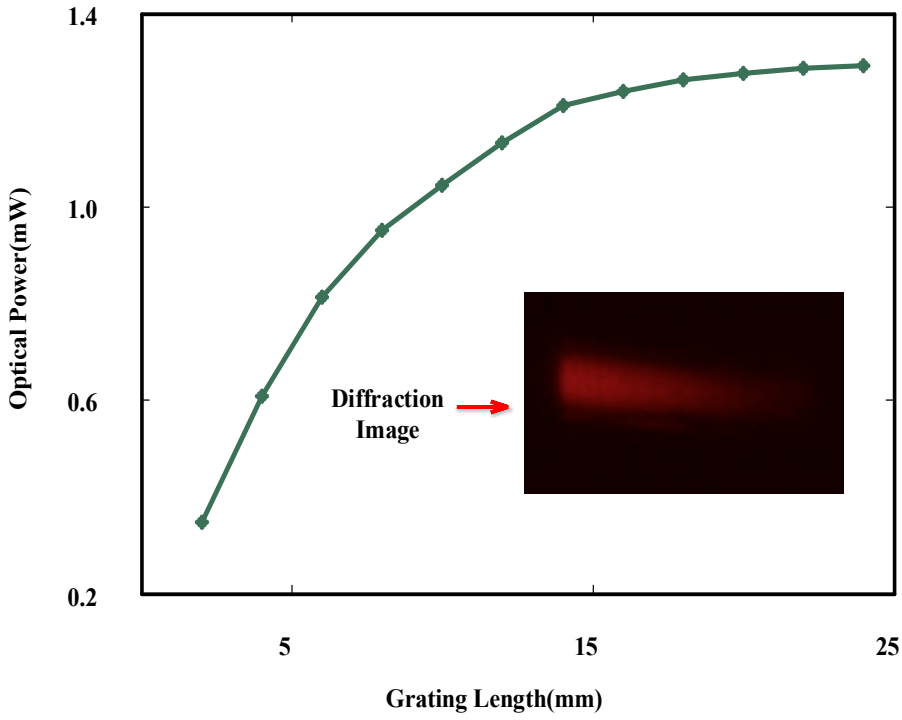

Figure 3.4 Total emitted optical power with different lengths of 45° TFG. A 24 mm long TFG was used and measurements were done by blocking part of the TFG region. Inset: the image of diffraction pattern showing exponential decay.

The exponential decay of 45° TFG is analysed and the optical power along with the length of the 45° TFG is experimentally measured and the result is illustrated in Figure 3. 4, which shows for a 24mm length of 45° TFG as an example, 74% of its power lies in the first one third length (8mm), while 87% of its power lies in the first half (12mm). Noting that the beam size of the diffracted light is determined by the active length of the 45° TFG, hence the length of the 45° TFG should be carefully choose to ensure good diffraction efficiency, and at the same time to avoid strong decay in the emitted intensity profile along the axial direction.

Also Figure 3. 4 confirmed the conclusion that the optical power from 45° TFG has exponential decay (green line), and the relationship between incident optical power and the length of the 45° TFG is shown as

$$P_{in} = \exp(\alpha \cdot 1 + \beta) \tag{3.4}$$

where α and β are constant coefficient and l is the length of the 45° TFG.

3.3. 45° TFG for highly efficient spectrum encoded imaging

Chapter 3.2 theoretically investigated and experimentally demonstrated the performance of 45° TFG, which confirms the 45° TFG can be regarded as a high efficient, compact in-fibre diffractive device. The 45° TFGs can replace the free-space ruled or holographic bulky diffraction gratings that used in the traditional SEI systems as diffractive devices, which encodes the spatial information (image) into the optical spectrum via the wavelength to space linear mapping.

Compared to 45° TFGs, the traditional free-space ruled or holographic bulky diffraction gratings [15,17,24,26–28,30,38,107] suffer from some inherent drawbacks in the imaging applications. First of all, in order to achieve high angular dispersion for high-quality imaging, diffraction gratings with high groove density

are usually required, which are however high cost and bulky, and hinder miniaturization of the imaging system in real practice. In addition, normal ruled or holographic diffraction gratings fall short in diffraction efficiency (usually up to 75%) in a non-Littrow configuration due to the inherent strong zeroth-order reflection. Besides, high coupling loss between free-space diffraction gratings and optical fibres or CFBGs, which provide chromatic dispersion for time stretch, significantly reduces the quality of signal or image. In particular, many time stretch imaging systems are based on a reflection configuration. Reflected light from the target is diffracted by the diffraction grating for the second time to be coupled back into optical fibre with the help of a fibre collimator. Use of a fibre collimator and double diffractions from the diffraction gratings lead to high coupling loss. More importantly, what is surprisingly overlooked in existing free-space diffraction grating based imaging systems, is the sacrificed imaging resolution (lower than diffraction limit) due to non-full-aperture illumination for individual wavelengths, which is resulted from large angular dispersion of free-space diffraction gratings. These technical issues hinder widespread application of SEI techniques in real practice where low-cost, energy-efficient, and compact imaging devices are desired.

To address these challenges, an optimal solution of using 45° TFGs as a highly efficient, compact, and in-fibre lateral diffractive element in the traditional SEI systems is proposed, which could eliminate the need for bulky and lossy free-space diffraction gratings. For a 45° TFG operating at 1550 nm band has a grating period of serval hundreds nm, the equivalent grating groove density is much higher than a conventional free-space diffraction grating. In addition, the 45° tilted grating structure generates cylindrical asymmetry in the fibre core, making the 45° TFG highly polarization dependent with a significantly enhanced diffraction efficiency (up to 97%). Also, the use of 45° TFG in SEI systems will completely eliminate the need for bulky free-space diffraction gratings for spectral encoding and avoid complex and lossy light coupling between dispersive fibres and free-space components. Beside, 45° TFG is inherently compatible with optical fibres that provide chromatic dispersion, which makes ultrafast optical imaging possible. This conceptually new design of all-fibre SEI scheme using 45° TFG enables highly efficient and miniaturized SEI systems for practical imaging applications. More importantly, the 45° TFG enables almost full-aperture illumination for all

wavelengths due to its small angular dispersion value, leading to improved imaging resolution for a given imaging optics setup.

The schematic diagram of the highly efficient SEI system based on a 45° TFG is shown in Figure 3. 5. To provide broadband illuminating incident light, a wavelength swept laser (WSL, Agilent 8168E) was employed and it wavelength scanning was controlled by LabVIEW programmes. Here a CCD camera or sophisticated optical spectrum analyser (OSA) is not required for spectrum measurement, which can be done using a single-pixel photo-detector in a fast manner due to the usage of a tunable laser rather than a broadband light source. Light from the laser was launched into the fibre containing the 45° TFG, where light was diffracted into open space from fibre core through one side of the 45° TFG. A polarization controller (PC) was employed in the system to maximize the overall diffraction efficiency as the lateral diffraction of light is strongly polarization-dependent. The use of 45° TFG as an in-fibre diffractive element can significantly reduce the volume of the imaging system, the optical insertion loss and the complexity of the system as well as increase the efficiency and stability of the SEI system.

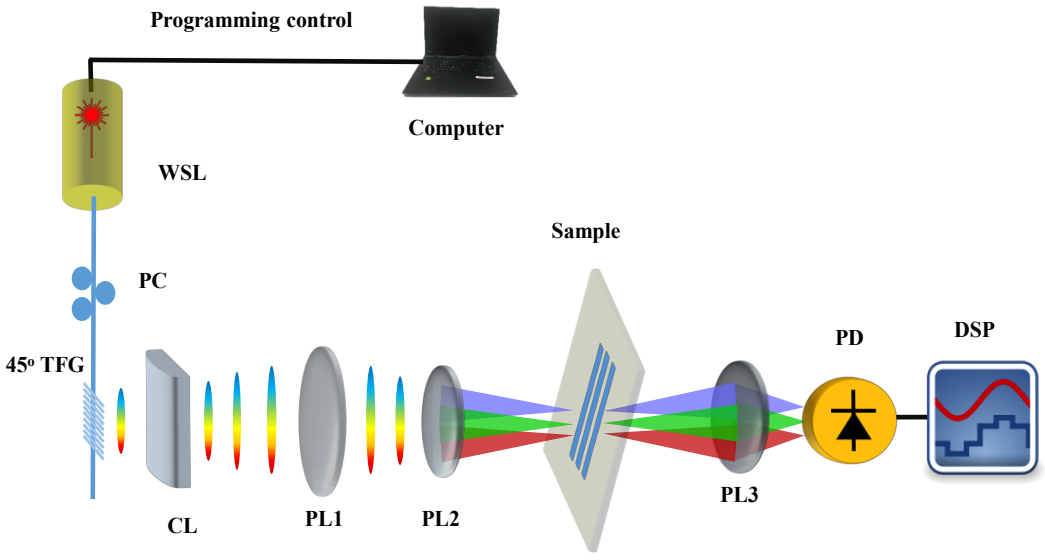

Figure 3.5 Schematic diagram of the SEI system based on a 45° TFG.

To obtain vertical beam collimation, a cylindrical lens with a focal length of 20 mm was placed after the 45° TFG. The beam-width of the diffracted light is determined

by the length of the 45° TFG. The diffracted light beams with different wavelengths are largely overlapped in space. Therefore, a lens set, consisting of two plano-convex lenses with focal lengths of 250 mm (PL1) and 200 mm (PL2), respectively, separated by 190 mm, is required to focus different colours of light into separate spatial coordinates on the object plane to achieve the unique linear one-to-one space-to-wavelength mapping. The lens set is placed 60mm after cylindrical lens (PL3). A custom-designed three-slot sample with a size of 2.0 mm by 2.0 mm is used as the test target and placed in the object plane. Our designed SEI system is operating in a transmission mode. After the diffracted light propagated through the target, the image was encoded onto the spectrum of the illuminating light thanks to the space-to-wavelength mapping. The spectrally encoded light is focused by another plano-convex lens and detected by a single-pixel PD. The SEI image is reconstructed in the digital domain by decoding the spectrally encoded information. Compared to conventional SEI systems that operate in reflection mode where the diffraction gratings also collect the reflected light for imaging [15,17,24,26–28,30,38,107], our proposed SEI system in transmission mode has the advantages of zero reflection disturbance and low reception loss. As light can be coupled back from free space to 45° TFG, this system can work in reflection mode as well, which is desired for non-transparent objects.

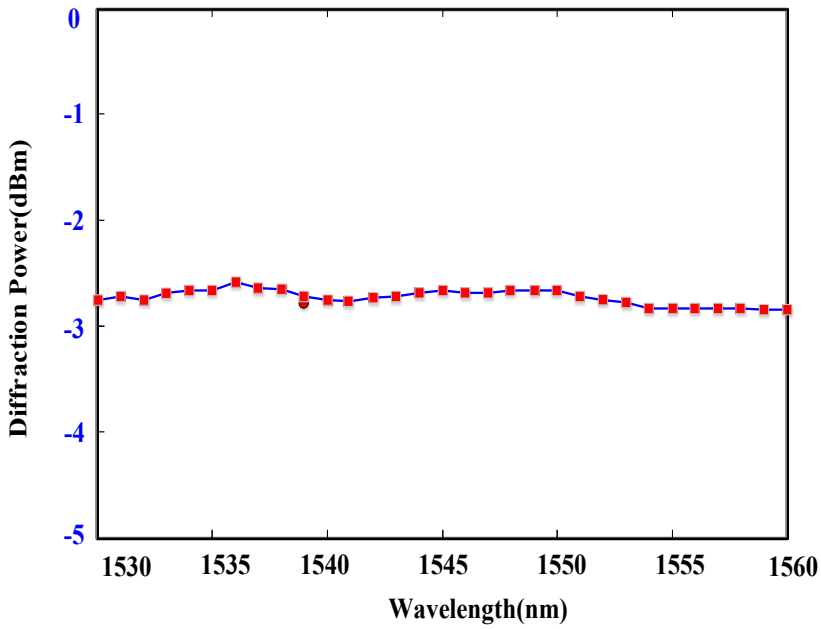

Figure 3.6 The intensity distribution of lateral diffraction of 45° TFG across a 30 nm spectral band from 1530 to1560 nm when a uniform incident light from WSL propagating through it TFG.

In addition, the intensity distribution of lateral diffraction of 45° TFG is experimentally investigated, which is described in Figure 3. 6. The result shows he uniform intensity distribution has a fluctuation less than 0.3 dB across the entire 30 nm bandwidth from 1530 to 1560nm. Note that the measured diffraction power was not corrected according to the photodetector's response efficiency, which has a negligible wavelength dependence characteristic (for a wavelength band less than 30nm).

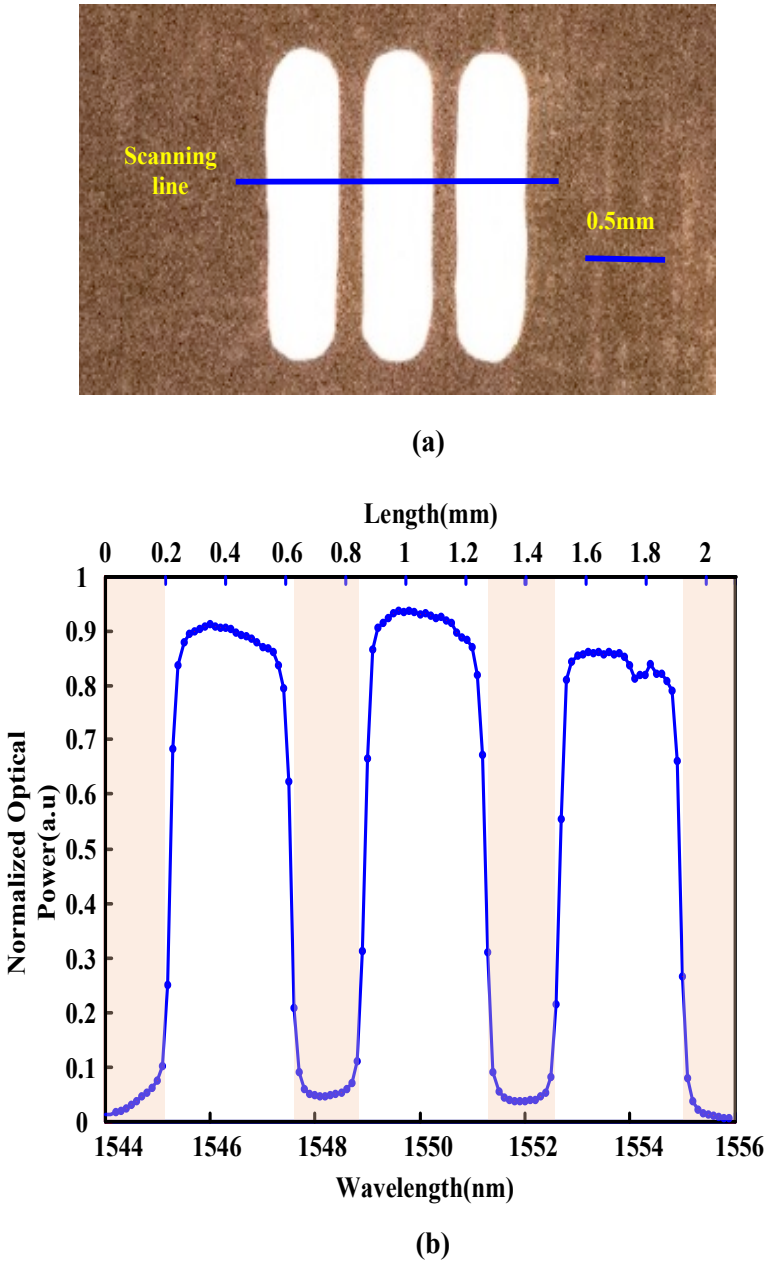

Figure 3.7 Imaging results using the 45° TFG-based SEI system. (a) CCD image of the three-slot sample; (b) 1D line scan image of the sample captured by the SEI system.

Spectrally encoded imaging of the three-slot sample is performed to verify our proposed 45° TFG-based SEI system. A CCD image of the custom-designed test target is shown in Figure 3. 7(a). The transparent slots were surrounded by an opaque substrate. Brown shadow areas represent the opaque parts. Each slot has a width of 0.4 mm and is 0.2 mm apart from the adjacent slots. As a proof-of-concept demonstration, 1D line scan imaging was carried out by rapidly sweeping the laser wavelength via LabVIEW programme controlling. The step of wavelength scanning is 0.1 nm and the scanning range is 12 nm from 1544 to 1556 nm. The reconstructed 1D image of the three-slot sample is shown in Figure 3. 7(b). The three-slot pattern is also shown in the Figure as a background. It clearly verifies that the reconstructed image matches well with the actual sample.

Lateral resolution of the 45° TFG-based SEI imaging can be estimated by measuring the point spread function (PSF) of a sharp slot edge in the target. In our proof-of-concept experiment, lateral resolution of the SEI system is estimated to be 28 μm. This lateral resolution can be easily improved by using a high-quality objective lens with shorter focal length and larger numerical aperture. Note that 1D line scan imaging is demonstrated in this work, and 2D imaging can be achieved by either using a galvanometer minor to provide the other scanning axis or moving the sample in the vertical direction, which is stated in the next part.

2D imaging of the 45° TFG-based SEI is achieved by moving the sample in the vertical direction. The schematic diagram of SEI system based on a 45° TFG is depicted in Figure 3. 8. Compared to the previous 1D imaging system, a lens set is also designed to focus different colours of light into separate spatial coordinates on the image plane. The lens set involves two plain convex lenses with focal lengths of 250 and 200 mm, respectively, separated by 130 mm instead of previous 190mm. A 2D sample of "**KENT**" with a size of 3.0 mm× 9.6 mm is used as the test target and placed in the image plane. The tuneable light beam of different wavelengths are scanned in x-axis while the 2D customer-designed sample is moved in y-axis to perform a 2D imaging. After the light propagates through the target, the image was encoded onto the spectrum of the illuminating light, thanks to the space-to-wavelength mapping. The spectrally encoded light is focused by another plain

convex lens and detected by a single-pixel free-space PD with a large active area of 6mm×6mm. Coupling loss from free space to the PD is minimal. The SEI image was finally reconstructed in the digital domain by decoding the spectrally encoded information.

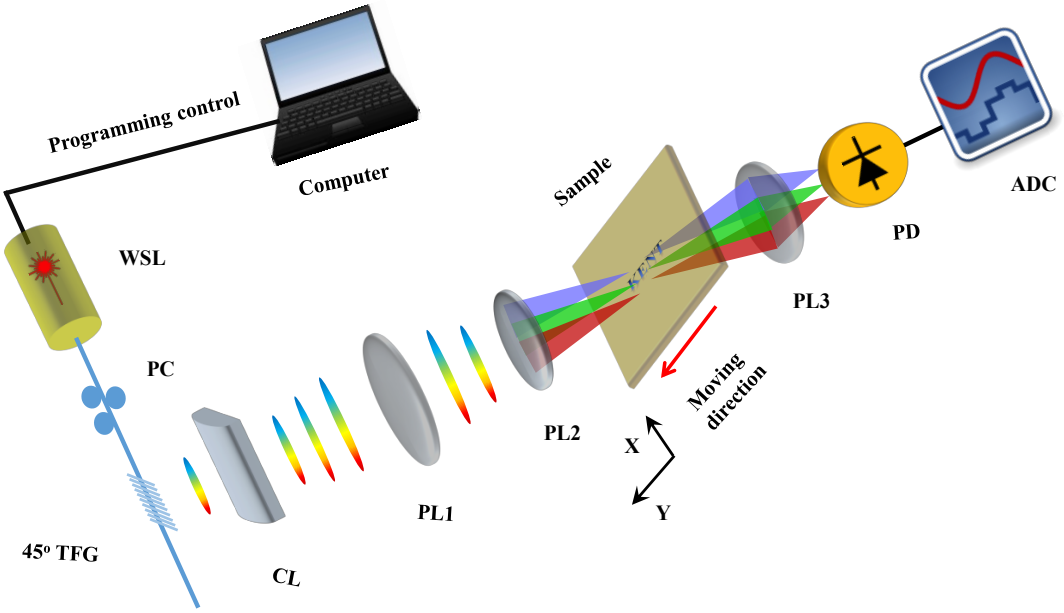

Figure 3.8 Schematic diagram of the SEI system based on a 45° TFG.

The test target is an opaque metal plate with four transparent letters "**KENT**". The width of strokes in the letters is around 0.6 mm. Figure 3. 9 (a) shows the CCD image of the customer-designed test target. As a proof-of-concept demonstration, vertical line scanning SEI imaging was carried out by rapidly sweeping the laser wavelength via controlling using LabVIEW programmes. The step of wavelength scanning is 0.1 nm, and the scanning range is 21.5 nm from 1530 to 1551.5 nm. The 2D imaging was achieved by moving the target in the horizontal direction with a step of 30 μm. The reconstructed dark-field 2D image of the target is shown in Figure 3. 9 (b), which clearly shows the word "KENT." The number of pixels in the captured target image is 320 × 215 (horizontal × vertical). The result firmly verifies the utility of the 45° TFG as an efficient diffractive element in SEI imaging.

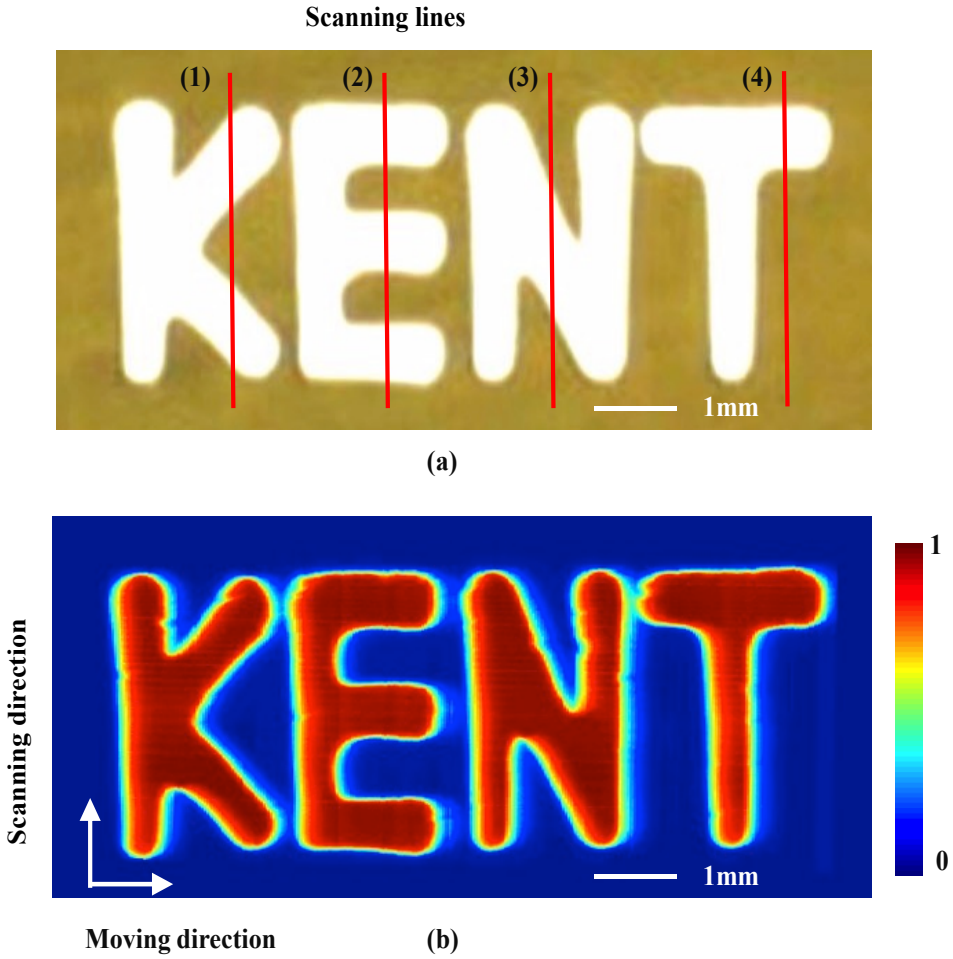

Figure 3.9 (a) CCD image of the customer-designed target with letters "KENT", which has a whole size of 3.0 mm× 9.6 mm and the strokes width of the letters are 0.6 mm. (b) Reconstructed dark-field 2D image obtained by the 45° TFG-based SEI system.

In Figure 3. 9 (a), the corresponding details of four scanning lines (1) to (4) are illustrated in Figure 3. 10 (1) to (4), respectively. The 1D line scanning results show four scanning lines matched quite well with the corresponding position of four-letter customer-designed "**KENT**" sample.

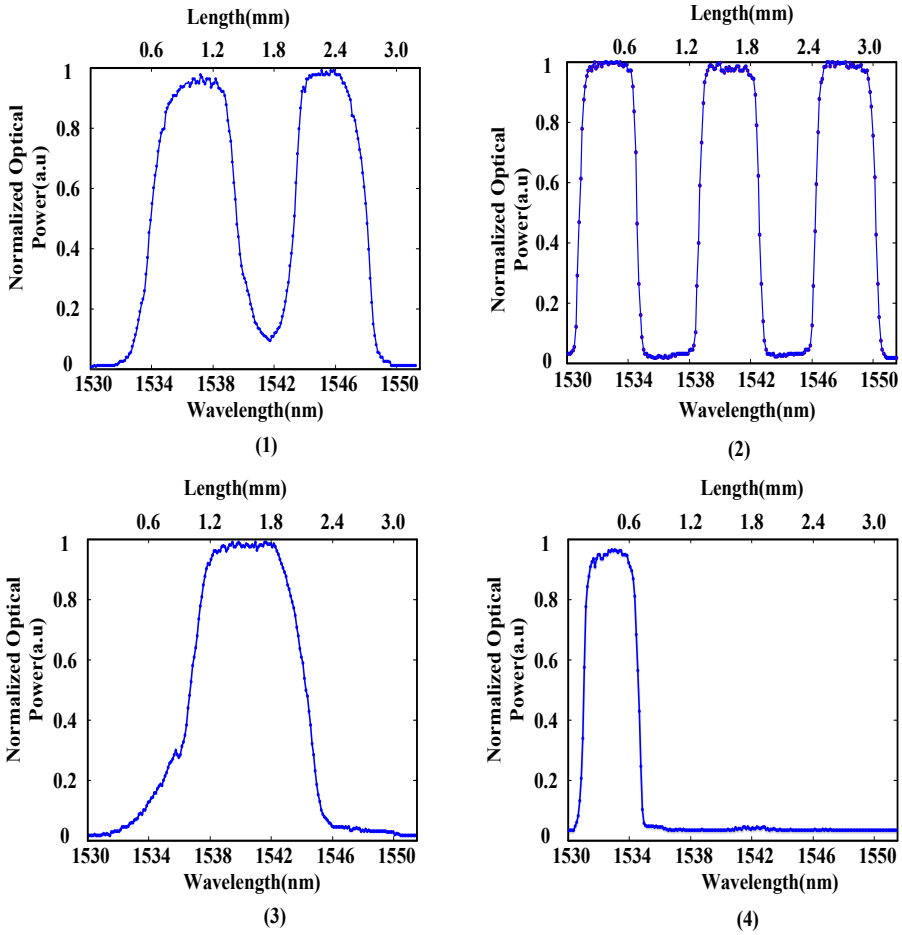

Figure 3.10 1D line scanning of (1) to (4) in the proposed SEI system, which shows the corresponding details of four scanning lines (1) to (4) in Figure 3. 9 (a). The results of four scanning lines matched the details in the corresponding position of four letters of customer-designed "**KENT**" sample.

Figure 3. 11 shows a vertical line scanning of the right part of letter "E," as shown in Figure 3. 9 (a) of position (2). The grey shadow areas represent the opaque parts. 45° TFG-enabled one-to-one mapping between the measured optical spectrum and the 1D target appears evident. Lateral resolution of the 45° TFG-based SEI system can be estimated by measuring the point-spread function (PSF) of a sharp edge (such as the edges of three horizontal strokes in letter "E"). In our proof-of-concept experiment, lateral resolution of the SEI system is estimated to be 42 μm, as shown in Figure 3. 11. Note the value of lateral resolution in 2D imaging in comparison 1D imaging is different, this is because the lens set, the beam width of incident light and the customer-designed samples are different.

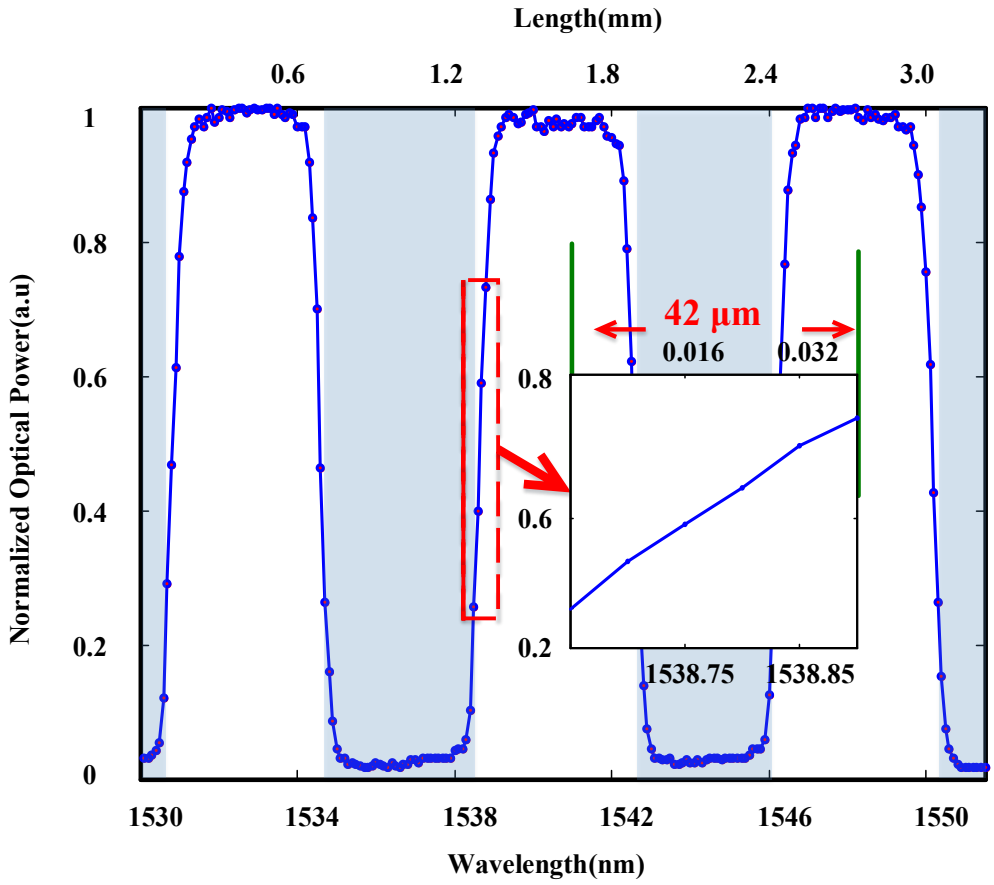

Figure 3.11 1D line scanning image of the right part of letter "E" in the target, obtained by the 45° TFG-based SEI system.

More study on the spatial resolution of our 45° TFG-based SEI system is conducted, with the results shown in Figure 3. 12. The diffraction-limited spatial resolution is calculated to be 43 μm based on the system parameters. According to the linear space-to-wavelength mapping relation, the wavelength scanning step of 0.1 nm corresponds to a spatial resolution of 14 μm in our system. Point A in Figure 3. 12 represents the measured resolution in our experiment, which is 42 μm. The diffraction-limited resolution is calculated as 43 μm (green line), and scanning step-limited resolution is shown in blue line. Therefore, the spatial resolution of our system is diffraction limited. In fact, the diffraction-limited resolution of our system can be improved by using a high-quality objective lens with shorter focal length and larger NA. This confirms a 45° TFG can be demonstrated as a highly efficient

diffractive element for SEI applications to substitute the traditional expensive and bulky free-space ruled or holographic diffraction gratings.

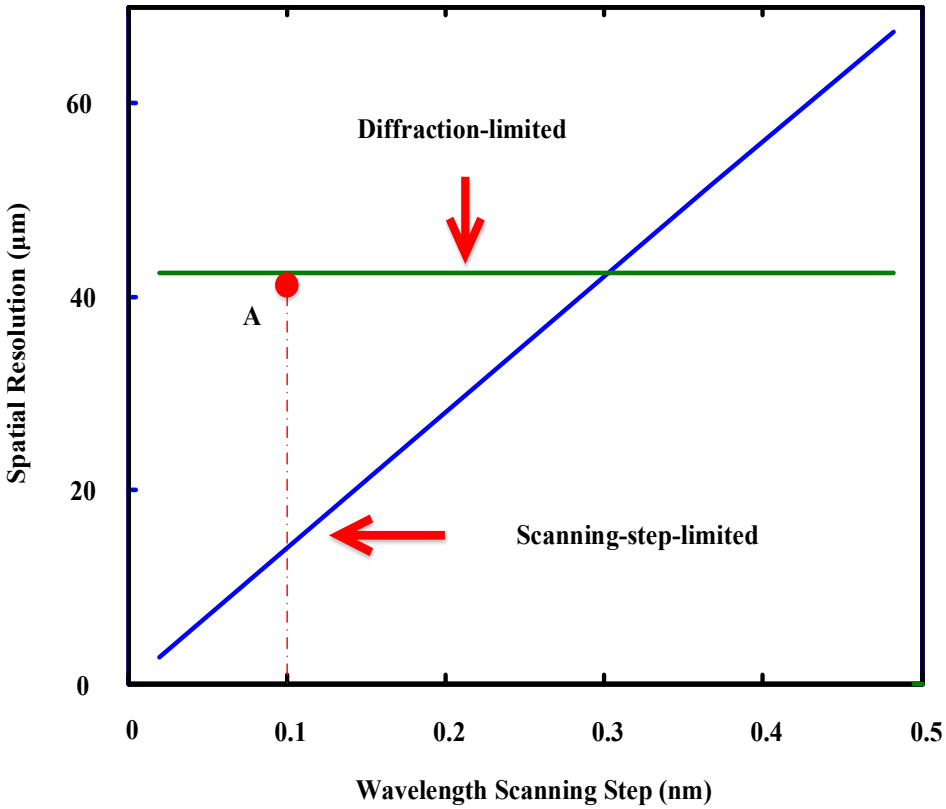

Figure 3.12 Spatial resolution of our 45° TFG-based SEI system.

The angular dispersion and diffracted beam size are intrinsic for a given 45° TFG. The field-of-view (FOV) and spatial resolution of the imaging system can be adjusted in the free space. For a given lens system, the two parameters are related: higher spatial resolution comes with a smaller FOV. However, the FOV can be further adjusted by changing the spectral bandwidth of the light source.

High-speed realization of SEI, such as STEAM [15,27,37,108,109], can be implemented by replacing the continuous-wave tunable laser with an ultrafast wavelength-swept light source. The imaging speed can be as high as 1 GHz [37]. The 45° TFG is particularly attractive in this ultrafast SEI scheme, as it is inherently compatible with optical fibres or chirped fibre Bragg gratings that

provide chromatic dispersion and the ultrafast imaging system based on a 45° TFG is presented in the following part.

3.4. 45° TFG for ultrafast highly efficient PTS based imaging system with improved spatial resolution

The previous parts presented the usage of 45° TFGs in spectrally encoded imaging systems. In this part, a PTS based ultrafast SPI system using a 45° TFG as an in-fibre compact high-efficient lateral diffraction device is presented. Also thanks to the beam size of each wavelength from a 45° TFG is the same as the whole beam size, in theory its spatial diffracted lateral resolution should be better than that of traditional free-space ruled or holographic bulky diffraction gratings. As a result, except for reduced physical volume/size of the imaging system, improved energy efficiency, and enhanced system stability, the proposed imaging system also has the advantage of improved spatial resolution.

3.4.1. Experimental setup

The utility of 45° TFG as an in-fibre diffraction grating for proposed ultrafast imaging system is first examined using a ray tracing software Zemax based on the 45° TFG characteristics and actual experimental setup, with the results shown in Figure 3. 13. A cylindrical lens (CL) with 20 mm focal length is placed after the 45° TFG to collimate the emitted optical beam in vertical direction. An imaging lens set consisting of two plano-convex lenses with focal lengths of 250 mm (PL1) and 200 mm (PL2) separated by 130mm is used to focus different wavelengths of light (from 1530 to 1570 nm) into different spatial positions on the object plane. The inset shows a zoom-in top view of 1-D illumination beam near the object plane. Wavelength-to-space mapping has been achieved and different wavelengths of light

are focused on the same object plane confirming a shallow depth of field. The field of view is 1.4 mm.

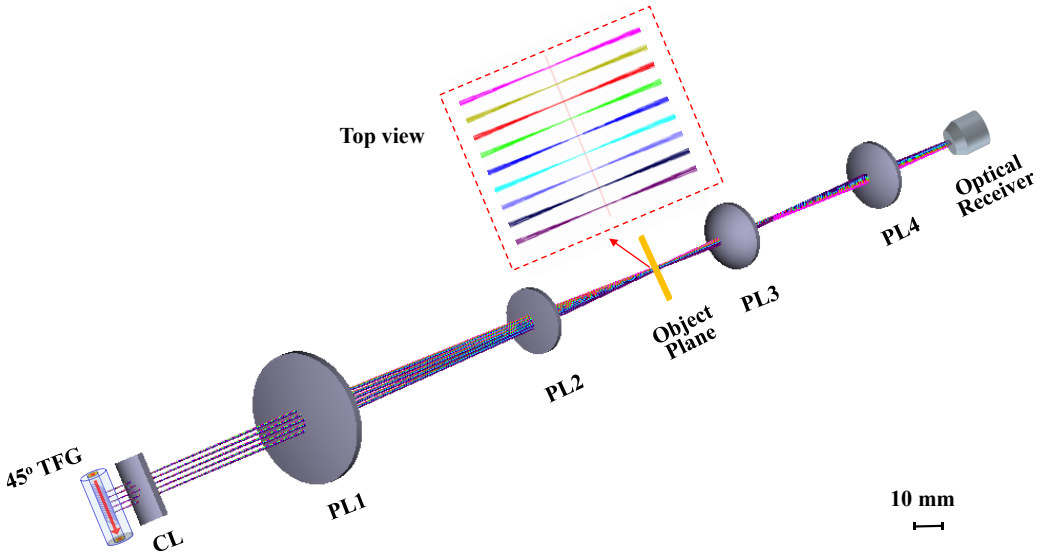

Figure 3.13 Ray-tracing simulation results using Zemax showing wavelength-to-space mapping for spectrally-encoded imaging with a shallow depth of field.

The utility of the fabricated 45° TFG in proposed ultrafast imaging system is experimentally demonstrated. We construct the imaging apparatus as shown in Figure 3. 14. A passively mode-locked fibre laser (Calmar Mendocino FP laser) produces a series of ultrashort optical pulses with full-width at half maximum (FWHM) pulse width of 800 fs and a repetition rate of 50 MHz. Optical pulses from the laser are largely stretched using DCFs with total dispersion of 1.03 ns/nm to achieve linear one-to-one wavelength-to-time mapping, followed by optical amplification using two EDFAs. Time-stretched and amplified optical pulses, with their polarization states properly controlled via a polarization controller, are launched into the 45° TFG with an effective length of 8 mm, where light is scattered out of fibre into free space based on the feature of wavelength-dependent side lateral diffraction of the 45° TFG. A lens set (as depicted in Figure 3. 13) focuses the illumination beam onto the object plane. The imaging system is working in transmission mode for the customer-designed sample.

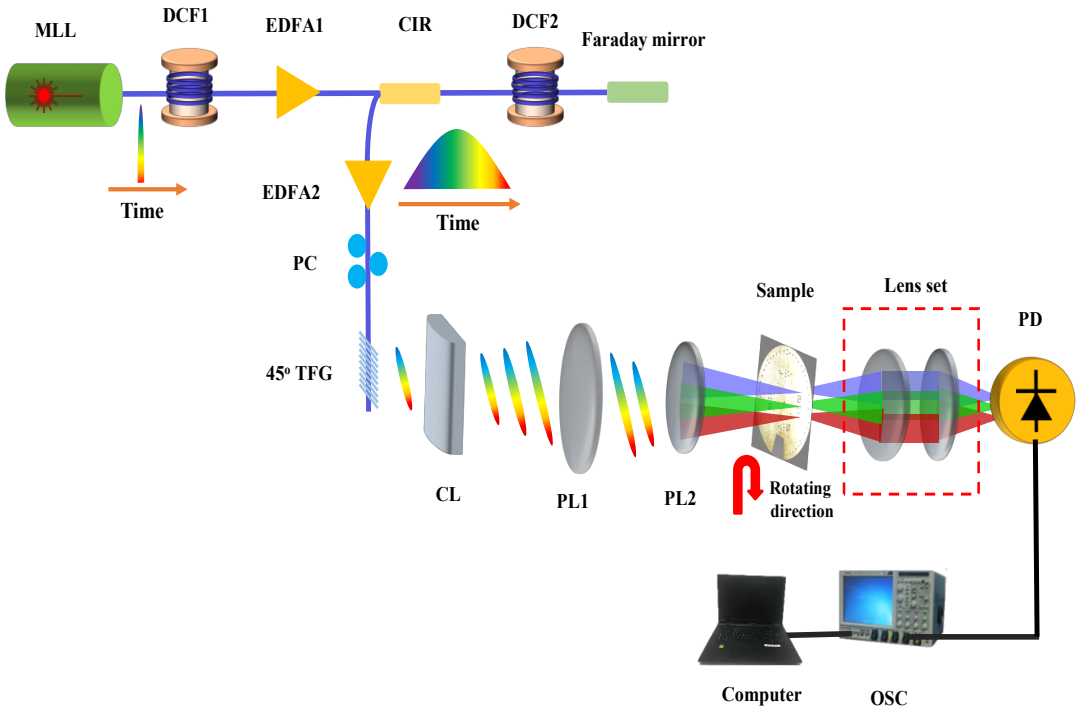

Figure 3.14 Schematic of PTS based ultrafast SPI system using a 45° TFG.

Due to the unique illumination conditions in the proposed ultrafast imaging system, light beam propagated through the object is not properly collimated (light with different wavelengths will have different propagation angles). To focus the light beam onto the high-speed free-space photodetector with a small sensitive area of 50 μm by 50 μm, another complex lens set with two stages of light collection after sample was arranged. In the first stage, a plano-convex lens with focal length of 30 mm is used to couple the light into a large NA MMF via a fibre collimator. Secondly, beam size of the output light from the MMF through a second collimator is reduced by 4 times using a telescope to match the sensing size of the high-speed photo-detector for efficient light detection.

The transmitted light after propagated the second lens set is coupled into a high-speed single-pixel photodetector with an analog bandwidth of 12 GHz. A high-speed oscilloscope (Tektronix DPO 72304DX) with a real-time sampling rate up to 100 GS/s captures and digitizes the time-encoded signal. Image of the object is reconstructed in the digital domain.

In our proposed ultrafast imaging system, the space-to-spectrum conversion is achieved based on the use of diffraction device, i. e. 45° TFG. This mapping relationship is first calibrated by sweeping the wavelength of a tunable continuous-wave laser and measuring the displacement of the focused laser spot on the object plane using an infrared beam profiler. This is characterized as 1 nm (spectrum) to 0.1mm (space). The spectrum-to-time conversion is based on dispersion-induced time stretch. As significant amount of dispersion is required, higher-order dispersion (dispersion slope) may have impact on the spectrum to time mapping process. Wavelength-dependent total GVD of the DCF used is characterized accurately by comparing interferograms in the wavelength domain and in the time domain. The nominal GVD value is 1040 ps/nm.

3.4.2. Result and discussions

The basic performance of the proposed PTS-based ultrafast SPI system using 45° TFG is demonstrated by imaging a standard resolution test chart, with the results shown in Figure 3. 15. Element 4 in group 1 is imaged. The effective field of view of 1D line scan imaging is 1.2 mm in vertical direction. 2D image of the resolution chart was obtained by moving the chart in the horizontal direction with a fine step of 15 μm, with result shown in Figure 3. 15(b). Stretched and time encoded optical pulses corresponding to four different line scans, which are shown in Figure 3. 15 (c), matched the corresponding positions of real imaging resolution target quite well after the linear wavelength-to-time and space-to-wavelength conversion. And spatial and temporal dispersion calibration of the system is carried out as previous analysis investigated, as a result, the image can be constructed precisely.

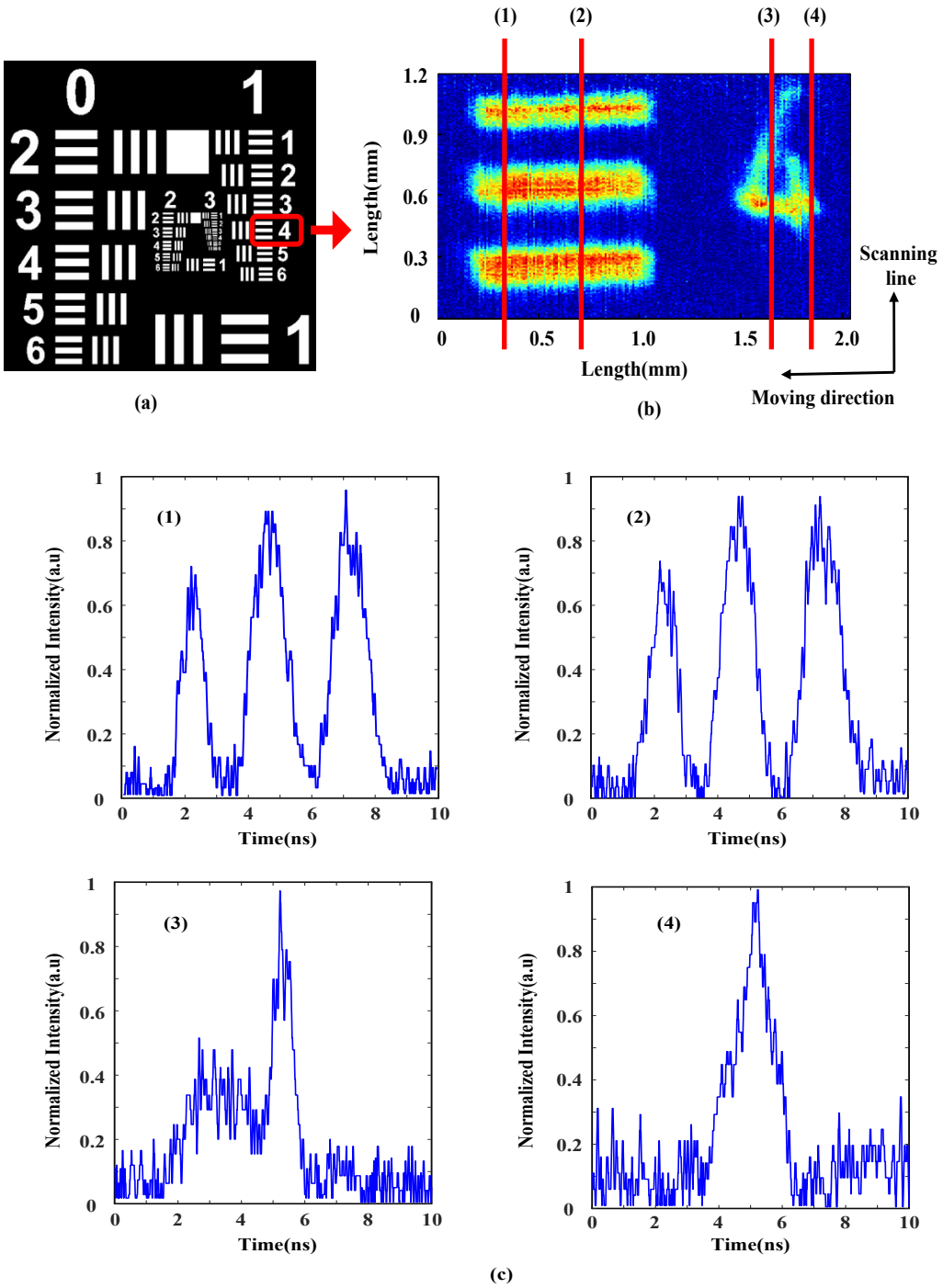

Figure 3.15 Imaging a stationary sample with the PTS-based ultrafast SPI system using 45° TFG. (a) CCD image of the resolution chart; (b) The reconstructed image of the selected part of the resolution chart. (c) Stretched and time-encoded optical waveforms (1) to (4) corresponding to four different line scans in (b) after the linear wavelength-to-time and space-to-wavelength conversion.

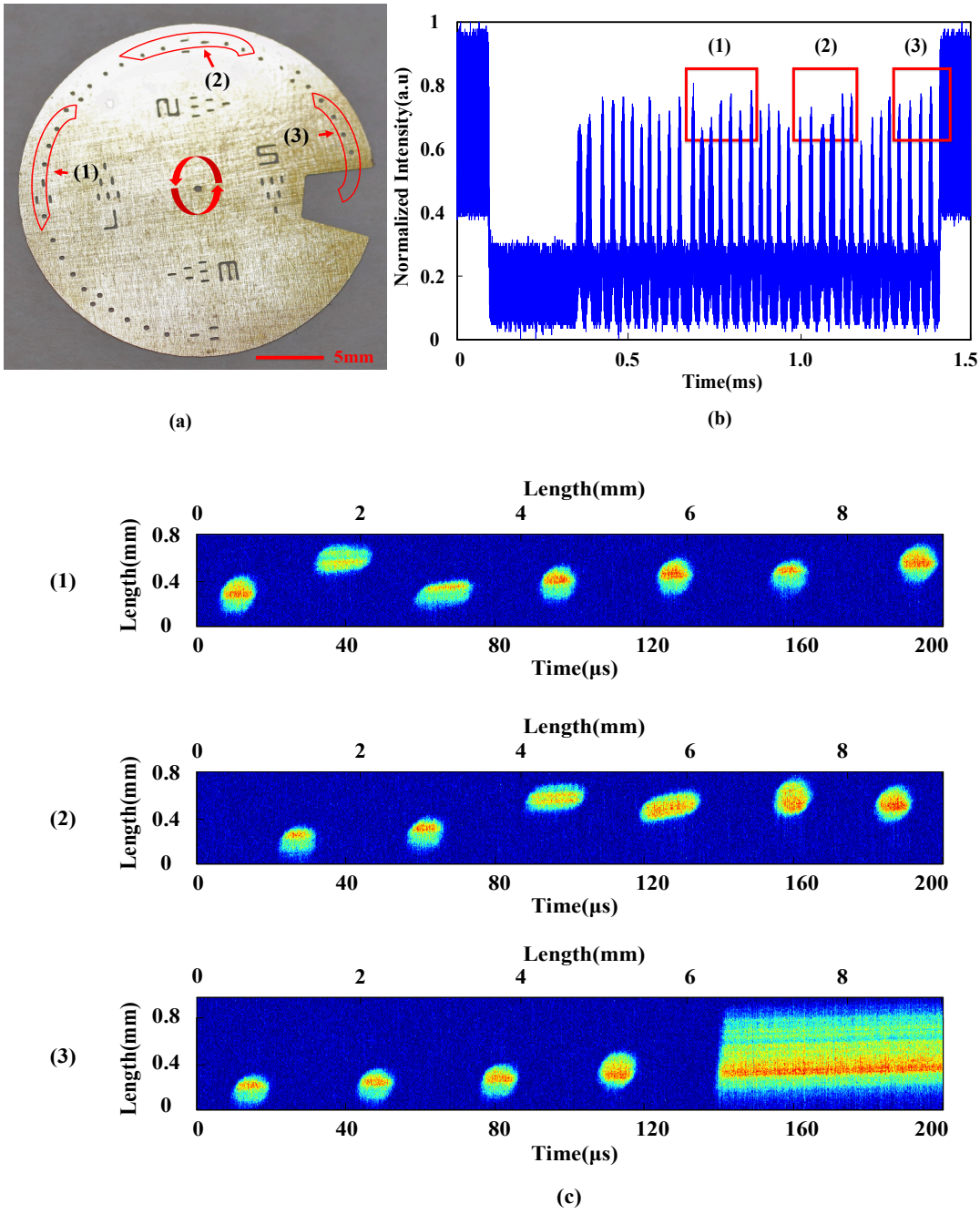

Figure 3.16 Imaging a fast moving object with PTS-based ultrafast SPI system using 45° TFG. (a) CCD image of the one-inch sample with etched features. (b) The captured temporal waveforms representing the features in the sample. Waveforms corresponding to three groups of features have been highlighted with red frames. (c) The reconstructed images of the three groups of selected features in the fast spinning object at a line speed of 46 m/s.

To demonstrate the ultrafast imaging capability of PTS-based ultrafast SPI system using 45° TFG, we implemented real-time imaging of a fast-moving object. The sample is a custom-designed one-inch round metal disk with some etched features,

as shown in Figure 3. 16 (a). The metal disk, which is placed in the object plane, is spinning at a speed of 40,000 rpm (rotation per minute), corresponding to a line speed of 46 m/s within the field-of-view range. The captured temporal waveform corresponding to a full rotation is plotted in Figure 3. 16 (b). Three groups of different features in the sample, as highlighted by red frames (1), (2) and (3), are represented by three groups of pulse bursts in red frames of Figure 3. 16 (b). Each pulse in the bursts performs a single-shot line scanning of the spinning sample. The reconstructed images of selected features in the fast spinning object are shown on Figure 3. 16 (c). Small circular holes, longer slots and a big gap have been clearly identified. Each of the images consists of 10,000 line scans. Each of line scans has a frame time of 20 ns and the whole image takes 200 μs. The actual field of view of each 2D image is 0.7 by 9.2 mm.

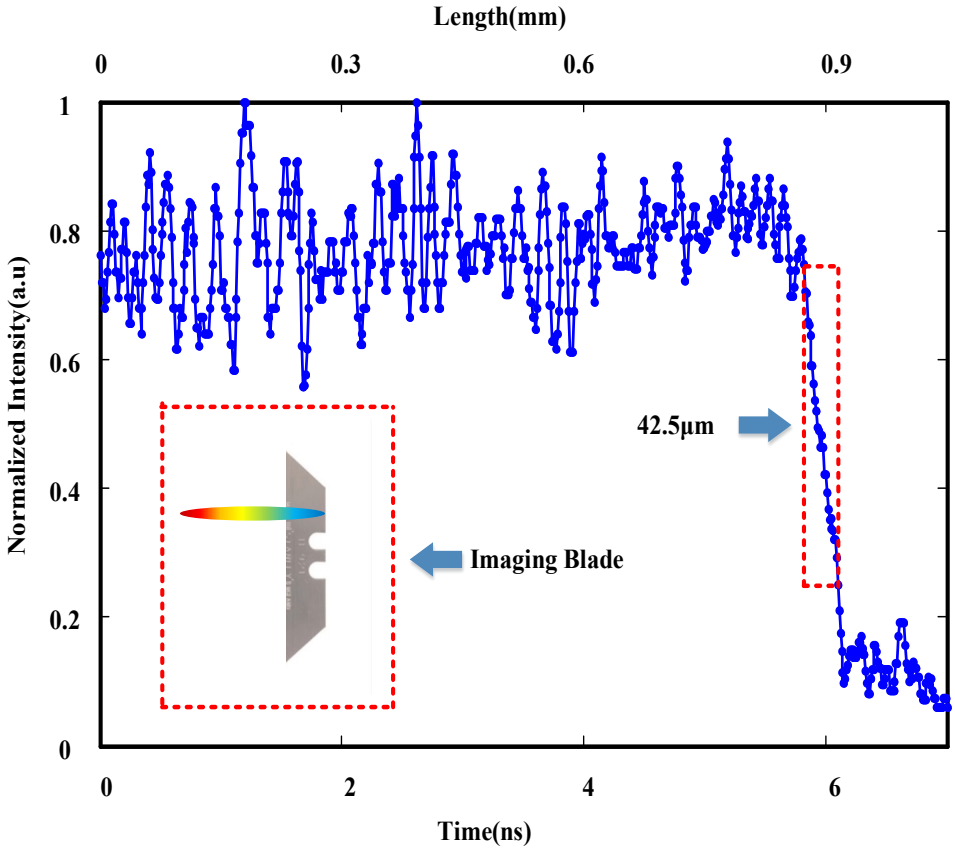

Figure 3.17 Measurement of lateral resolution of the proposed PTS-based ultrafast SPI system using 45° TFG based on point spread function by using a sharp blade.

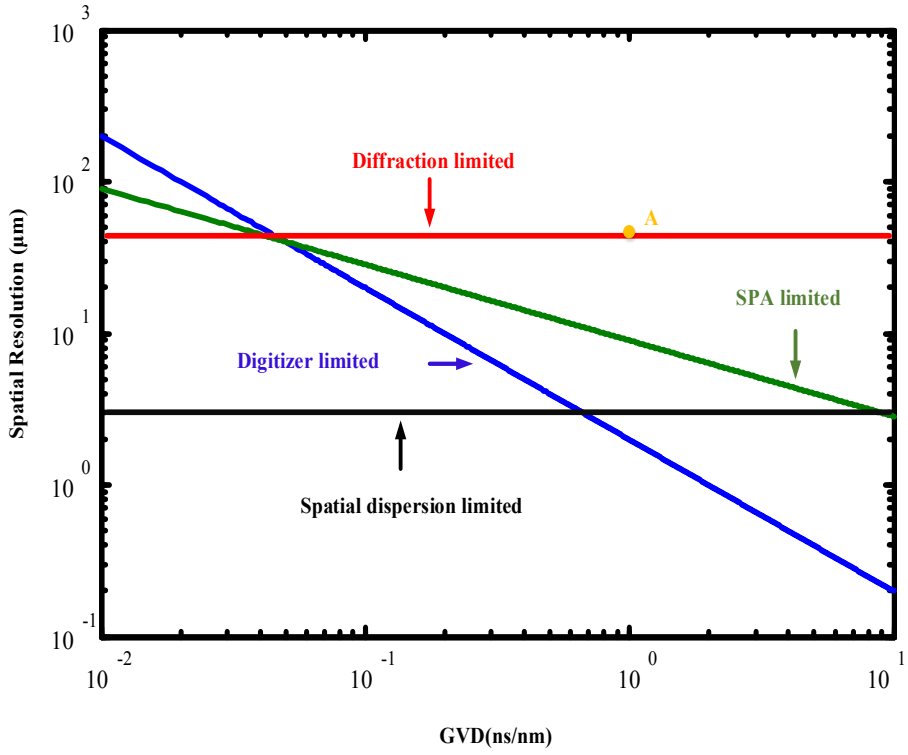

Figure 3.18 Spatial resolution analysis of our proposed PTS-based ultrafast SPI system using 45° TFG.

The spatial resolution of our proposed PTS-based ultrafast SPI system using 45° TFG is estimated based on point spread function measurement using a sharp edge blade. A lateral resolution of 42.5 μm is obtained, as shown in Figure 3. 17. The spatial resolution of our proposed system is further analyzed. Spatial resolution of our proposed imaging system is determined by various factors [14]: the spectral resolution of the spatial disperser (spatial dispersion limited spatial resolution), focusing power of the plano-convex lenses (diffraction limited spatial resolution), the spectral resolution imposed by dispersion-induced time stretch through stationary-phase-approximation (SPA) (SPA limited spatial resolution), and the temporal resolution of the digitizer (digitizer limited spatial resolution). Figure 3. 18 shows the calculated spatial resolution limited by different factors with respect to chromatic dispersion. The diffraction limited spatial resolution is calculated to be 41.7 μm according to the system parameters in our experiments. Owing to the extremely high grating groove density in the 45° TFG, the spatial dispersion limited resolution is as high as 3.2 μm. Considering that the GVD in our imaging system is 1.03 ns/nm, the measured spatial resolution is mapped into Figure 3. 18 as point A

(42.5 μm), which is very close to the diffraction limited spatial resolution of our imaging system.

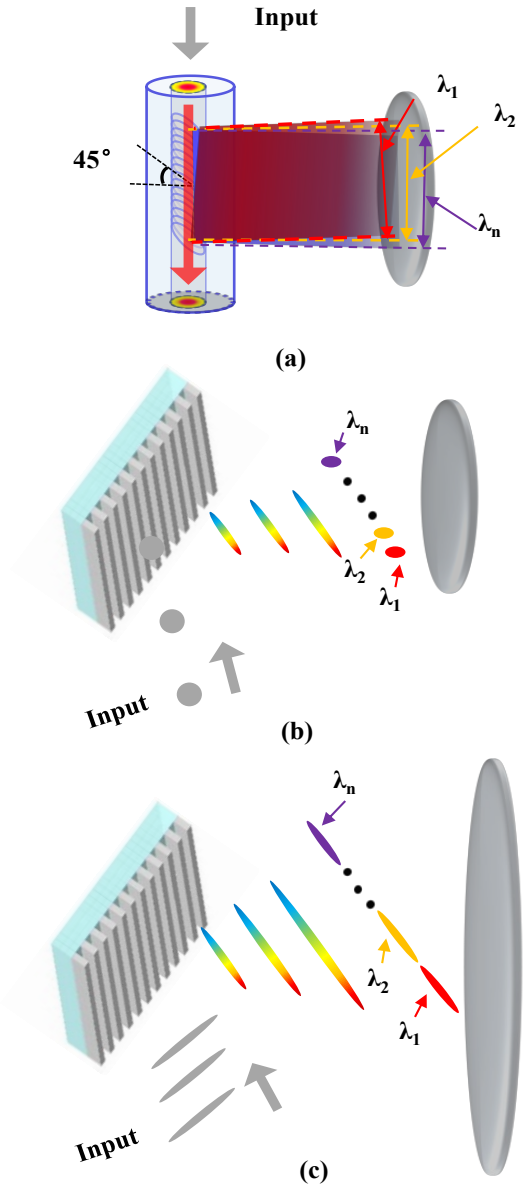

Figure 3.19 Principle of improved spatial resolution in PTS-based ultrafast SPI system using 45° TFG. (a) The proposed 45° TFG-based ultrafast imaging system offers improved imaging resolution. (b) Conventional STEAM systems use free space diffraction gratings. (c) In conventional STEAM systems, if the incident light has a large beam width, a very large focusing lens is needed to cover the whole diffracted illumination beam.

Improved spatial resolution is due to the fact that the 45° TFG has much smaller angular dispersion value than a normal free-space diffraction grating and the whole beam width of diffracted light is similar to that of initial illumination beam. Almost

full-aperture illumination is hence achieved for all wavelengths, as illustrated in Figure 3. 19 (a). In order to achieve microscopic imaging, spatial resolution of our system can be improved by using a high-quality objective lens. Capability of improving imaging resolution can be preserved. Note that exponential decay of diffracted intensity over TFG may slightly degrade the imaging resolution compared to an ideal Gaussian beam.

Different from our proposed TFG-based system, conventional STEAM systems suffer from sacrificed spatial resolution if a same imaging lens is used, which is usually poorer than the diffraction limit. This is because a free-space diffraction grating has large angular dispersion value resulted from its small groove spacing and the diffracted optical beams with different wavelengths are largely separated. Therefore, each individual illumination wavelength does not fulfil the full-aperture illumination condition required for high-resolution imaging, as illustrated in Figure 3. 19 (b). In addition, for a big initial illumination beam, a very large focusing lens is needed to cover the whole diffracted illumination beam, which is bulky and expensive and is shown in Figure 3. 19 (c).

To compare the imaging resolution, two time stretch imaging experiments are curried out using the 45° TFG and conventional free-space diffraction gratings (Thorlabs GR25–0616) respectively. To ensure a fair side-by-side comparison, the spectral bandwidth and beam of the illumination light out of the diffraction devices (45° TFG and free-space diffraction grating) remain identical in two systems and the same focusing lenses are used. Figure 3. 20 (b) to (e) shows the comparison results. The object is a thin metal plate with three etched slots, as shown in Figure 3. 20 (a). Upper left corner of the first slot is imaged using two systems. The reconstructed image using the 45° TFG-based imaging system and conventional STEAM system are shown in Figure 3. 20 (b) and (c), respectively. The spatial resolutions achieved by our proposed and the conventional systems are characterized as 27 and 45 μm, respectively, based on point spread function measurement, as shown in Figure 3. 20 (d) and (e). Therefore, superior performance of our proposed TFG-based approach in achieving higher imaging resolution has been evident.

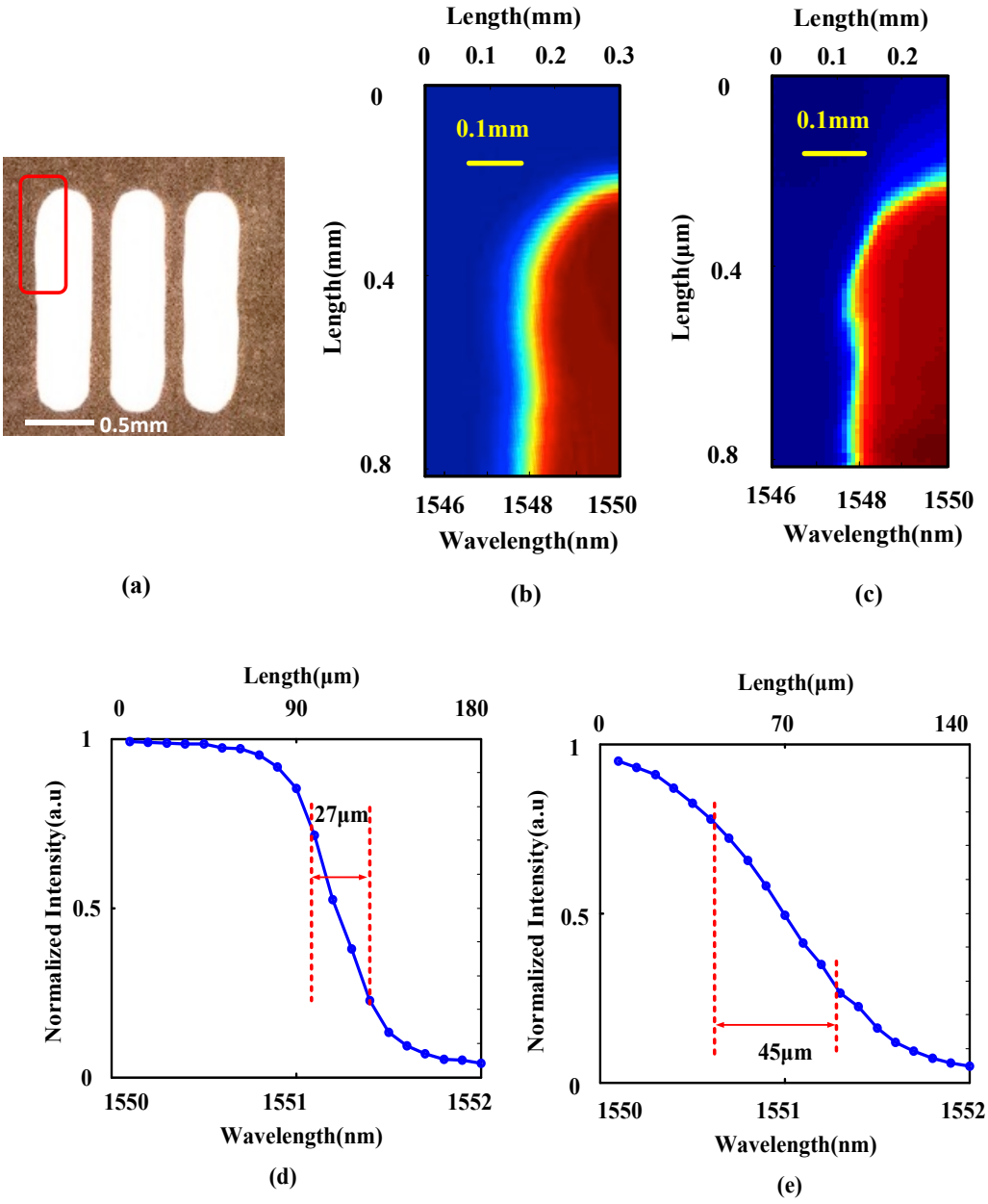

Figure 3.20 Comparison of spatial resolution in the proposed 45° TFG-based imaging system and conventional grating-based STEAM system. (a) CCD image of the sample used in comparison experiments (Imaging area is within the red frame). The reconstructed image using the 45° TFG-based imaging system (b) and conventional grating-based STEAM system (c). Point spread function measurement and measurement results using the 45° TFG-based imaging system (d, estimated to be 27 μm) and conventional grating-based STEAM system (e, estimated to be 45 μm).

The one-to-one time-to-wavelength mapping is experimentally calibrated based on the DCF employed in the proposed imaging system. A calibration system is built

using a Mach - Zehnder Interferometer (MZI) with an optical path difference (OPD) of 1.6 mm, which is shown in Figure 3. 21. The MZI is put to substitute the free-space optics starting from 45° TFG in Figure 3. 14. The output of MZI with fibre links is split into two channels using an optical fibre coupler. One channel is detected by an optical spectrum analyser, which shows the result of interferometric optical spectrum of time-stretched pulse. Another one is connected with PD and ultrafast oscilloscope. The combination of these two channels is used to detect the interference fringes of time-stretched pulse in time domain and spectrum domain. Via comparing the crest or trough of waves in time domain and spectrum domain, the one-to-one mapping between time and spectrum can be experimentally calibrated.

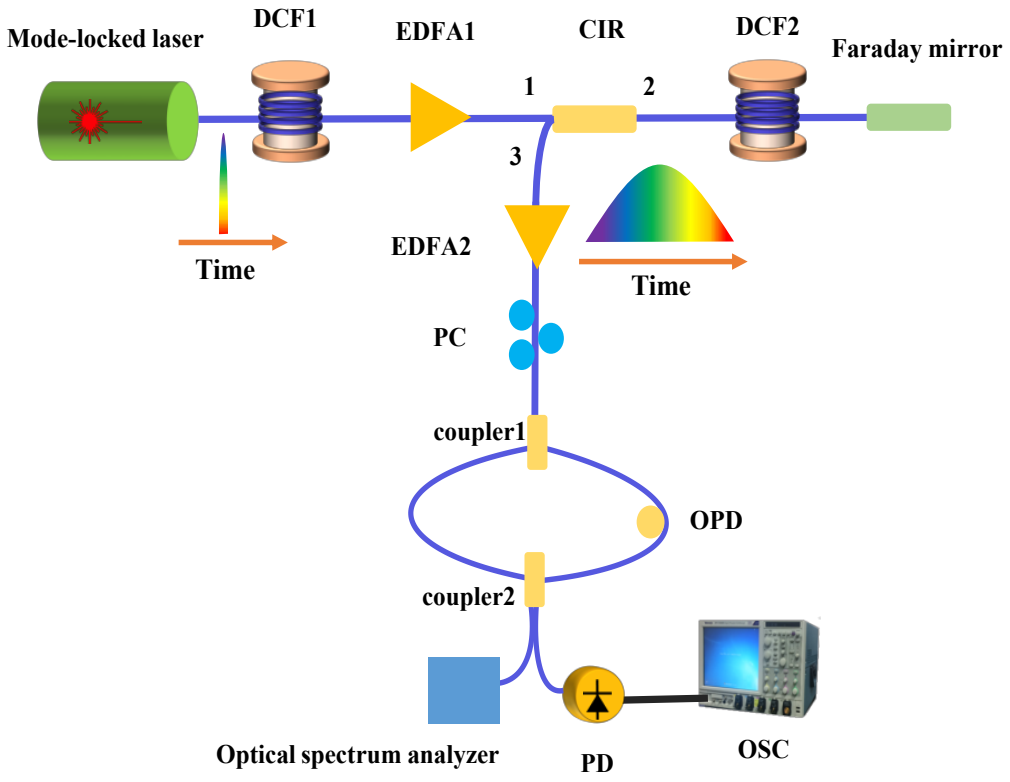

Figure 3.21 The schematic process of calibration using MZI and DCF.

Figure 3. 22 shows the experimentally calibrated result of time-to-spectrum one-to-one mapping relationship. The result shows a group velocity dispersion (GVD) of 1.03 ns/nm is obtained in our proposed system. The theoretical value of GVD provided by DCF is 1.04 ns/nm, which is quite close to the experimental result.

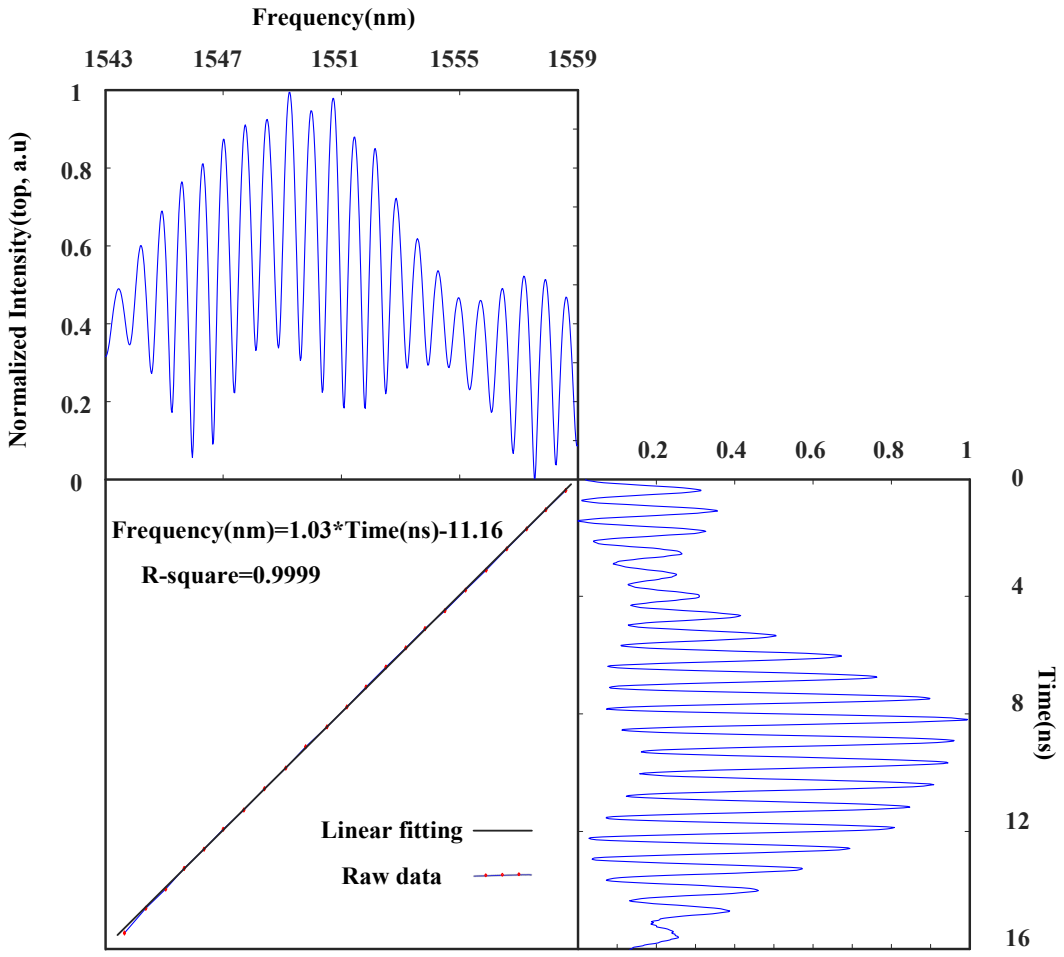

Figure 3.22 The calibration result of one-to-one time-to-wavelength mapping with a total GVD of 1.03 ns/nm.

The use of 45° TFG in PTS based ultrafast SPI system completely eliminate the need for bulky free-space diffraction gratings for spectral encoding and avoid complex and lossy light coupling between dispersive fibres and free-space components as well as improved the diffraction lateral resolution. This conceptually new design of all-fibre PTS based ultrafast SPI scheme using 45° TFG significantly reduces the volume of the imaging system, improves energy efficiency and system spatial resolution, and enhances system stability.

3.5. 45° TFG as a beam steering device in free-space optical wireless communication system

A new approach for broadband two dimensional beam steering for free-space indoor optical wireless communication system using a 45° TFG can be theoretically investigated and experimentally demonstrated. The 45° TFG is performed as the key element for nonmechanical passive beam steering by means of wavelength tuning, whose characteristics are previously analysed, has a wide range of applications.

3.5.1. 45° TFG as a beam steering device

There is increasing demand for higher data rate in indoor wireless communications. Conventional radio wireless communication suffers from limited transmission speed and ever-worse spectrum congestion [110]. Despite that the approaching 5G wireless techniques offer much higher data rate up to gigabits per second, the available RF bandwidth has nearly hit its limit and cannot fulfil the increasing demand of high data rate for indoor wireless transmission applications. On the other hand, optical wireless communication has attracted more and more interests recently as it provides a promising solution for high speed and wide bandwidth challenges in conventional radio wireless communications [111]. Optical wireless communication takes advantages of the huge bandwidth of optical carriers and mature transmission technology developed in long-haul optical fibre communication systems [112].

The principle of 45° TFG as a wavelength-controlled passive optical beam steering device is shown in Figure 3. 23. Optical beams with different wavelengths are diffracted into different spatial positions by the diffraction device, namely, mechanical-free beam steering is achieved via wavelength tuning. The wavelength-dependent angle depends on the nature of 45° TFG and it's investigated in chapter 3.2. In order to make the distance between transmitter and receivers flexible, a lens

is employed to separate the beams of different wavelengths. Based on the nature of highly efficient, low-cost, polarization-sensitive, compact and fibre-compatible 45° TFG, an indoor free-space optical wireless communication system is presented in the next part.

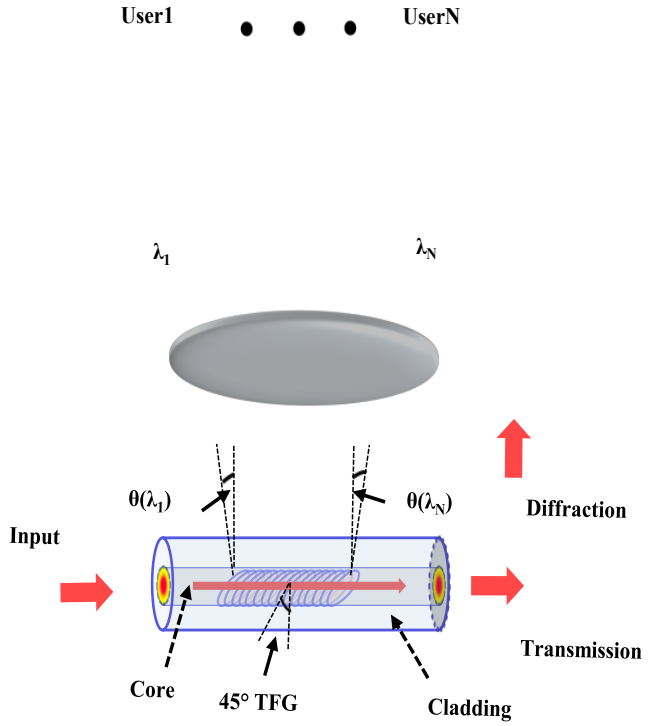

Figure 3.23 The principle of wavelength-tunning-based laser beam steering using the TFG.

3.5.2. An indoor free-space optical wireless communication system

As preliminary comprehensive analysis, to verify the utility of the 45° TFG in wavelength-controlled optical beam steering in optical wireless communication, a proof-of-concept experiment based on the setup shown in Figure 3. 24 is performed. A data stream to be transmitted is first generated using an AWG. After being amplified by a radio frequency amplifier (RFA), the data stream modulates the continuous-wave optical carrier from a WSL source at a MZM, which is biased at quadrature point to minimize modulation nonlinearity. An optical fibre polarization controller (PC) is used to ensure that the incident light into the 45°

TFG is s-polarized, which guarantees the maximum diffraction efficiency as high as 93% over a broad bandwidth from 1530 to 1570 nm. The 45° TFG diffracts light of different wavelengths into different directions thanks to its inherent angular dispersion. Optical beam steering is obtained by tuning the wavelength of the optical carrier using a WSL source.

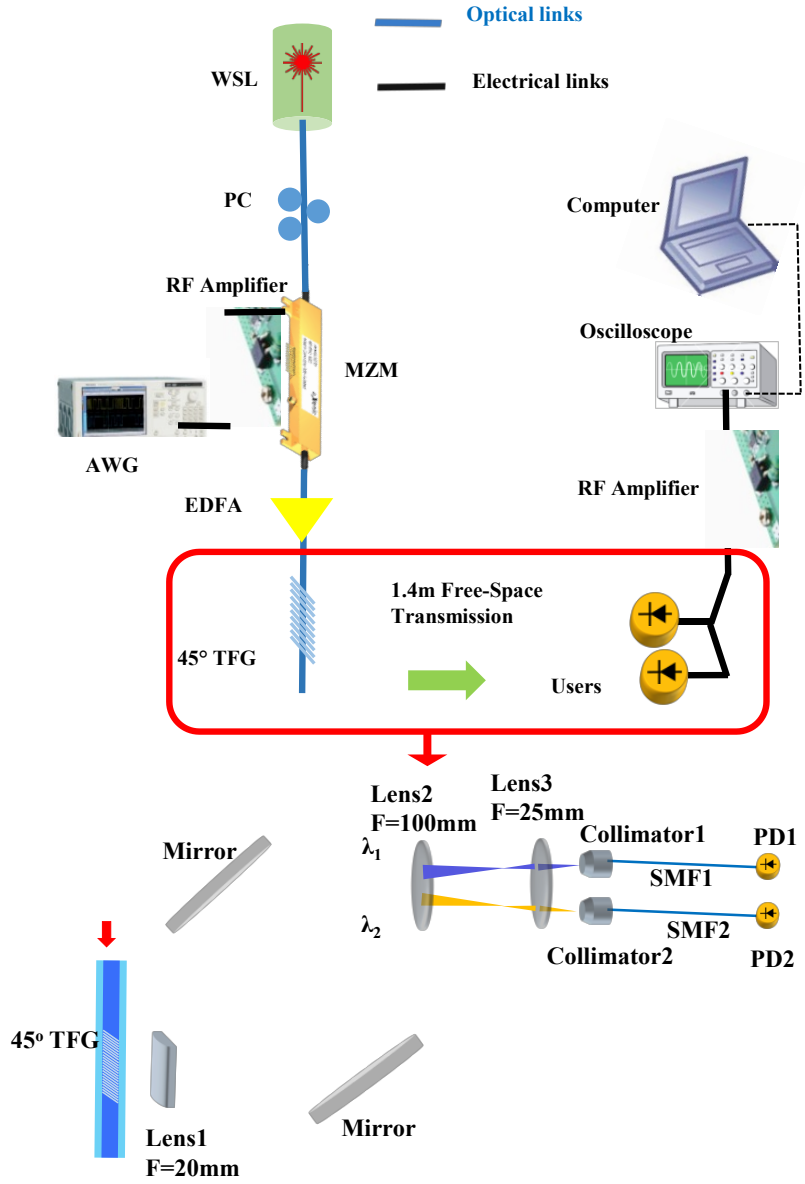

Figure 3.24 Schematic of passive beam steering system for free-space indoor optical wireless communication using a 45° TFG.

The diffracted light beam has a horizontal beam width as same as the length of the 45° TFG. In all the following experiments, only the first 8 mm length of the TFG is used as it provides dominate light diffraction and produces good received optical

power considering the trade-off between tolerance to optical alignment and signal-to-noise ratio.

A 1.4 m free-space optical link is then implemented for beam steering data transmission. Here three optical carrier wavelengths of 1530, 1540 and 1550 nm were selected to serve three remote users. After 1.4 m indoor free-space transmission, the laser beam is received by each of the remote users. In order to obtain high data rate, a single mode fibre (SMF) coupled high-speed PD with a receiving bandwidth of 45 GHz is used at each user site. Light reception is realized using a telescope set for beam shrinking and a SMF collimator (NA=0.49) at the receiver end for light coupling into the PD. The measured optical link propagation loss ranges from 6.8 dB to 10.4 dB for different channels.

In our experimental setup, each wavelength has a quite high spectral bandwidth, however, due to the limitation of AWG and its compatible software, which can only support with a spectral bandwidth of 2.4 GHz, spectral-efficient orthogonal frequency-division multiplexing (OFDM) modulation format thus is needed and is utilized to have a better usage of the optical carrier bandwidth for data transmission. An OFDM 16-quadrature amplitude modulation (16-QAM) encoded data stream is created offline in MATLAB. The complex OFDM symbols created in MATLAB are used to generate a 2.4 GHz bandwidth signal through an AWG (Tektronix 7122C) at an intermediate frequency (IF) of 2 GHz. The AWG operates based on 10-bit digital-to-analog conversion (DAC) with a sampling rate of 12GS/s. Data blocks contains 16-QAM modulated data offers an aggregate data rate of 9.6 Gb/s.

The constellation of received 16-QAM OFDM signal for one remote user with allocated optical wavelength of 1550 nm is shown in Figure 3. 25 (a). Here the received optical power is -2 dBm. The error vector magnitude (EVM) is estimated as 9.6%. Optical beam steering using the 45° TFG for multiple users is demonstrated with the help of a fixed mirror set. Three optical wavelengths of 1530, 1540 and 1550 nm have been selected to serve the three users. EVM performance for all the three channels have been measured with respect to the received optical power with the results shown in Figure 3. 25 (b). The EVM limit for 16 QAM is 12.5%. Using a bandwidth of 2.4 GHz, our system demonstrates a

data rate of 9.6 Gb/s per beam, which is only limited by the sampling speed of the AWG used in the experiment.

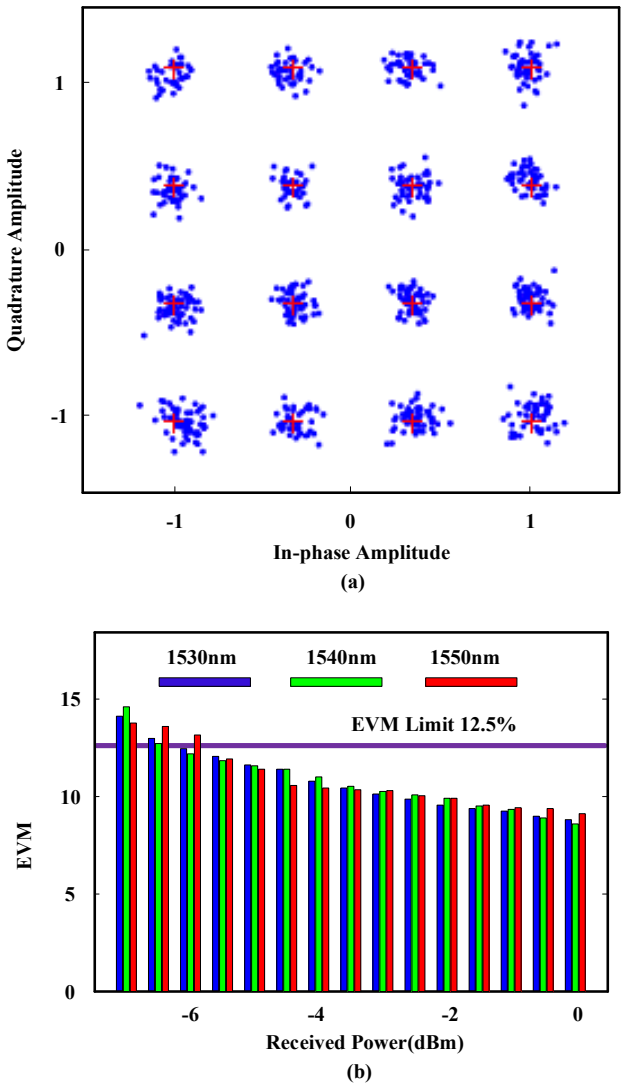

Figure 3.25 Experimental results for optical wireless transmission. (a) Constellation of OFDM 16-QAM signal received by one user with allocated optical wavelength of 1550nm. The received power is - 2 dBm, and the EVM is estimated as 9.6%. (b) EVM performance of all three channels (16-QAM) with optical wavelengths of 1530, 1540, and 1550 nm with received optical power ranging from -7 to 0 dBm.

A novel optical beam steering method using a 45° TFG as a highly efficient in-fibre diffraction device is proposed and experimentally demonstrated for the first time. However, the feature of bidirectional of 45° TFG is not utilized, that is to say, the 45° TFG is not only served as an in-fibre diffraction device, but also as an acceptor

of recoupled optical signal. Thus, a full-duplex bidirectional free-space optical wireless communication using 45° TFG is presented next part.

3.5.3. Full duplex free-space optical wireless communication system

Based on the previous research of 45° TFG as an in-fibre beam steering device in indoor free-space optical communication system, full-duplex bidirectional indoor free-space optical communication system using 45° TFG is investigated and performed, in this case, the 45° TFG functions as an beam steered light transmission and reception device at the same time via wavelength tuning. The in-fibre diffraction device has the advantages of low cost, high diffraction efficiency, and low uplink coupling loss from free-space to existing optical fibre links, making it a promising optical beam steering candidate in full-duplex indoor optical wireless communication system.

The schematic of full duplex bidirectional indoor free-space optical communication system using a 45° TFG is shown in Figure 3. 26. A RF signal with a bandwidth of 2.4 GHz on a 2GHz electrical carrier from radio frequency signal generator (RFSG, Tektronix 7122C) with a sampling rate of 12 GS/s. The signal with encoded data stream are using OFDM 16/32-QAM and a bit rate of 9.6 Gb/s or 12 Gb/s is generated with further magnified by a RFA. Different wavelengths of optical light beam from the tunable laser (TL) is modulated by the signal when it passes through the MZM. In the access point two polarization controllers are utilized, one is used to ensure the minimum insert loss of MZM, another one is employed to guarantee the maximum efficiency of the 45° TFG with all the *s*-polarized light will be diffracted into open space for free-space optical communication usage. Owing to the angular dispersion of the 45° TFG, different wavelengths of the optical light beam from TL will be diffracted into different spatial position and beam steering is achieved by optical carrier wavelength tuning.

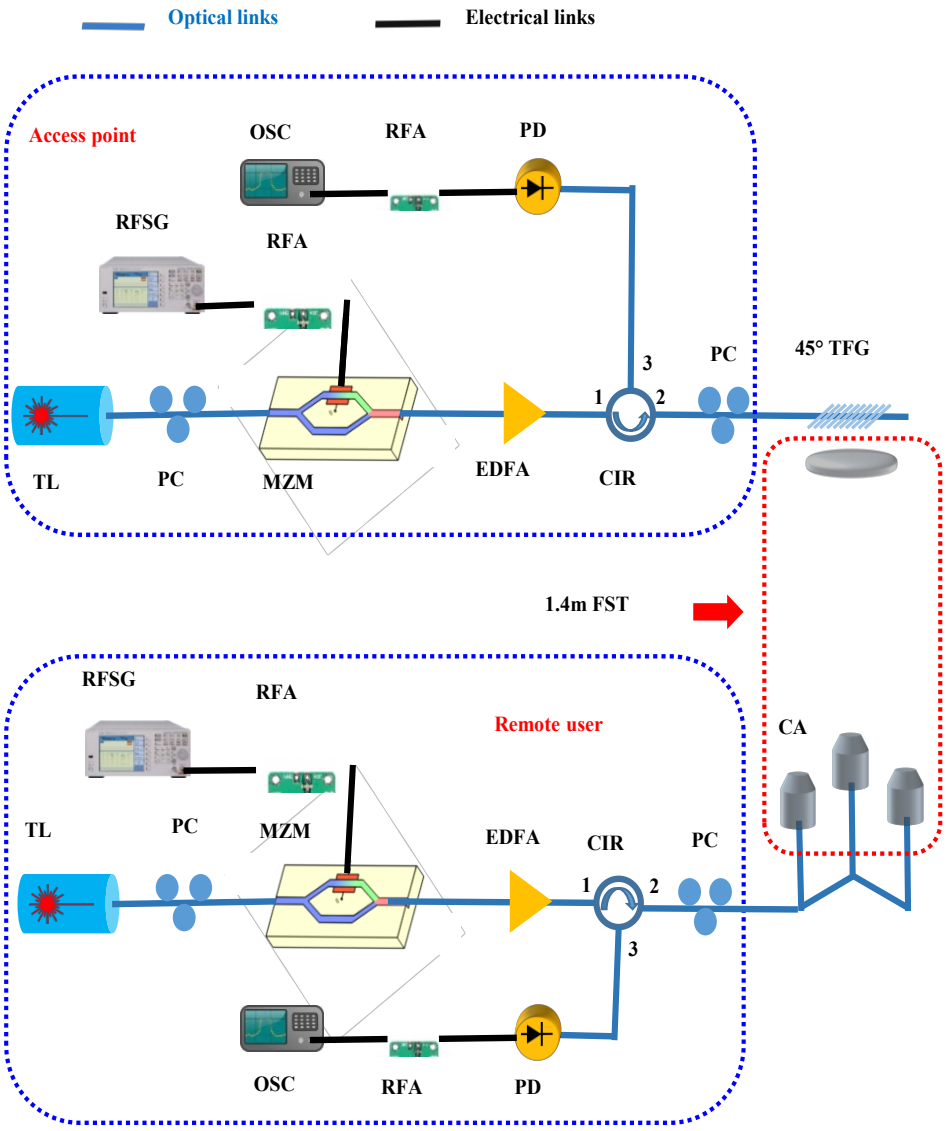

Figure 3.26 Schematic of full duplex bidirectional indoor free-space optical communication system using a 45° TFG.

A lens set is put after the 45° TFG to collimate and shrink the beam size during the 1.4 m indoor free-space transmission (FST) and a collimator (NA 0.49) matrix (CM) is utilized to receive the free-space optical light beam. The access point and the remote user is connected by the circulator to realize the duplex bidirectional free-space optical communication. Light received by CM will be converted to electrical signal by PD with a bandwidth of 3 GHz followed by a second RFA and sampled by the 100 GS/s oscilloscope (Tektronix DPO72304DX). Finally the data

received by oscilloscope will be shifted to computer for off-line data processing using MATLAB.

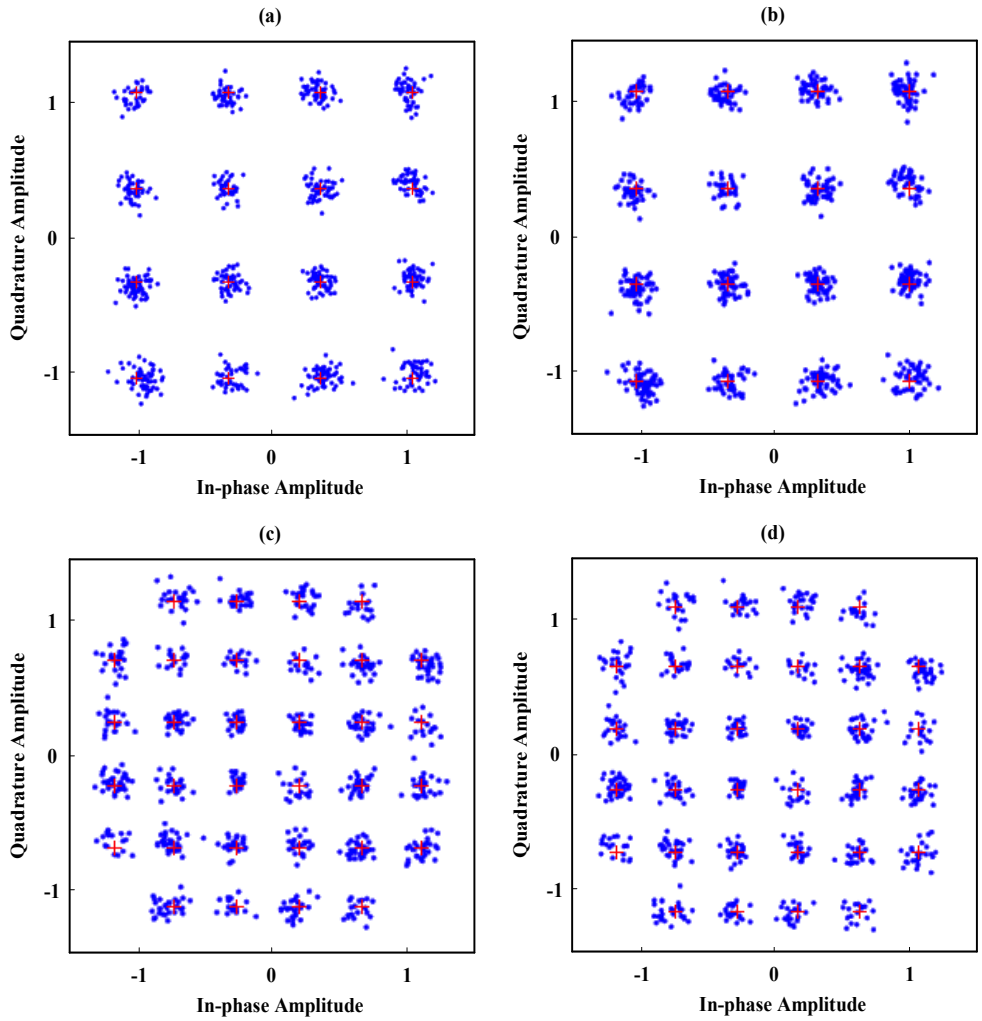

Figure 3.27 Constellation of received 16-QAM OFDM signal for (a) uplink channel with 10.1% EVM and (b) downlink channel with 9.8% EVM with optical wavelength of 1550 nm and a received optical power of -2 dBm; Constellation of received 32-QAM OFDM signal for (c) uplink channel with 10.7% EVM and (d) downlink channel with 10.3% EVM with optical wavelength of 1550 nm and a received optical power of -1 dBm.

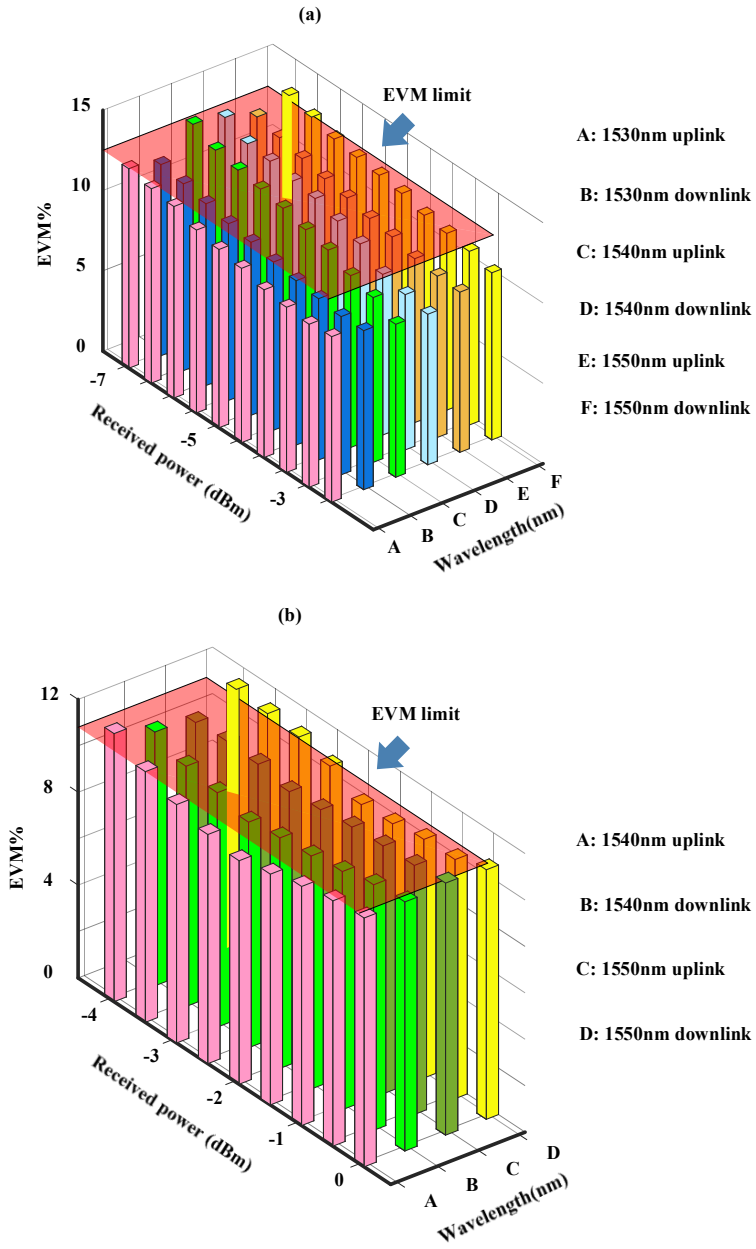

Figure 3.28 (a) The EVM performance of 16-QAM with duplex bidirectional free-space optical communication at the wavelength of 1530 nm, 1540 nm, 1550 nm with received optical power from -7 to -2.5 dBm; (b) The EVM performance of 32-QAM with duplex bidirectional free-space optical communication at the wavelength of 1540 nm, 1550 nm with received optical power from -4 to 0 dBm.

The result of the presented duplex bidirectional communication system is shown in Figure 3. 27 and Figure 3. 28. The constellation of 16-QAM OFDM diagraph is shown in Figure 3. 27 (a) and (b), with a 10.1 % and 9.8% error vector magnitude (EVM) for uplink channel and downlink channel respectively, with -2dBm received

optical power in 1550nm; while constellation of 32-QAM OFDM diagraph is shown in Figure 3. 27 (c) and (d), with a 10.7 % and 9.3% EVM for uplink channel and downlink channel respectively, with -1dBm received optical power at 1550nm. The EVM limit for 16-QAM and 32-QAM is 12.5% and 10.8 % respectively and the bit rate for 16-QAM and 32-QAM is 9.6 Gbit/s and 12 Gbit/s, respectively. Figure 3. 28 (a) and (b) shows the EVM result of 16-QAM and 32-QAM with their received optical power, respectively. Figure 3. 28 (a) gives the EVM performance of uplink channel and downlink channel at 1530nm, 1540nm and 1550nm using 16-QAM with received optical power from -7 to -2.5 dBm and Figure 3. 28 (b) gives the EVM performance of uplink channel and downlink channel at 1540nm and 1550nm using 32-QAM with received optical power from -4 to 0 dBm.

3.6 Summary

In this chapter, the main application of imaging with 45° TFG is theoretically investigated and experimentally demonstrated and another of wireless communication application with 45° TFG for beam steering is experimentally proposed.

Firstly, we proposed and experimentally demonstrated a new highly efficient, fibre-compatible, and cost-effective spectrally encoded imaging system based on a 45° TFG. As an in-fibre diffraction element, the 45° TFG replaces the bulky and lossy free-space diffraction gratings in conventional imaging systems. A 24-mm long 45° TFG was fabricated with its angular dispersion measured to be 0.054°/nm within a wide spectral range of 40nm (from 1530 to 1570 nm) and lateral diffraction efficiency measured to be as high as 93.5%. As a proof-of-concept demonstration, 1D line scan imaging of a custom-designed three-slot target and “KENT” sample were performed using the 45° TFG-based SEI system. This design significantly reduces the volume, complexity and optical insertion loss and improves the efficiency and stability of the conventional imaging systems. The developed technique holds great promise in various applications where portable and low-cost imaging systems are needed. In addition, as the 45° TFG-based diffraction element is inherently compatible with optical fibres that provide chromatic dispersion, it is

particular attractive in ultrafast real-time SEI system based on dispersion-induced time-stretch dispersive Fourier transform, which will significantly increase the temporal resolution for ultrafast and high-throughput measurements.

Secondly, we proposed and experimentally demonstrated the first use of a 45° TFG in PTS based ultrafast SPI system enabling highly efficient and diffraction-limited ultrafast time stretch imaging. The 45° TFG is presented as an in-fibre diffraction device to replace bulky and lossy free-space diffraction gratings in conventional STEAM systems. As the 45° TFG is inherently compatible with optical fibres that provide chromatic dispersion for time stretching, no coupling loss between free-space and fibre optics will occur. This new proposal simplifies the conventional STEAM system, reduces system volume and cost, and promotes higher energy-efficiency, and better stability. A 24-mm long 45° TFG was fabricated with an angle dispersion of 0.054°/nm and an enhanced diffraction efficiency up to 97%. Utility of the 45° TFG in ultrafast time stretch imaging has been verified by proof-of-concept demonstrations, where a fast moving customer designed one-inch sample with holes and short slots in its edge at 46 m/s was imaged at frame rate of 50 million frames per second with a large field of view of 0.7 mm. Diffraction-limited spatial resolution has been achieved due to the fact that a long 45° TFG produces much wider instantaneous illumination beam size. A side-by-side comparison between the proposed in-fibre approach and the conventional free-space diffraction grating based STEAM systems have been carried out to evidence the superior performance of our approach and the lateral spatial resolution is 27μm and 45μm separately. This conceptually new PTS based ultrafast SPI scheme opens the way towards cost-effective, stable, compact and high-resolution ultrafast imaging systems for image-based high-throughput detection and measurement.

Finally, based on previous analysis, the 45° TFG is performed as wavelength-dependent passive beam steering device in free-space wireless optical communication systems. In addition, the proposed 45° TFG-based beam steering solution provides inherent compatibility with existing fibre links, which is particularly attractive in achieving seamless interface with FTTH access networks. The considerable coupling loss between fibres and free-space or waveguide devices in conventional systems is also completely eliminated. The proposed all-fibre

optical beam steering technique is successfully verified by proof-of-concept experiments, in which optical wireless transmission over 1.4 m serving three users with data rate of 9.6 Gbps per beam has been demonstrated using 2.4 GHz bandwidth OFDM signals. Also, for the first time we have presented and experimentally demonstrated a full-duplex bidirectional indoor free-space optical communication system using a 45° TFG as wavelength controlled passive beam steering device for light diffraction and reception of back recoupled light. A RF signal with a bandwidth of 2.4 GHz at an electrical spectral carrier of 2GHz from RFSG utilizing OFDM 16/32-QAM to perform the experiment with a bit rate of 9.6 Gbit/s or 12 Gbit/s. Thanks to its unique features of low-cost, compactness, inherent fibre compatibility and low insertion loss, the presented 45° TFG based laser beam steering holds great promise in full duplex indoor optical wireless transmission in future high data-rate home area networks.

CHAPTER 4: DATA COMPRESSION IN ULTRAFAST SINGLE-PIXEL IMAGING BASED ON COMPRESSED SENSING

4.1. Introduction

In this chapter, CS single-pixel imaging (SPI) system based on STEAM structure, and PTS and CS based OCT system are presented. SPI systems [8–12], which overcome the bottleneck of direct sight of the object, draw extensive attention due to the advantages of enabling high quality images acquiring with a single point detector.

To enhance the speed of the SPI-based systems, several of methods are proposed, one of the most popular methods is using PTS technique [16], also named DFT [13,113], and frequency-to-time mapping, which has been previously investigated and implemented in OCT [92], ultrafast optical imaging systems [23,98,114], ultrafast waveform measurement [115], and analog-to-digital technology [116]. PTS can map the broadband optical spectrum of an ultrashort optical pulse into temporal waveform via the employment of GVD as introduced in chapter 2. Hence, the temporal resolution of the optical system can be greatly enhanced and ultrafast optical measurement system is made possible via using a high-speed single-pixel PD.

However, the utilization of PTS leads to big data problem, that hundreds of gigabits even terabits of data needs to be processed in one second. Thus, big data compression technique is desired. CS is a promising technique for big data compression and it is based on the theory that the sparse information in a transformation domain can be recovered from a reduced number of measurements, which is introduced in chapter 2, conquers the traditional Nyquist-Shannon sampling theorem [88,89]. Hence, it got pervasive attention in RF signal detection [117,118], OCT [92–94] and CS-based imaging [23,92].

To achieve data compression using CS technique, PRBS is widely employed to generate random serials [92], which have the drawback of high cost and narrow bandwidth owing to the employment of expensive AWG. Also, the speed of CS imaging is limited by multiple measurements to obtain one frame. Several of methods are employed to eliminate the usage of expensive PRBS that generated by AWG, for example, a special TiO2-coated fibre tip, which could generate wavelength-dependent optical random speckle patterns to perform CS imaging, is introduced in [10]. However, the imaging speed of this methods is limited to the tunable laser speed and its iteration. Also, another high-speed low-cost random sequential CS method is presented using MMF [119], which has potential applications in imaging and signal detection.

In the following part, a STEAM structure based CS SPI system is introduced using a spatial mask as the passive optical random generator, and a CS and PTS based OCT system as a joint work is presented.

4.2. Compressed sensing in spatial domain

As introduced in chapter 2, STEAM based on spectrum-encoded time-stretch (SETS) structure has enabled unprecedented ultrafast imaging speed of tens of MHz or even GHz [16] and it has been extensively applied in various real-time ultrafast dynamic phenomena, such as ultrafast laser scanning [6], flowing particle screening [120], and ultrafast optical imaging [11,12,21]. STEAM consists of two steps: one-to-one spectrum-to-space mapping (spectrum encode procession) and one-to-one spectrum-to-time mapping (time-stretch procession). And an ultrafast single-pixel detector, i.e. PD, could be employed for ultrafast optical dynamics measurement thanks to the unique one-to-one mapping of space-spectrum-time.

However, the employment of time-stretch procession requires expensive ultrafast PDs and oscilloscopes, which increases the cost of the optical system drastically and enhances the high volume of data that needs to be processed. One solution is using nonlinear one-to-one mapping between time and spectrum, i.e. anamorphic stretched transform or wrapped time stretch [104,121], more imaging information

could be detected with better time resolution. One of the other commonly used solutions is the utilization of CS method [23,92,98], which reduces the high volume of data that needs to be processed, has the benefits of low-cost via using low-bandwidth PDs and oscilloscopes. For example, in our CS imaging system setup, a low-bandwidth of 50MHz PD is used to replace the traditional high-bandwidth PD over 10GHz via using CS method. In order to perform CSI, PRBS that generate random patterns are demanded for the CS procession [92,98]. Conventionally, the PRBS sequences are generated by AWGs, which could achieve a speed of 10GHz or even more. However, to obtain such speed an expensive large-bandwidth modulator is needed, which increases the cost and complexity of the system.

To tackle this issue, a passive all-optical random pattern generator, i.e. spatial mask, is employed in the system (in our experiment the passive all-optical random pattern generator is based on SLM, but it is not limited to SLM), which eliminates the usage of AWGs and expensive large-bandwidth modulators, with the benefit of all-optical mixing in CS and low-cost is proposed. This proposal has the merits of low-cost and high-speed as no electrical devices are involved in the process. This method has wide applications in dynamic phenomena where low-cost and high-speed system is required.

4.2.1. Experimental setup of STEAM based CS imaging system

The schematic of the proposed CSI system is shown in Figure 4. 1. A pulsed MLL (Calmar Mendocino FP laser) with a repetition rate of 50 MHz is employed as the laser source, which has an average optical power of 15 mW and the pulses produced by MLL have a FWHM of 800 fs. In order to achieve linear one-to-one mapping between spectrum and time, ultrashort optical pulses from MLL are stretched in time domain using DCFs, with a total dispersion of 0.65 ns/nm. Besides, two EDFAs are used for optical amplification after the pulses time-stretch to achieve higher SNR. The amplified and time-stretched optical pulses are scattered onto a diffraction grating (1200 lines/mm) via a collimator (Thorlabs, F240APC-1550) under polarization control using a PC. A plano-convex lens with a

focusing length of 150mm (Thorlabs, LA1433-C) is used for collimating the beam. The optical pulses of the beam passes through a polarization beam splitter (PBS, Thorlabs, PBSW-1550) and a half-wave plate (HWP, Thorlabs, WPH10ME-1550), then reaches the sample (1951 USAF resolution target) and spatial mask, where the optical mixing of imaging and random patterns in spatial domain is happened. The HWP has an angle of 22.5° to match the polarization coupling for the intensity modulation of reflective spatial mask. The optical pulses carrying the information of imaging and random patterns, modulated and reflected by spatial mask, returned to the original collimator with same free-space optical way. The information-carried optical pulses in time-serial are detected by a single-pixel PD with a bandwidth of 2GHz via a circulator. An oscilloscope with a real-time sampling rating of 12.5GS/s is employed to digitize the captured information followed by information processing in computer using Matlab programming.

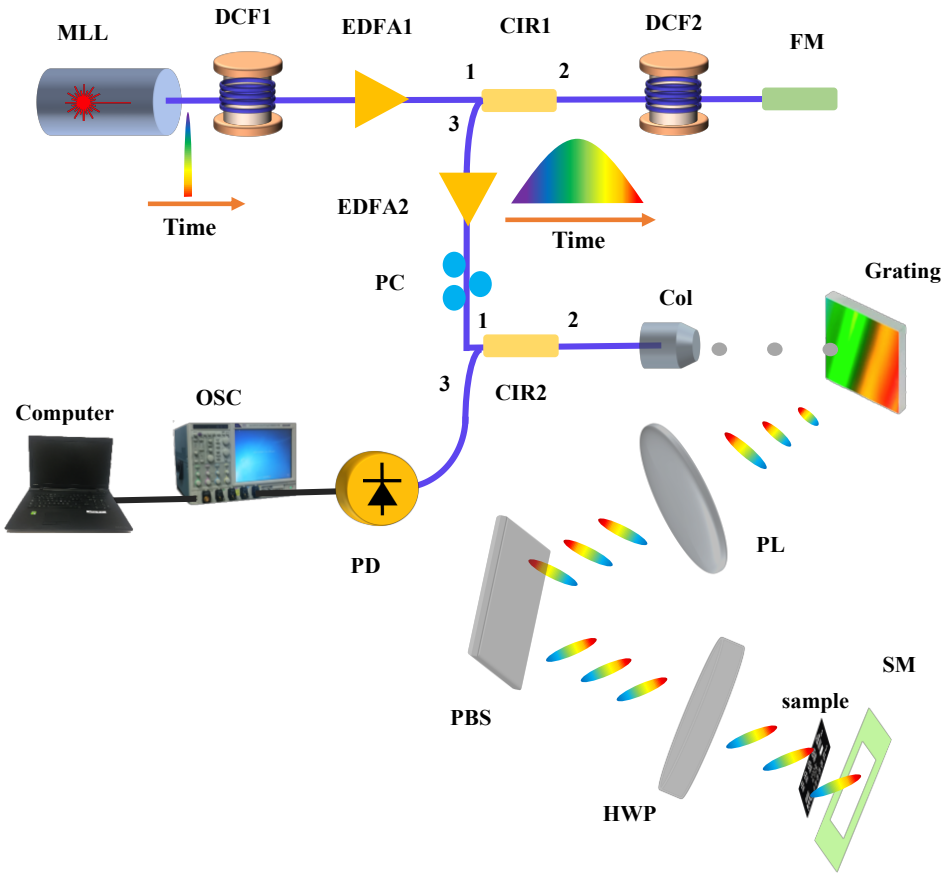

Figure 4.1 Schematic of the proposed CSI system based on SETS structure.

Note in this demonstration the data compressing of CS method is implemented in digital domain, that is to say, the pulse compression for every 20 ns is digitally-added in Matlab instead of using SMF to compress the time-stretched optical pulse, which is limited by the existing devices. However, theoretically in the traditional CSI system matched length of SMF should be used to compensate the DCF and a low-cost low-speed 50MHz PD could be applied, thus the cost and data volume of system can be reduced.

4.2.2. Results and discussions

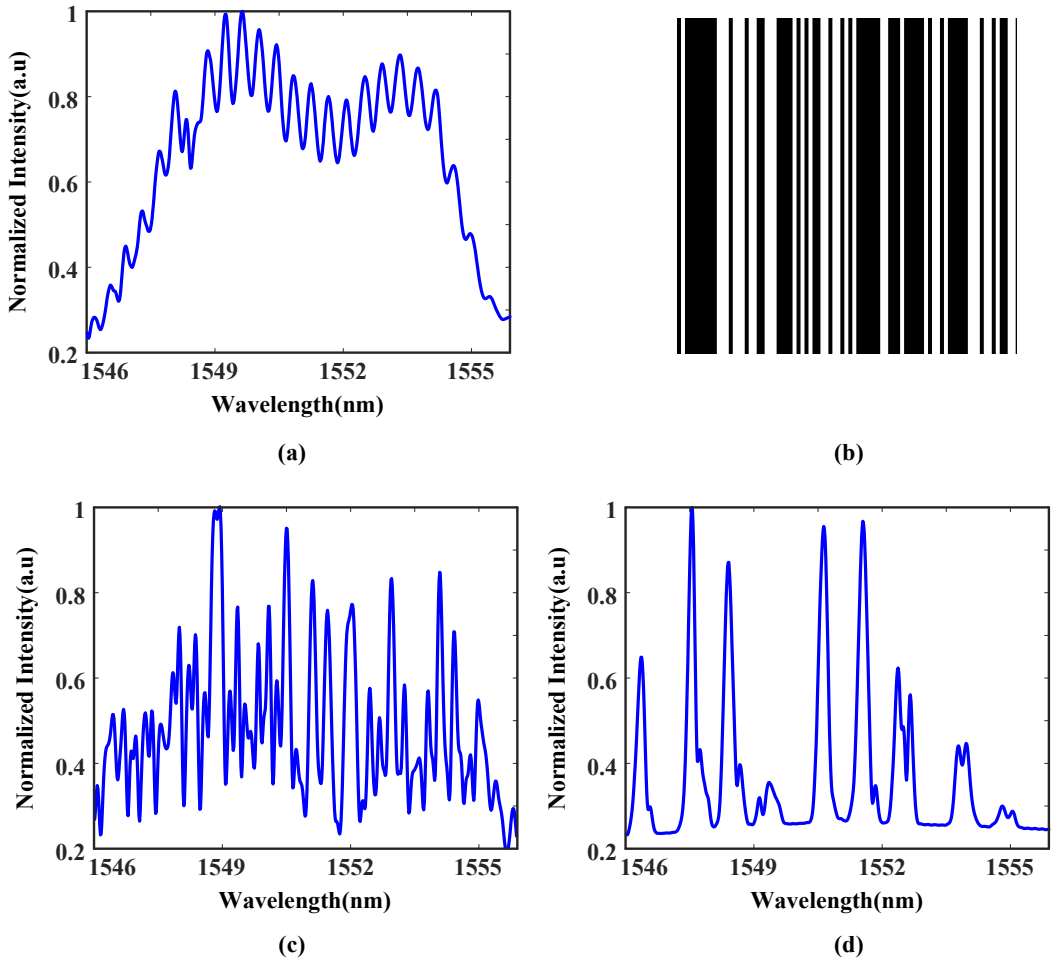

Figure 4.2 (a) Input of time-stretched pulse in spectral domain. (b) One random pattern from spatial mask. (c) Result of all-optical mixing of (a) and (b) in spectral domain. (d) Result of optical mixing of resolution target and (c) in spectral domain.

The input of time-stretched pulse in spectral domain is shown in Figure 4. 2(a), where the incident time-stretched pulse is sent to the collimator. The spectrum range is from 1546 nm to 1556 nm. Figure 4. 2(b) shows one random pattern from spatial mask that used to modulate the optical pulse (a) in spatial domain. The result of spatially all-optical mixing of Figure 4. 2(a) and (b) is illustrated in Figure 4. 2(c) in spectral domain. Figure 4. 2(d) shows the result of spatially optical mixing of resolution target and (c) in spectral domain.

As our system has the unique feature of one-to-one mapping between spectrum and time. Similarly, the input of time-stretched pulse in time domain is shown in Figure 4. 3(a), for a sampling rate of 12.5 GS/s, there have 81 points which last 6.5 ns. Another optical random pattern from spatial mask that used to modulate the optical pulse spatially is shown in Figure 4. 3(b). Figure 4. 3(c) shows the spatially all-optical mixing of Figure 4. 3 (a) and (b) in time domain. Figure 4. 3(d) is the result of spatially optical mixing of resolution target and (c) in time domain.

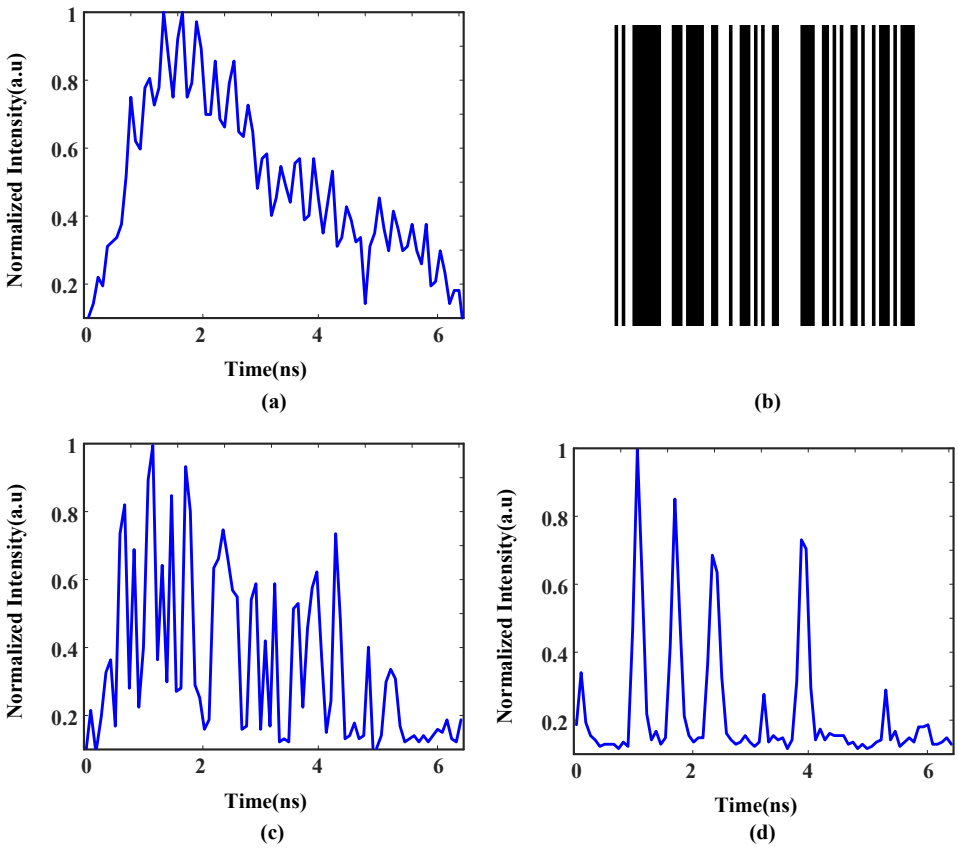

Figure 4.3 (a) Input of time-stretched pulse in time domain. (b) One random pattern from spatial mask. (c) Result of all-optical mixing of (a) and (b) in time domain. (d) Result of optical mixing of resolution target and (c) in time domain.

Note whether in spectral domain or time domain, there are interference fringes resulting from the interference of glass coating of employed spatial mask. In spectral domain, the free spectral range (FSR) in terms of optical spectrum is shown as $\Delta\lambda = \lambda^2 / 2\Delta l$, where Δl, 3mm, is the optical path difference (OPD) of two interferometric arms owing to the glass coating of spatial mask; λ is the optical wavelength, 1550nm. Hence the theoretical result of $\Delta\lambda$ is 0.40 nm, which is close to the experimental result of 0.41 nm. The interference fringes are not filtered in experiment as their period of is close to that of imaging patterns.

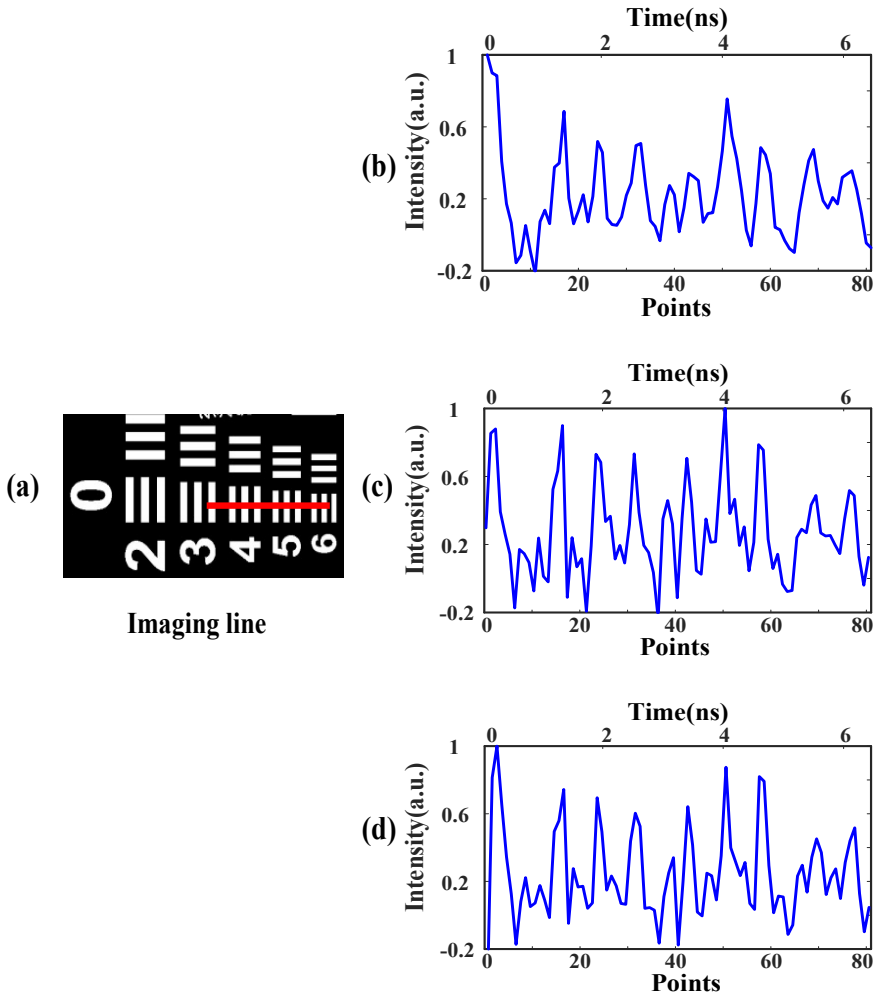

Figure 4.4 (a) The imaging sample of 1951 USAF resolution target, red line is the imaging area. Reconstructed line with (b) 35, (c) 40, and (d) 45 times of measurements with data compression ratio of 43.2%, 49.4% and 55.6%, respectively, based on minimum l1 norm reconstruction.

The spatial mask is performed as a passive optical random pattern generator in our demonstration. To perform a fast CSI system, a fast galvo-scanner could be applied

to change the height of time-stretched optical pulses that reaches different patterns from spatial mask or a mechanical scheme could be used to change the height of spatial mask rapidly.

In our CS computation, a line sample imaging $I_{M\times 1}$ with a length of M points is mixed with N random patterns from spatial mask, N is the number of measurements (N < M). $I_{M\times 1}$ can be expressed as [122]

$$I_{M\times 1} = \varphi_{M\times M} \times S_{M\times 1} \tag{4.1}$$

where $\varphi_{M\times M}$ is a M×M matrix denotes for Fourier orthogonal basis, $S_{M\times 1}$ is a M×1 matrix representing the spectrum of $I_{M\times 1}$ in transformation domain. Each pattern $R_{M\times 1}$ (also has a length of M points) stands for each measurement. The line sample imaging is sparse in discreet Fourier transformation (DFT) domain in presumption, N number of random patterns can be depicted as the M×N dimensional measurement matrix $R_{M\times N}$, and hence the measurement vector $y_{N\times 1}$, also known as dot product, is defined as [122]

$$y_{N\times 1} = R_{N\times M} \times I_{M\times 1} = R_{N\times M} \times \varphi_{M\times M} \times S_{M\times 1} = \theta_{N\times M} \times S_{M\times 1} \tag{4.2}$$

where $\theta_{N\times M} = R_{N\times M} \times \varphi_{M\times M}$.

Imaging information recovery from $y_{N\times 1}$ to $I_{M\times 1}$ is a process of convex optimization. The measurement vector $y_{N\times 1}$ and random pattern matrix $R_{M\times N}$ are given as inputs from the proposed system. $\varphi_{M\times M}$ is a standard orthogonal basis and the matrix product of $\theta_{N\times M}$ is random and meets the restricted isometry property [122]. Therefore, a valid and possible solution for $S_{M\times 1}$ is achievable using total variation (*TV*) minimization algorithm based on minimum *l1* norm reconstruction [101],

$$s = \arg\ \min(TV_1), \text{ subject to } \theta s = y \tag{4.3}$$

Hence, the presentation of transformation domain s can be obtained. Therefore, the 1D imaging information can be reconstructed due to $I_{M\times 1} = \varphi_{M\times M} \times S_{M\times 1}$.

The imaging sample of 1951 USAF resolution target used in our proposed system to perform CS technique is shown in Figure 4. 4(a). The imaging line is shown in the red line with a length (field of view) of 7.3 mm, which is group 0, number 3 to 6. Figure 4. 4(b), (c) and (d) illustrated the results of reconstructed 1D lines using different number of random patterns or times of measurement, which are 35, 40 and 45, and the data compression ratio are 43.2%, 49.4% and 55.6%, respectively, based on minimum *l1* norm reconstruction. From Figure 4. 4(d), when 45 times of measurement/random patterns are employed in our proposed CSI system, the target data stream with recovered a set of 81 data matched the original imaging line, which confirms the spatial all-optical mixing for CS method is applicable. Note there is some interference patterns resulting from spatial mask, which affected the final reconstructed results, however, this issue can be easily eliminated via using a transmission mode of spatial mask or a reflective spatial mask without glass coating.

4.3. Compressed sensing in time domain

OCT, which is based on low-coherence interferometry, is a fundamentally established optical imaging technique that uses broadband optical light as the light source to capture micrometer-resolution, multi-dimensional images [123–130]. OCT technique is widely utilized in cross-sectional tomographic imaging of internal microstructures of materials, especially in vitro in the human retina and other biomedical tissues.

There are mainly two types of OCT, frequency-domain OCT and time domain OCT. Frequency-domain OCT provides higher scan rate, offering greater stability and better signal-to-noise ratio compared to traditional time-domain OCT methods [131]. In the last decade, extensive efforts have been made to increase the utility of frequency-domain OCT towards further higher measurement speed. Impressive MHz axial scan rates have been achieved by using a new type of high-

speed frequency-sweeping optical source based on Fourier-domain mode locking [131], and by using channelized optical spectrum measurement with photodiode arrays [132]. Apart from targeting high-speed axial scanning, master-slave interferometry [133] was recent reported as an alternative high-speed solution for real-time enface display of frequency-domain OCT images.

4.3.1. Compressed sensing OCT system

To enhance higher axial scan rates, PTS is explored in frequency-domain OCT. This method uses large chromatic dispersion in optical fibres to map the broadband spectrum of an ultrashort optical pulse into a temporal waveform. Therefore, frequency-domain OCT measurement can be achieved alternatively in time-domain using a high-speed single-pixel PD, which enables PTS-OCT to operate at the axial scan rate equivalent to the pulse repetition rate of the laser, typically ranging from tens of MHz to even GHz. PTS-OCT was first implemented in the fibre-optic communication band (i.e., ~1550 nm) [134], in which ultrafast PDs and good dispersive elements with large dispersion-to-loss ratio are commercially available. PTS-OCT operating at a shorter wavelength range has also been implemented offering better axial resolution and less water absorption in biological samples [135]. PTS based OCT has been recently demonstrated to allow high-speed OCT imaging of biological tissues [136].

Although the PTS technique has enabled high-throughput OCT measurement thanks to the use of DCF, the instruments inherently produce an extremely high-rate data stream, which can be as high as one trillion bits per second [135]. This deluge of OCT image data will overwhelm even the most advanced data acquisition circuits and the backend digital signal processors. Most electronic solutions fall short in this case due to the electronic bottleneck in speed and bandwidth.

Therefore, new and efficient photonic approaches, which feature ultrafast speed and extremely broadband bandwidth, are highly demanded to address the emerging massive data problems in ultrafast OCT systems. As introduced in the previous chapters, CS is a promising data compression method, which could solve this

problem. And recent research efforts have also been made to explore the use of CS method in OCT systems for data compression. For example, in [94], a CS method has been employed in post processing to reconstruct 3D OCT images from a subset of the original images by exploiting the image sparsity. In [93], CS has been implemented in spectral domain OCT to reduce the total amount of original data from a CCD camera.

However, very little research work on data-compressed PTS-OCT has been reported so far, especially considering the fact that PTS-OCT suffers much more from massive data issues due to its high-throughput nature. Thus, photonic CS enabled data compression in high throughput PTS-OCT has been explored and experimentally demonstrated in the next part. Both random mixing and signal integration are implemented in the optical domain based on temporal modulation of time stretched optical pulse using PRBSs and pulse compression using opposite dispersion value. The proposed method not only overcomes the bottleneck of big data problems [104], but also provides an economic alternative to high-speed PTS-OCT data acquisition as a low speed (50MHz) detector is capable enough to capture compressed OCT data, which otherwise demands tens of GS/s sampling rate [114,134–136].

4.3.2. Experimental setup

Schematic diagram of proposed CS PTS-OCT system is shown in Figure 4. 5. The optical source is a passively MLL that produces a series of broadband ultra-short optical pulse train. The optical pulse is first stretched by a DCF generating a broadband passive wavelength swept optical carrier. The stretched pulse is then sent to a Michelson interferometer for real-time spectral-domain OCT measurement. Each frequency component of the pulse spectrum hence illuminates the sample successively in time. The back-reflected pulses from different layers of the sample are interferometrically combined with an unmodulated pulse reflected from a reference mirror at the optical coupler, resulting in an interference fringe in the time domain. The concept of PTS-OCT can also be understood based on frequency-to-time mapping: depth information of the sample is first encoded to

optical pulse spectrum, which is further mapped to a temporal waveform by large GVD of the DCF. The frequency-to-time mapping relation is characterized as $\lambda = t / \psi$, where ψ is the total chromatic dispersion (in ps/nm) of the DCF. Finally a spectral interferogramcan be captured in real time using a high-speed single-pixel photodetector.

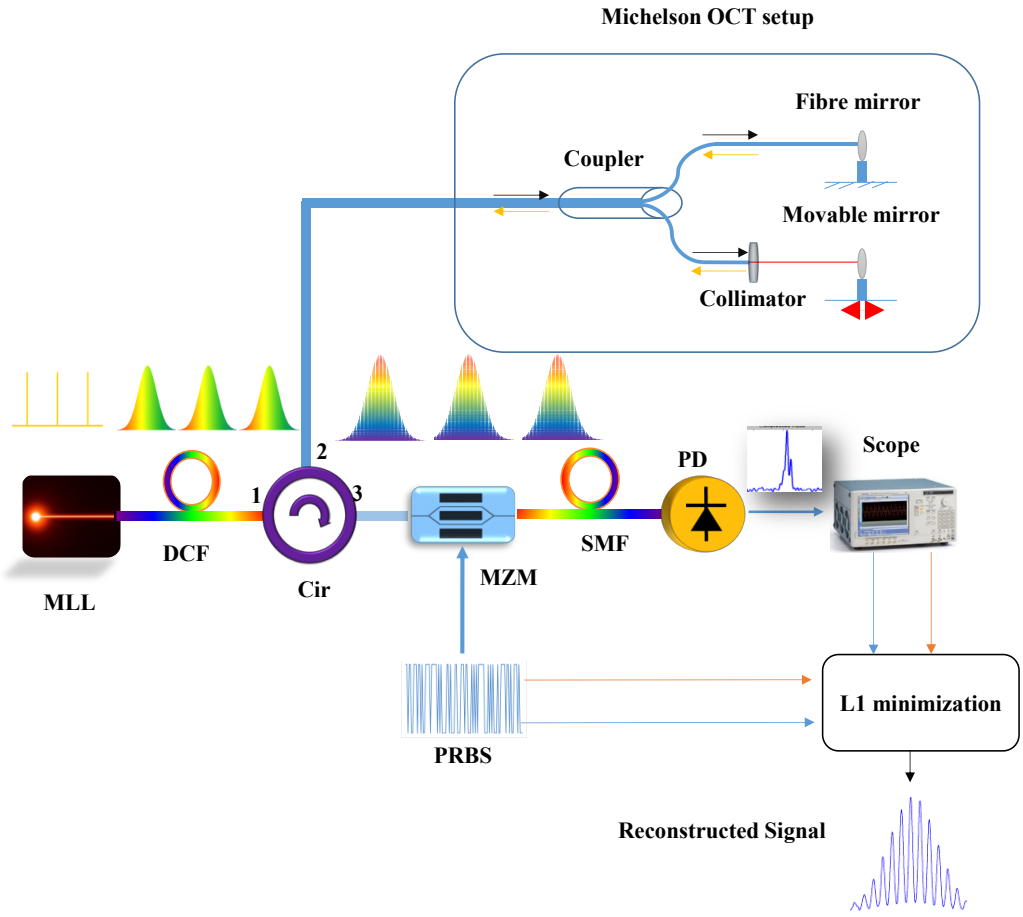

Figure 4.5 Block diagram of the proposed CS based PTS-OCT system.

In the Michelson-type interferometer set up, one optical fibre arm ends with a fixed fibre Faraday mirror and other arm is focused onto a moveable mirror, which emulates a single reflection-layer sample. This interferometer set up produces an interference fringe pattern in both the time and frequency domains. The optical path length difference between two arms is considered to be

$$\Delta L = n_g L - L_1 \tag{4.4}$$

where n_g is the refractive index of the fibre in the fixed arm, L is the optical fibre length between the end of fibre mirror and fibre connector in fixed arm, L_1 is the free space length between the collimator and the tunable mirror. Free spectral range (FSR) in interference spectrum in terms of optical wavelength can be calculated as

$$\Delta\lambda = \frac{\lambda^2}{2\Delta \mathrm{L}} \tag{4.5}$$

Thanks to the dispersion-induced wavelength-to-time mapping, this interference spectrum is converted to a temporal interference pattern with its period given by $\Delta t = \Delta\lambda * \psi$. It can be easily deduced from equation (4. 2) that the relation between RF frequency of the interference pattern and optical path length difference can be established as

$$\mathrm{f_{RF}} = \frac{1}{\Delta \mathrm{t}} = \frac{2\Delta \mathrm{L}}{\lambda^2 \psi} \tag{4.6}$$

Therefore, the optical path length difference and hence the depth information of the sample can be uniquely determined from the RF frequency at a refresh rate identical to the pulse repetition rate.

CS theory shows that a frequency-sparse signal, such as the time-encoded OCT signal, can be recovered from a reduced number of measurements in a single-pixel receiver scheme such as the PTS-OCT system, which leads to significant data compression. CS normally involves three successive steps: random mixing, integration (or equivalently low-pass filtering), and down-sampling. The original signal can be then reconstructed following a minimization algorithm. The specific algorithm has been discussed in chapter 2.5.1.

To verify the utility of the proposed compressed sensing PTS-OCT system, a proof of concept experiment has been designed and implemented based on the setup shown in Figure 4. 5. In the experiment, the optical source is a passively MLL (Calmar Mendocino FP laser), which produces a series of ultrashort optical pulses with FWHM of 800 fs and repetition rate of 50 MHz. After being time stretched using a DCF with total dispersion of 1.04 ns/nm, the optical pulses are directed to a

Michelson-type OCT setup where one arm is an optical fibre ended with a fibre Faraday mirror and the other is in free-space towards a moveable mirror emulating as a single-layer sample. Tuning to a particular path difference, the depth profile is encoded into the RF frequency of the mapped temporal waveform.

4.3.3. Experimental results and discussions

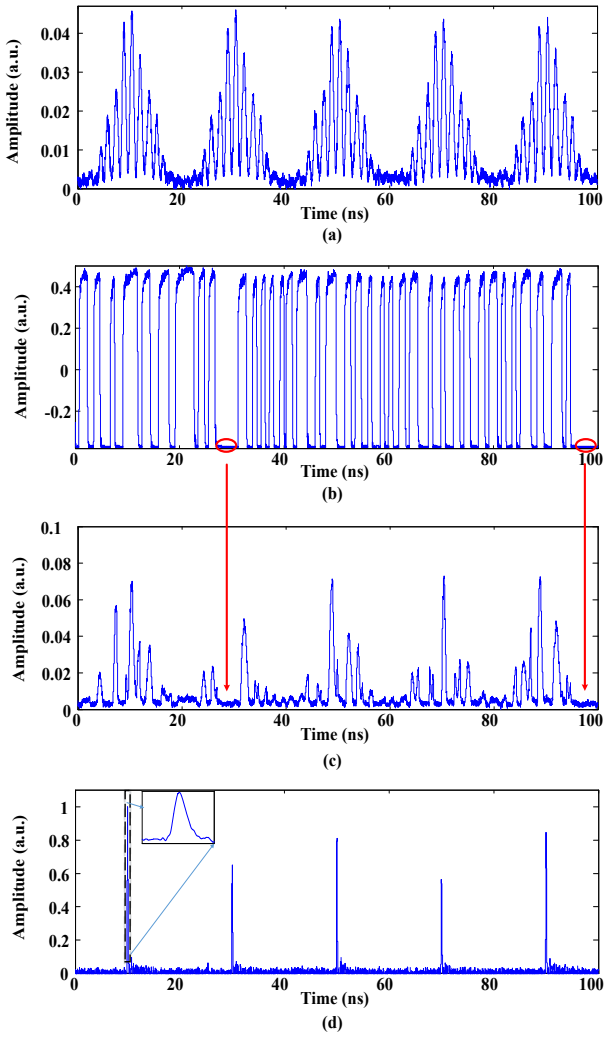

Figure 4.6 Experiment results for a single-layer PTS-OCT measurement. (a) The temporal interference pattern for five successive pulses. (b) The first 5 PRBS patterns. (c) The modulated waveforms with red marking showing no pattern for exact amount of duration of a bit 0. (d) The compressed optical pulses using a SMF with opposite dispersion profile.

The first five consecutive pulses are captured using a high-speed PD and a real-time oscilloscope and shown in Figure 4. 6 (a). We can see the stretched Gaussian pulse

is encoded with a single tone RF frequency indicating the strong single-layer reflection from the sample. PRBS patterns at 2.5 Gbps are generated by an AWG (Tektronix AWG7122C) as shown in Figure 4. 6 (b). Considering Nyquist rate of 2.5 Gbps and pulse period of 20 ns, the original signal length is N = 50. Mixing of PRBS patterns with the encoded optical pulses is implemented using a 10 GHz MZM with the results captured by the oscilloscope and shown in Figure 4. 6 (c). Passing the randomly mixed pulses through a SMF with opposite dispersion profile, signal integration has been realized via pulse compression. The compressed pulses are detected with a 2.5 GHz PD and shown in Figure 4. 6 (d). The pulses have a pulse-width of 0.4 ns which is inversely proportional to the PD bandwidth. The peak power of each pulse indicates the integration of mixed optical pulse and leads to a single measurement result.

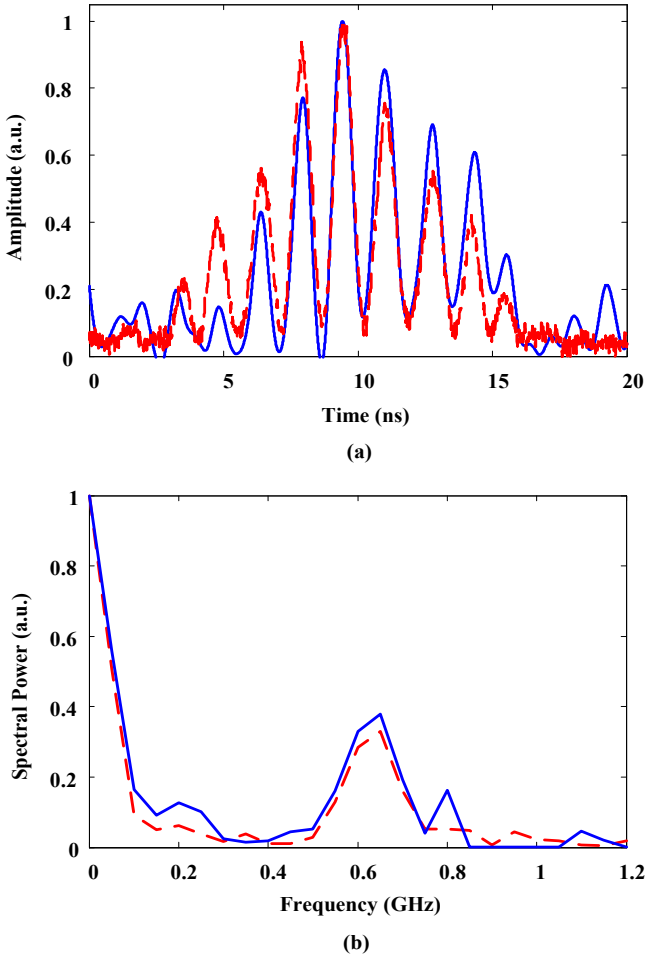

Figure 4.7 (a) Overlapped temporal waveforms for the reconstructed signal (in solid line) and the original signal (in red dash line). (b) Fourier domain representation of the reconstructed signal (in solid line) and the original signal (in red dash line).

The Fourier transform of the interference waveform is indicated by the red dotted line in Figure 4. 7 (a). A clear peak at 650 MHz is obtained, which corresponds to an optical path length difference of 0.81 mm. Overall 33 measurements have been taken to reconstruct the original signal (50 data) following an l1 Magic minimization algorithm. The reconstructed DFT domain signal is shown with solid line in Figure 4. 7 (b). We can see that the target frequency (650 MHz) has been successfully recovered with a data compression ratio of 66%. Figure 4. 7 (a) shows the reconstructed time domain signal and the original signal with blue solid and red dotted line respectively. A good match in time-domain reconstruction has been achieved. Data compression is achieved in PTS-OCT at the cost of reduced axial scan rate. The effective axial scan rate in this experiment is 1.51 MHz. A better compression ratio (due to fewer number of measurements) will increase the scan rate as well.

A second experiment was carried out to verify the utility of the system at different imaging depths. We tune the moveable mirror further to get an increased optical path length difference of 0.99 mm. The mapped spectrally-encoded optical pulse has a higher carrier frequency of 800 MHz, with its time-domain and frequency-domain representations shown in Figure 4. 8 (a) and (b) respectively. The same random mixing and optical pulse compression processes are carried out. With 33 measurements, the reconstructed time-domain and DFT domain signals are shown in Figure 4. 8 (c) and (d) respectively. The reconstructed signal matches well with the original signal with a compression ratio of 66%.

This proposed and experimentally demonstrated data compression approach based on photonic CS for data-efficient PTS-based OCT systems is confirmed applicable in OCT applications. Random mixing and integration processes were implemented in the optical domain directly free from the electronic bottleneck. High-throughput axial scanning at 1.51 MHz has been achieved using low-speed data acquisition at 50MS/s thanks to photonic compressed sensing with a compression ratio of 66%.

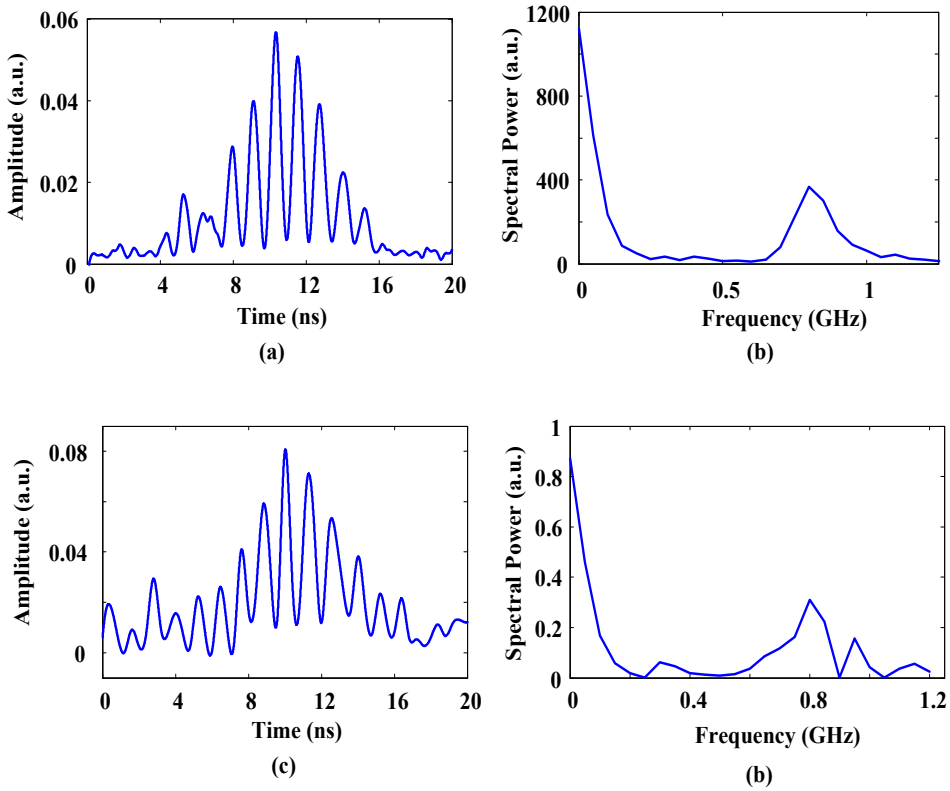

Figure 4.8 Experimental results for a second single-layer sample with different path length difference. (a) The original interference pattern in time domain. (b) Fourier transform of the original interference pattern showing a single carrier frequency of 800 MHz. (c) The reconstructed time domain waveform with 33 measurements. (d) The reconstructed DFT domain signal clearly identifying the 800 MHz frequency component.

4.4. Summary

In this chapter, the spatial domain and time domain CS systems based on PTS technique are proposed and experimentally demonstrated.

First, we proposed and experimentally demonstrated a low cost all-optical CSI system using STEAM structure with potential dynamic phenomena detection. The spatial mask is performed as passive optical random pattern generator, which is applied for all-optical mixing to perform spatial domain compressed sensing, hence, no electrical bandwidth is limited and no expensive electro-optical modulator is involved. The experimental result of CSI system shows a data compression ratio of 55.6% is performed using a computational low-speed data acquisition at 50MS/s.

Our proposed system could solve the big data issue in the traditional data acquisition procession and reduce the cost of system using low-bandwidth PD and oscilloscope with potential dynamic phenomena detection and measurement.

Second, an OCT system using CS and PTS techniques is proposed and experimentally demonstrated as a data compression approach. A comprehensive analysis and experimental verifications are presented. The usage of random mixing and integration processes in the optical domain directly overcomes the electronic bottleneck. High-throughput OCT measurements with axial scanning at 1.51 MHz has been achieved using low-speed data acquisition at 50MS/s with a compression ratio of 66% is performed.

CHAPTER 5: COMPRESSED SENSING AND PTS BASED SPI USING MULTIMODE INTERFERENCE

5.1. Introduction

In this chapter, MMF is introduced as a low-cost CS imaging approach, which obtained world-class unprecedented speed.

MMF, which caused randomization of phase, polarization and optical speckle pattern intensity distribution when light travels through it, has bigger core, higher capacity and larger numerical aperture in comparison with SMF. Hence it enables different kinds of applications and attracts extensively resurging attention in communication [82,83], and imaging [75–81], especially SPI-based systems [8–12].

The theory and introduction of PTS [23,98,114] and CS [92–94] are presented in chapter 2 and chapter 4, respectively. In CS technique, the high speed of PRBS has the disadvantage of high cost while the low-cost of SLMs and DMDs has drawback of comparatively low frame speed. As a result, high-speed with low-cost optical random patterns in time-serial is required. To conquer this challenge, PTS and CS based multimode interference using MMF is utilized. The optical random patterns in MMF are generated thanks to its feature of randomization of optical speckle pattern intensity distribution when light travels through it. When combined with PTS technique using a broadband short pulsed laser / mode-locked laser (MLL), different wavelengths from a MLL will propagate the MMF in time serial, thus a random optical speckle pattern generator is produced with unprecedented speed.

With the utilization of MMF, and combination of CS and PTS, unprecedented CS imaging speed under same laser source condition can be obtained. The frame rate of proposed imaging system is equal to the repetition rate of the pulsed laser. Compared to traditional all-optical random pattern generator that using SLM or

DMD, which generates hundreds or tens of thousands of random speckle patterns in one second, ultrashort optical pulse with broadband spectrum that passes through a single capsuled MMF based PTS could introduce an all-optical random speckle pattern generation speed of tens of GHz, which is around 6 to 7 orders higher. When in comparison with other PRBS-based high-cost CS and PTS imaging system, such as OCT [92–94] and STEAM [23,98,114], which need hundreds of times iteration of a single ultrashort optical pulse to reconstruct one frame, the low-cost frame rate of proposed imaging system is hundreds of times faster thanks to its fundamental nature.

5.2. Ultrafast CS imaging system based on multimode interference

We present our conceptual imaging system with combination of CS and PTS based on the employment of multimode interference using MMF. Via the usage of MMF, our proposed system has the benefit of ultrafast all-optical random speckle pattern generation speed with low cost and ultra-wide bandwidth in comparison with narrow bandwidth PRBS generator and low speed SLMs / DMDs. Also, it has the advantage of inherent 2D imaging reconstruction due to its nature of 2D spatial speckle intensity profile distribution.

To gain a better understanding of our proposed system, a combination of analysis with computation and experiment is presented. The all-optical random speckle patterns, generated in a single capsuled MMF via light of different wavelengths travelling through it in time serial, are experimentally analysed and demonstrated. The theory of MMF based PTS using CS method for imaging is presented.

5.2.1. Experimental setup of MMF based CS imaging system

Each single wavelength of light will generate its own random and repeatable optical speckle pattern in time sequence when travels in a single capsuled MMF. The all-

optical random speckle patterns are generated via the light of different wavelengths that travels in a capsuled MMF due to the multimode interference. By the implementation of PTS, ultrashort optical pulse of broadband spectrum can be stretched in temporal domain. Thus all-optical random speckle patterns can be generated once the stretched pulses propagating through the MMF. The process diagram is shown in Figure 5. 1. At each time, only one certain optical speckle pattern at one wavelength is generated (the mode dispersion can be neglected if selectively choose short length MMF and control the incident light when propagating through MMF). However, the time difference between each wavelength is extremely short, which could be around 0.1ns. The traditional imaging method for photon-detection and data acquisition in such ultrafast speed needs bandwidth of trillions of Hz and sampling speed of trillions of samples per seconds. In our case, CS technique is employed to conquer the limitation and a 10GHz bandwidth single-pixel PD can be used to reconstruct the image.

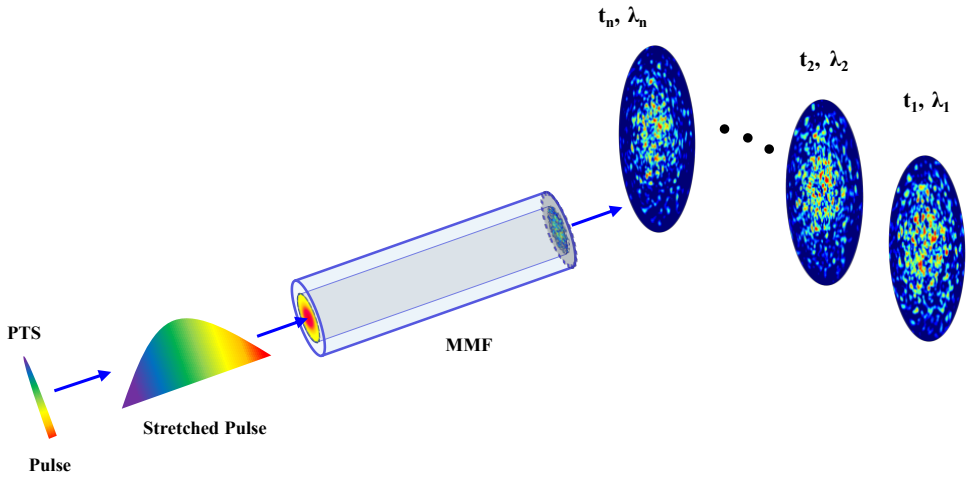

Figure 5.1 The process diagram of pulse stretch and all-optical random speckle pattern generation via the combination of PTS and MMF.

In our experiment, the spread of random distributed optical speckles can be tuned via tuning the angle of incident light that transmitted into the MMF. Hence, in this case the randomization and spatial intensity distribution of optical speckles, which determines the success of our experiment, can be optimized.

To ensure the process of MMF based CS imaging using PTS, the calibration process of MMF for optical speckles distribution of various wavelengths is presented. Figure 5.2 gives the calibration process of random all-optical speckle patterns via wavelength tuning. A TL with wavelength range from 1518 nm to 1568 nm is exploited to provide the narrow bandwidth single wavelength. Light from TL will be emitted into open space via a collimator (Col) with NA of 0.49. A lens set of two plano-convex lens with focal lengths of 30 mm and 100 mm is used to expand the open space beam size. An objective lens (OL, ×10, 0.40NA) is put after the lens set to coupling light of different angles of single wavelength at each certain time into the capsuled MMF (with a length of 2m and a core diameter of 200μm, 0.39NA). Therefore, different modes are produced in MMF and each wavelength stands for each speckle pattern. Finally, the speckle patterns are captured by a beam profiler (BP). The single MMF is capsuled and only wavelengths of light can affect the random intensity distribution of optical speckle patterns.

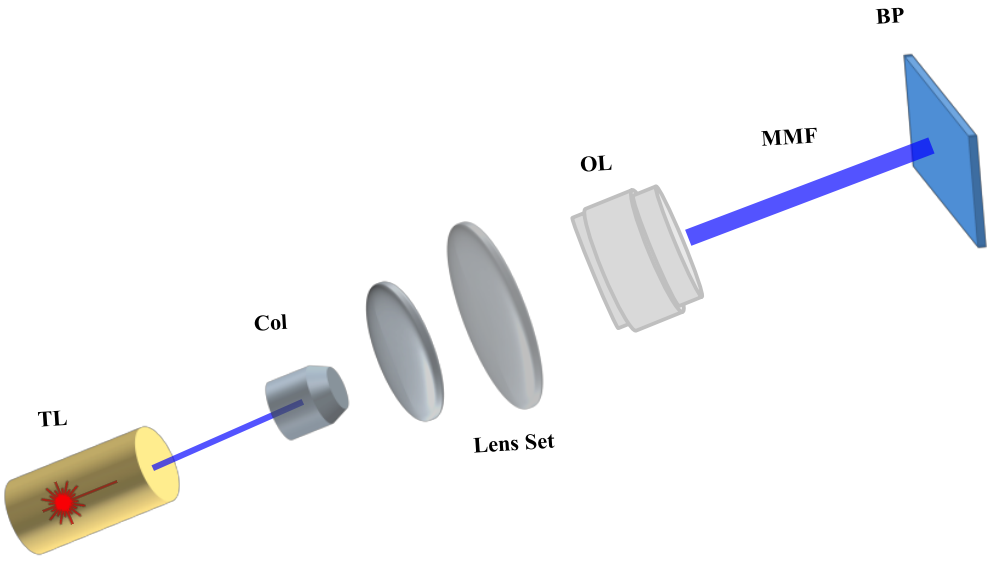

Figure 5.2 Schematic of calibration process of random all-optical speckle patterns via wavelength tuning.

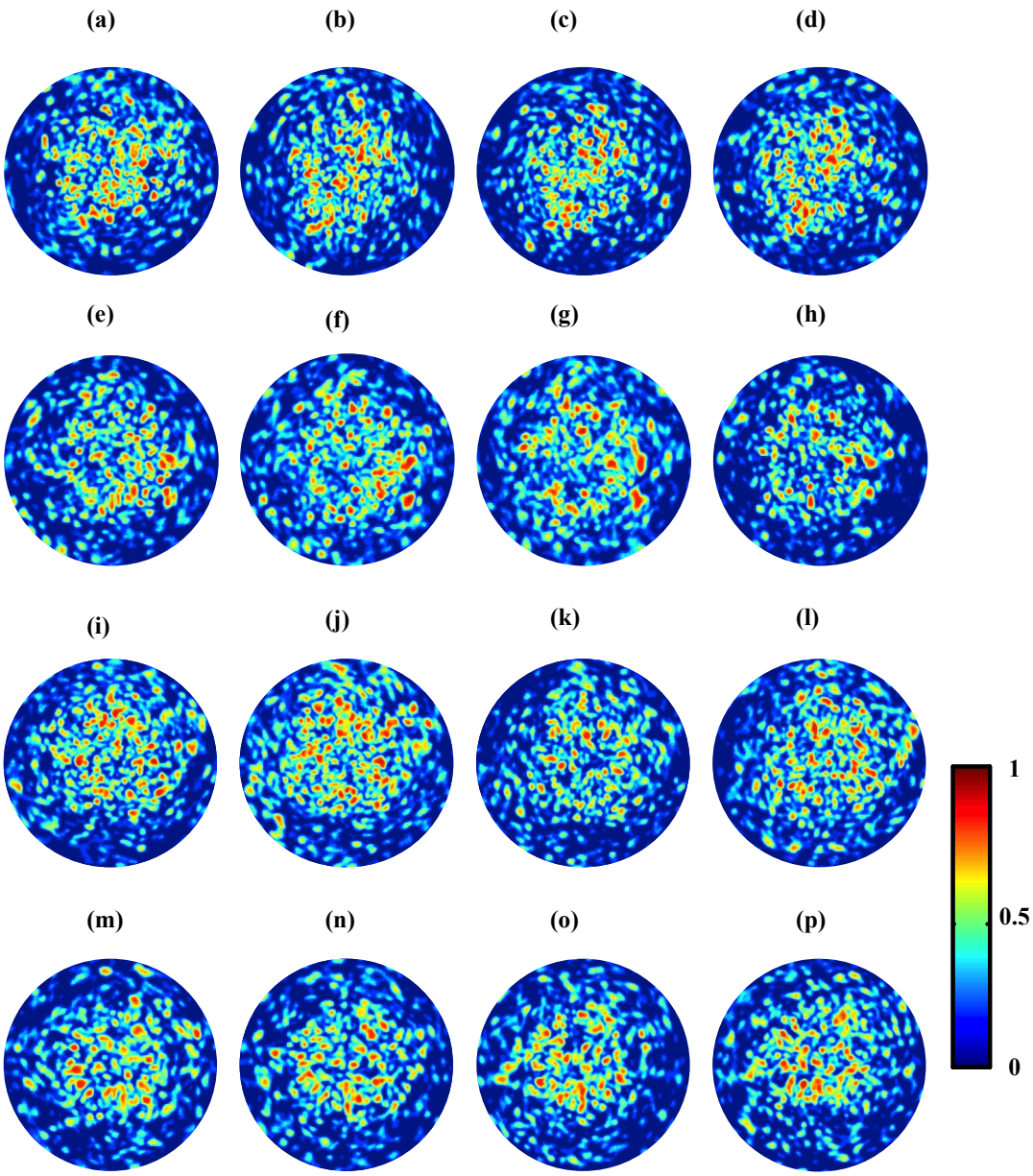

Figure 5.3 All-optical random speckle patterns at (a) – (d) 1520.0 – 1520.3nm; (e) – (h) 1530.0 – 1530.3nm; (i) – (l) 1540.0 – 1540.3nm; (m) – (p) 1550.0 – 1550.3nm, with 0.1 nm step.

One major principle must be satisfied in CS technique is that the random all-optical speckle patterns should be stable, repeatable, while at the same time all the other patterns of different wavelengths should be completely uncorrelated. Part of the random all-optical speckle patterns generated in our experiment is shown in Figure 5. 3, all-optical random speckle patterns at four wavelength bands are shown and each band has 4 wavelength-dependent random speckle patterns with 0.1nm

wavelength step ((a) – (d), 1520.0 – 1520.3nm; (e) – (h), 1530.0 – 1530.3nm; (i) – (l), 1540.0 – 1540.3nm; (m) – (p), 1550.0 – 1550.3nm), which shows the randomization of generated all-optical random speckle patterns spatially.

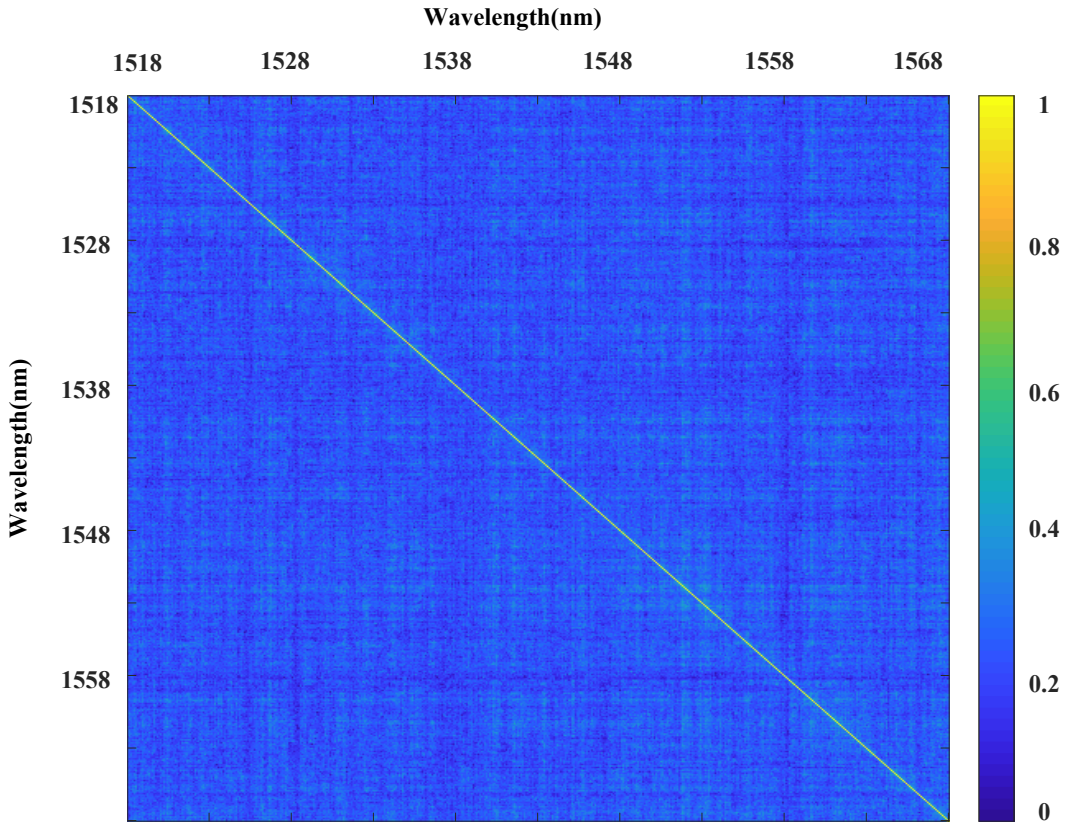

Figure 5.4 Correlation of 500 optical speckle patterns from 1518.0 to 1567.9 nm with 0.1 nm step.

To quantitatively determine the randomization of the all-optical random speckle patterns, a correlation of 500 stable and repeatable wavelength-dependent random all-optical speckle patterns are analysed and the correlation result is shown in Figure 5. 4. The wavelength range from TL is 1518.0 to 1567.9 nm with 0.1nm tuning step. The ideal correlation between every other two wavelength-dependent random all-optical speckle patterns should be as close to 0 and the self-correlation of one certain wavelength-dependent random speckle pattern should be as close to 1. In Figure 5. 4, the average correlation value among every two different patterns in the 500 patterns is 0.074, and the self-correlation value of the 500 patterns is 1.

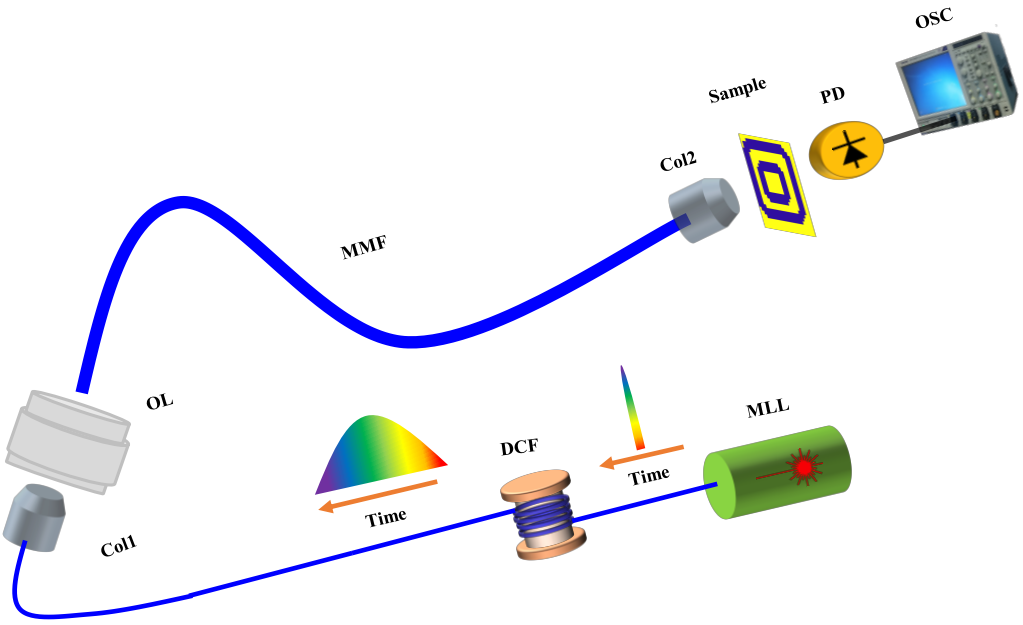

Figure 5.5 Schematic of proposed imaging system based CS and PTS using MMF.

The schematic of proposed imaging system based CS and PTS using MMF is shown in Figure 5. 5. The capsuled MMF in this setup is performed as a low-cost, ultrafast and passive all-optical random speckle pattern generator and the capsulation is performed to minimize the effect of the environment, which can fatally affect the stability of the all-optical random speckle patterns. A MLL with a repetition rate of 20MHz is utilized to generate the ultrashort pulses with broadband spectrum. The ultrashort pulses go through the DCF (with a whole dispersion of 1ns/nm) to perform PTS, namely, dispersive Fourier transform. Therefore, linear wavelength-to-time one-to-one mapping is achieved. The time stretched pulses are emitted into open space via a collimator (Col) with a NA of 0.49. Then the pulses are coupled into capsuled MMF (with a length of 2m and the diameter of its core is 200μm, 0.39NA) via pass through an objective lens (×10, 0.40NA), which induces more modes that could improve the randomization of the optical speckles. When each of the time-stretched broadband spectrum pulses propagates through the capsuled MMF, each wavelength in a pulse generates its own random, stable and repeatable 2D all-optical speckle pattern at its own time point. After the all-optical random speckle patterns in time serial pass through the target image, a single-pixel PD with properly chose bandwidth is used to receive the data. The final data are

collected by an oscilloscope (OSC) with a sampling rate the same as the bandwidth of the PD numerically.

5.2.2. Result and discussion

The computed data received by PD is illustrated in Figure 5. 6. A PD with a bandwidth of 10GHz is employed. The MLL has a wavelength range of 1518 nm to 1568 nm in simulation. Every 0.1ns (0.1nm in spectrum) is a measurement in our CS technique.

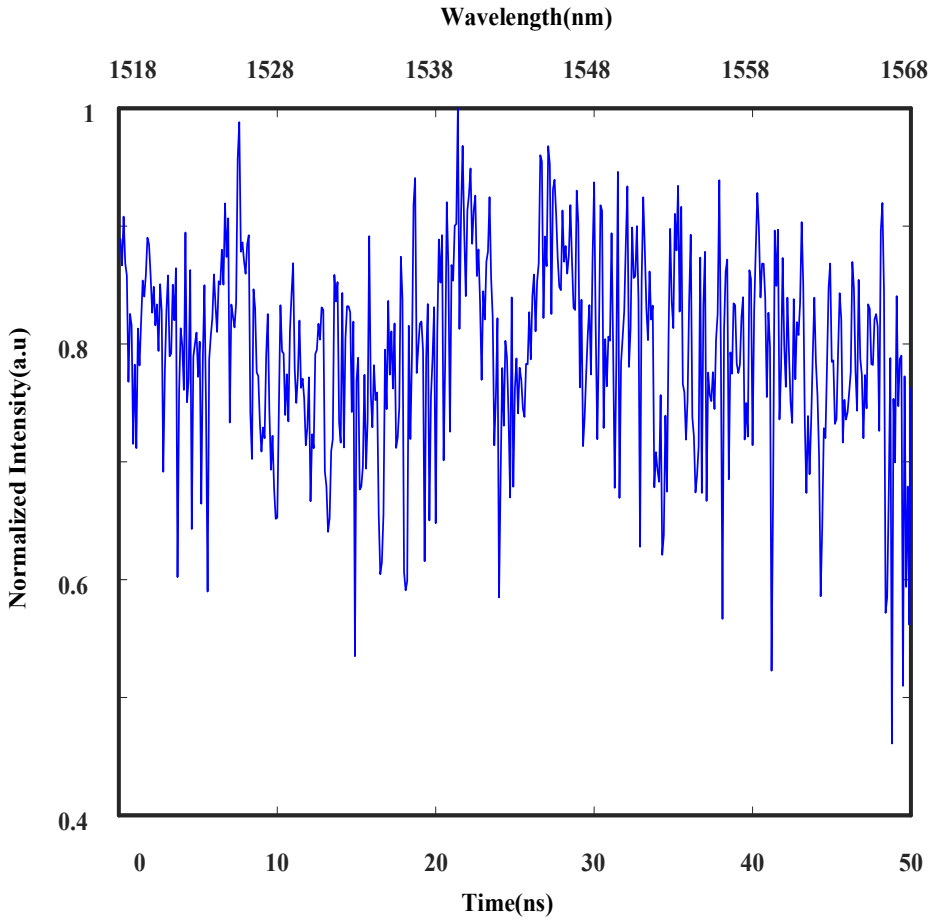

Figure 5.6 The computed signal received by PD in temporal domain (500 data of all-optical random speckle patterns).

In our CS computation, a target 2D image $I_{M\times M}$ is mixed with N random patterns, each $R_{M\times M}$ corresponding to a specific wavelength. N also corresponds to the number of measurements ($N << M\times M$). By vectoring the image into 1D ($I_{MM\times 1}$) and combining N random patterns ($R_{MM\times N}$), the CS system can be simplified into 1D model. The image $I_{MM\times 1}$ is assumed to be sparse in DFT domain, the measurement vector $y_{N\times 1}$ can be described as the dot product between the image and random patterns, $y_{N\times 1} = R_{N\times MM}\times I_{MM\times 1}$. Image $I_{MM\times 1}$ can be represented in transformation domain $\varphi_{MM\times MM}$ as $S_{MM\times 1} = \varphi_{MM\times MM}\times I_{MM\times 1}$, where $S_{MM\times 1}$ denotes the transformation domain representation. Hence the equations can be summarized as $y_{N\times 1} = R_{N\times MM}\times\varphi^{-1}_{MM\times MM}\times I_{MM\times 1} = \theta_{N\times MM}\times S_{MM\times 1}$, where $\theta_{N\times MM} = R_{N\times MM}\times\varphi^{-1}_{MM\times MM}$.

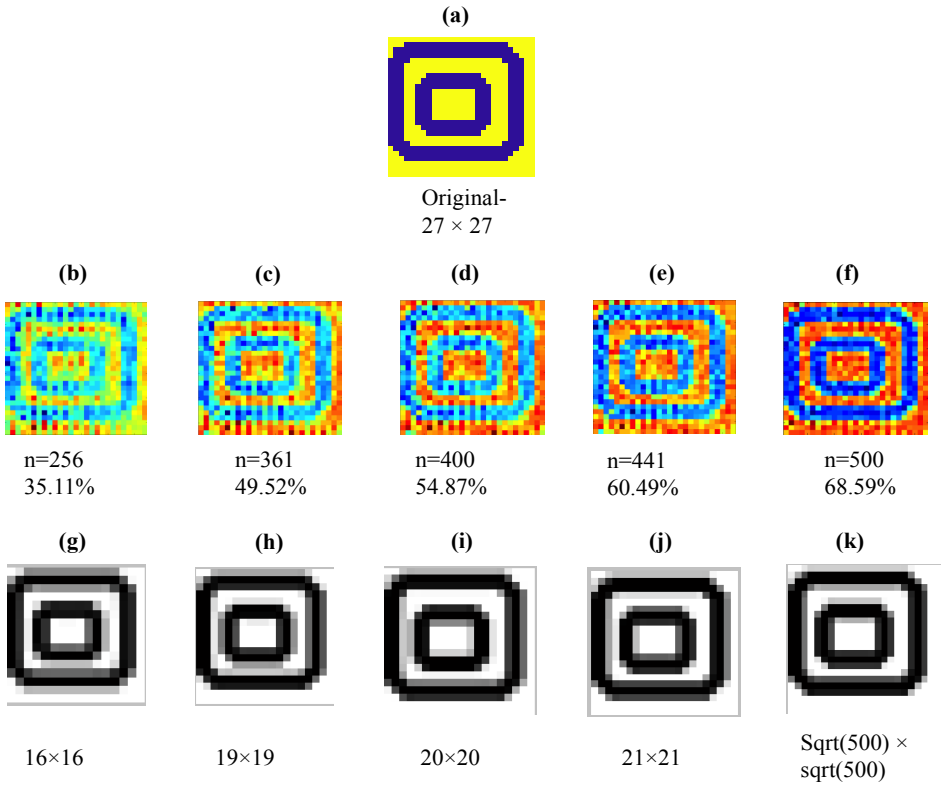

Figure 5.7 (a) An original target image with pixels size 27 × 27; (b) ~ (f), reconstructed images using different number of all optical random optical speckle patterns (different compression ratios from 35.11% to 68.59%); (g) ~ (k), CCD images downsized from (a) with corresponding same pixels size as (b) ~ (f).

In the imaging reconstruction region, the measurement vector $y_{N\times 1}$ and $R_{N\times MM}$ are given as inputs and the transformation domain $\varphi_{MM\times MM}$ is known, Hence $S_{MM\times 1}$ can be reconstructed using total variation (TV) minimization algorithm, $(TV_1)\min TV(s)$ subject to $\theta s = y$ [137]. From the retrieved transformation representation output s, the image can be reconstructed as, $I_{MM\times 1} = \varphi_{MM\times MM} \times S_{MM\times 1}$ and can be devectorized to get the 2D image $I_{M\times M}$.

An original customer-designed 27 × 27 pixels image (shown in Figure 5. 7(a)) is employed in our setup as the target image to perform CS technique. Figure 5. 7(b) to (f) show the reconstructed images with different number of all-optical random speckle patterns that used in CS technique, which is from 256 to 500 (with compression ratios from 35.11% to 68.59%). And from the result we could get the conclusion that the CS technique in our proposed imaging system can work as expected to fulfill the low-cost ultrafast imaging purpose with distinguishable resolution, and the more speckle patterns that used in CS technique, the more details can be identified in the reconstructed image. To compare the imaging effect of our CS technique, images of different CCDs with the same pixels size as Figure 5. 7 (b) ～ (f) are employed to receive the target image of Figure 5. 7 (a), and the images are shown in Figure 5. 7 (g) ～ (k). From Figure 5. 7 (g) to (k), the images get more elaborated as more pixels are used in the CCD. This result confirms our proposed imaging technique is an achievable approach of ultrafast SPI imaging method.

An original four-line-target image with pixels size 27 × 27, which is shown in Figure 5. 8 (a), is utilized to exemplify the resolution effect of CS imaging. Reconstructed images with different compression ratios / numbers of speckle patterns used from 35.11% / 256 to 68.59% / 500 are depicted from Figure 5. 8 (b) to (f), respectively. The result shows that the CS technique in our proposed imaging system matches quite well with the target image. To compare the imaging effect of our CS technique, images of different CCDs with same pixels size as Figure 5. 8 (b)

to (f) are employed to receive the target image of Figure 5. 8 (a), and the images are shown in Figure 5. 8 (g) to (k). Compared to images of different CCDs with same pixels size respectively, the CS imaging can offer better resolution in the target image although with the sacrifice of SNR, such as in comparison with Figure 5. 8 (h) and (k), (c) and (f) show more accurate details in the edge areas, especially notable with the first and last narrow lines.

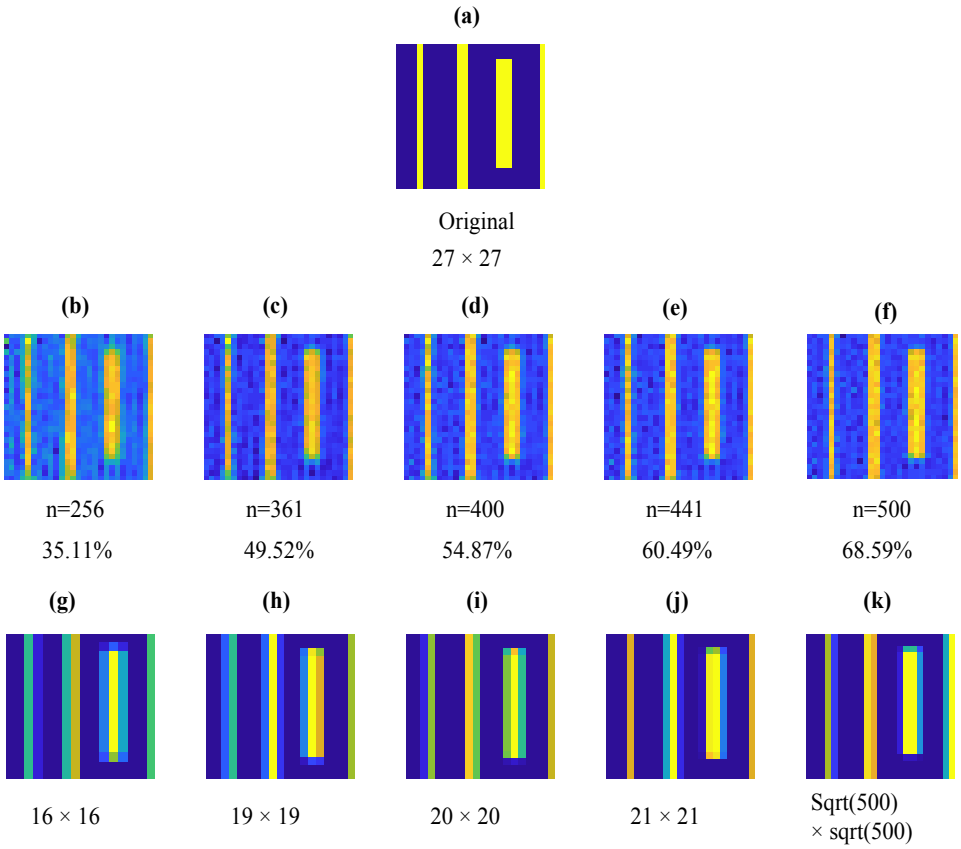

Figure 5.8 (a) An original target image with pixels size 27 × 27; (b) to (f), reconstructed images using different number of all-optical random speckle patterns (different compression ratios from 35.11% to 68.59%); (g) to (k), CCD images downsized from (a) with corresponding pixels size as (b) to (f).

The FFT spatial resolution of our system is analyzed based on the random speckle patterns we used in the CS process. Given a range of all-optical random speckle patterns generated in the MMF, the resolution is estimated to be 42 × 42 pixels.

Though the pixel resolution is 540 × 540, the random pattern cannot resolve the image of that size as the spatial resolution is limited by the random distance among

the speckles. Here we demonstrate the actual random pattern captured by the beam profiler along with spectral profile of the random pattern followed by several spatial low pass filters to remove the high frequency components to see any significant difference in the pattern. As observed, the actual figure captured by beam profiler with 540 × 540 pixel resolution is shown in Figure 5. 9 (a). The corresponding 2D spectral domain representation is shown in Figure 5. 9 (b), after removing the dominant low frequency component with a low pass filter and actual spectral power variation is shown in Figure 5. 9 (c), where the spectral power significantly decreases on higher spatial frequencies.

The higher spatial frequencies >150 are now suppressed using a low pass filter and the result is shown in Figure 5. 9 (f). The corresponding random pattern is shown in Figure 5. 9 (d), and the corresponding 2D FFT representation is shown in Figure 5. 9 (e).

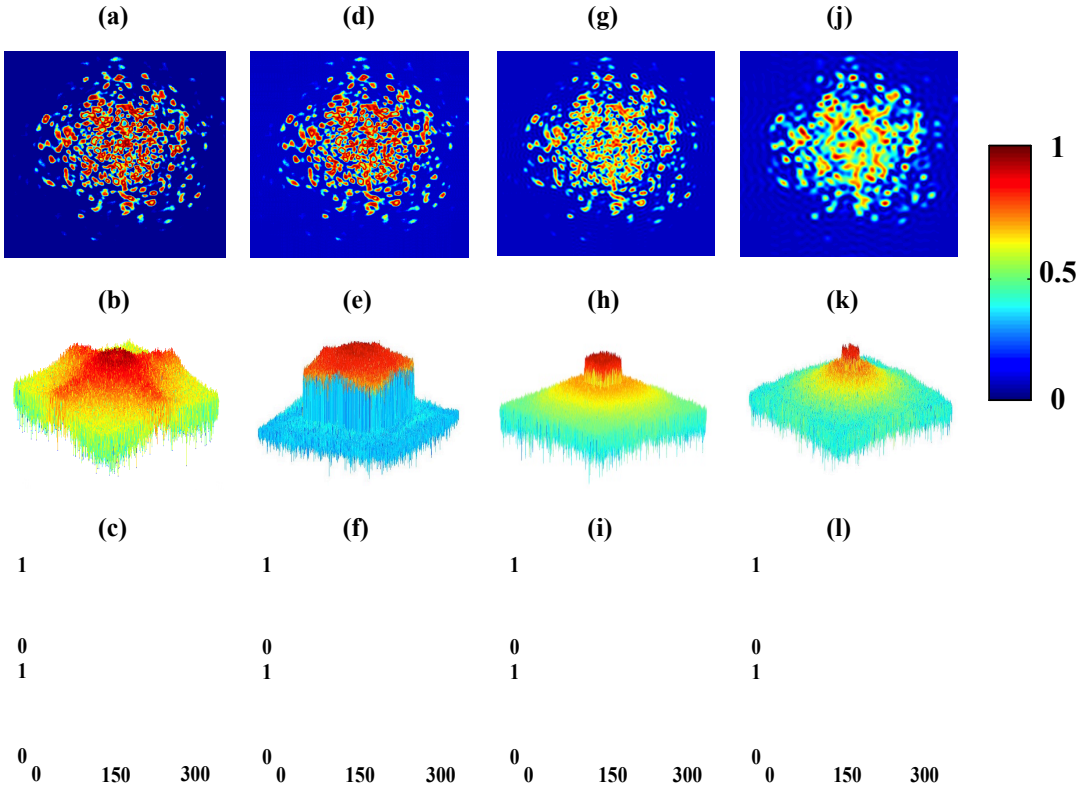

Figure 5.9 (a) Pattern captured by beam profiler with 540 × 540 pixel resolution; (b) 2D spectral domain representation after removing the low frequency components; (c) Superimposed spectral domain representation of individual rows of the image followed by superimposed representations of the columns of the image shown in (a); (d), (e), (f) and (g), (h), (i) and (j), (k), (l) are repetition of process of (a), (b), (c).

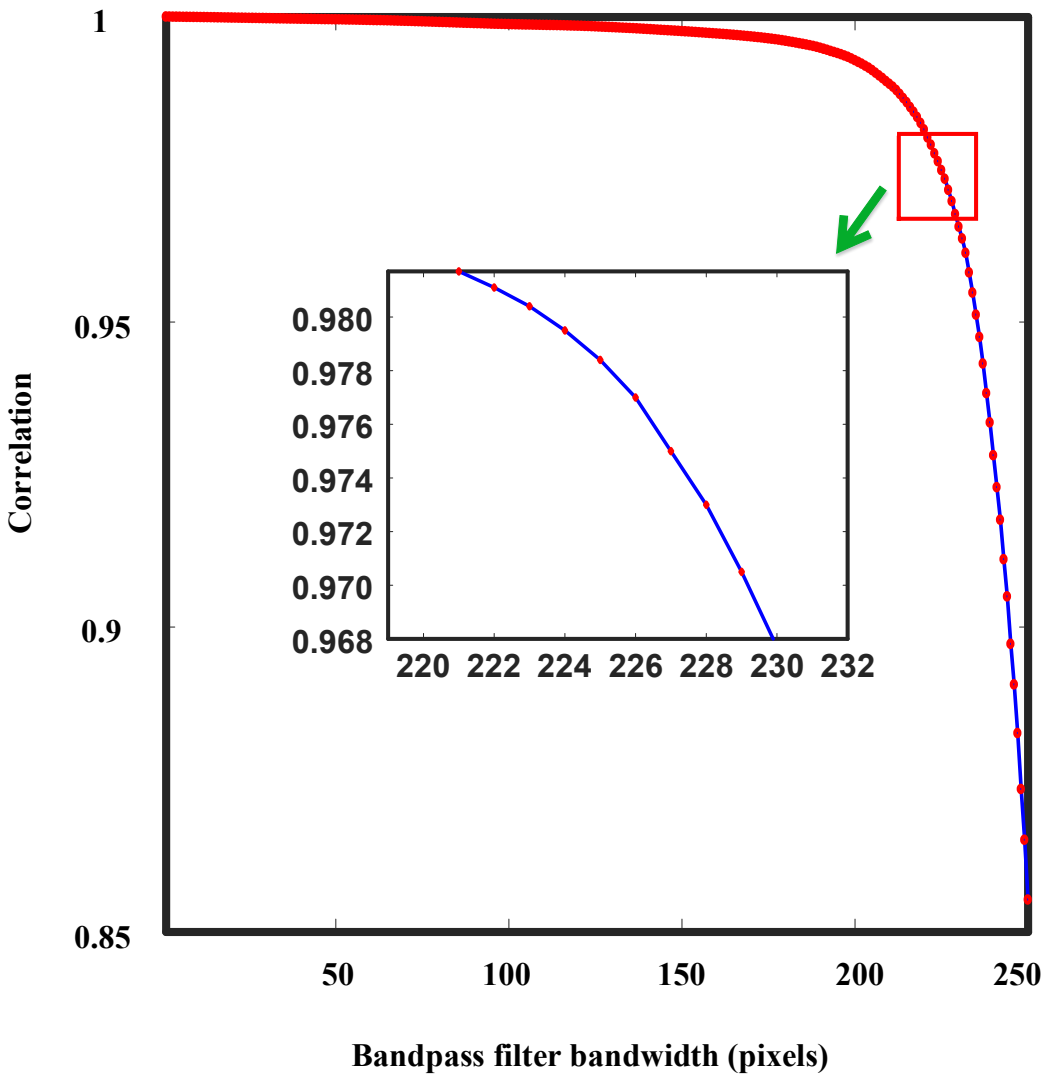

Figure 5.10 Correlation of original image with spatial frequencies filtered image, the correlation result is 0.97 for our spatial resolution.

Similarly the superimposed spectral domain representations of the pattern after removing the higher spatial frequencies >50 are shown in Figure 5. 9 (i), corresponding random pattern is shown in Figure 5. 9 (g), and 2D FFT representation is shown in Figure 5. 9 (h). The procedure is repeated for spatial frequencies >25 and the results are represented in Figure 5. 9 (l), (j), (k), respectively. As observed from the patterns with original Figure 5. 9 (a) and suppressed high frequency random pattern in Figure 5. 9 (j), some of the high frequency features have been lost marginally and this can be considered Nyquist frequency limit for the system. The result in our system is 42 × 42 pixels. The

correlation graph of original image with spatial frequencies filtered image is shown in Figure 5. 10, the correlation result is 0.97 for the existing spatial resolution.

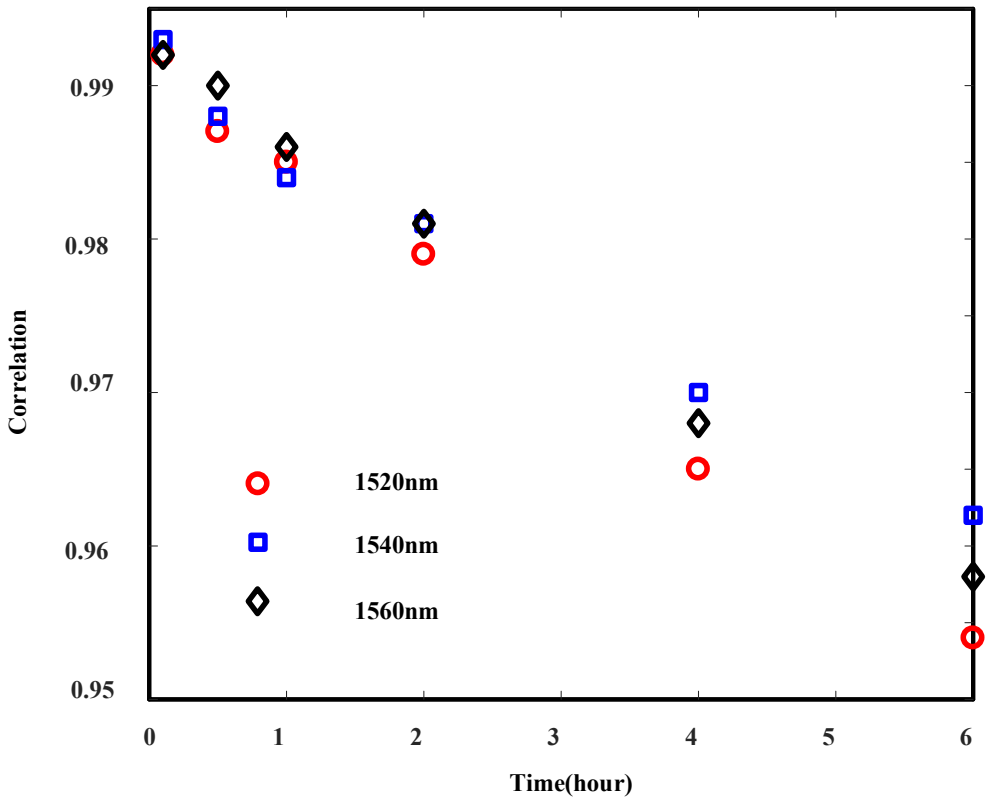

Figure 5.11 The temporal stability of optical speckle patterns within 6 hours.

The temporal stability of the all-optical random speckle patterns is analyzed via the correlation of previous and latter pattern within same wavelength at different captured time. The result is described in Figure 5. 11, three wavelengths of 1520 nm, 1540 nm and 1560 nm is used to exemplify the stability of all-optical random speckle patterns within 6 hours. The results show within one hour, all the patterns have correlation values of more than 0.985, although the value decreased as time increasing, the value is still above 0.95 within 6 hours. The calibration time of all-optical random speckle patterns is one pattern per second, so the whole calibration time of 500 patterns we used is 500 seconds. The frame speed in our proposed imaging system is 20MHz. Thus to make our proposal work, the all-optical random speckle patterns should be stable at least excess the time of calibration and imaging.

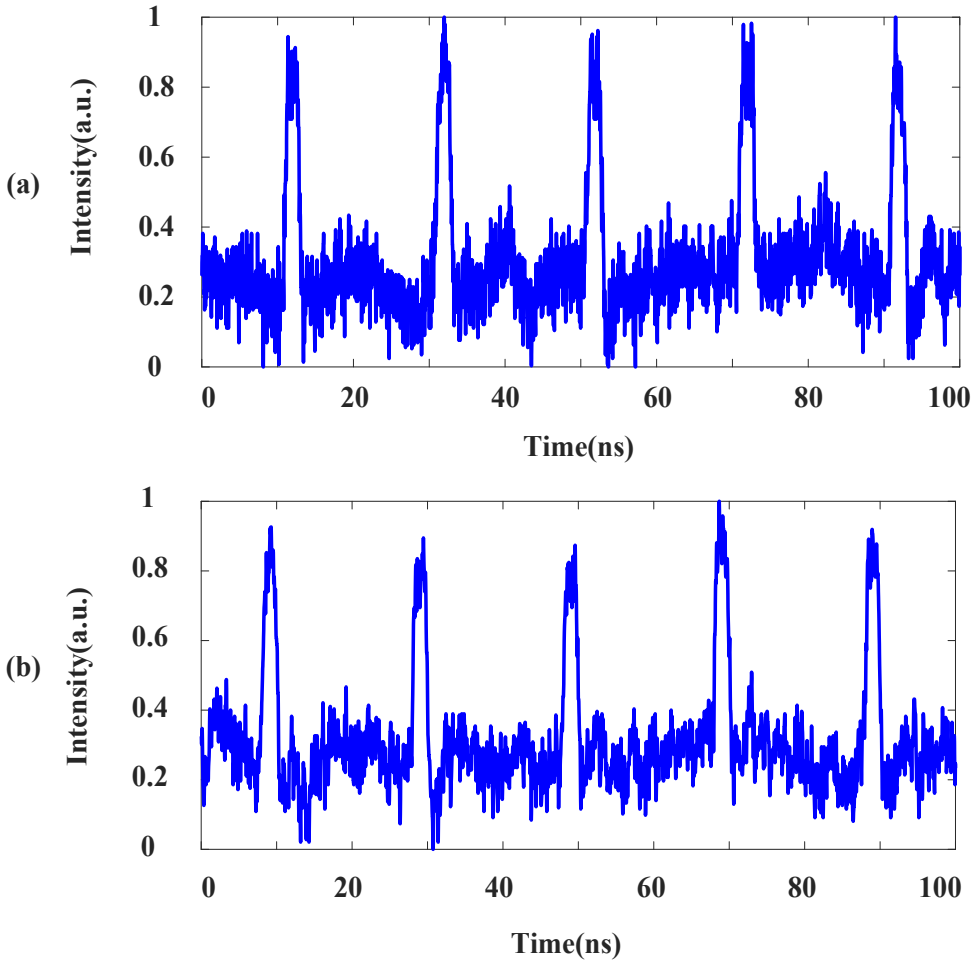

Figure 5.12 (a) Incident signal with a FWHM of 1.57ns ± 0.04ns; (b) output signal after MF with a FWHM of 1.60ns ± 0.05ns.

The mode dispersion [138–140] is also considered in our imaging system owning to the mode dispersion can temporally stretch the pulse when a single pixel PD is used to receive the final data. However, when carefully choose the length, core diameter, NA of the MMF and the coupling angle between the OL and MMF, the mode dispersion can be decreased, such as in our situation, a step-graded MMF with a length of 2m, core diameter 200μm, and 0.39 NA is employed. Figure 5. 12 (a) shows an original modulated single wavelength (1530nm) signal that propagating through MMF with a full width at half maximum (FWHM) of 1.57ns ± 0.04ns at a repetition of every 20ns, and Figure 5. 12 (b) shows the output signal that stretched via mode dispersion has a HWFM of 1.60 ± 0.05ns. In practical this effect might affect the experiment as there may have part of information overlapping between the two consecutive measurements (0.1ns division), while

in [23], a proposal that could solve 98% of overlapping between the two consecutive measurements and in theory this effect can be eliminated.

5.3. Summary

In this chapter, the CS and PTS based imaging systems using multimode interference are proposed and demonstrated for data compression.

Ultrafast optical imaging system using MMF for multimode interference based CS and PTS is presented conceptually with demonstration. MMF is regarded as an ultrafast all-optical random speckle pattern generator when combined with CS and PTS. This new conceptual all-optical random 2D speckle pattern generator has the advantage of low cost and large bandwidth. In comparison with traditional expensive and bandwidth-limited PRBS generator, our proposal is a perfect CS imaging method with low cost, ultrafast speed and inherently 2D CS imaging. For the other CS imaging systems that employed with SLM or DMDs, which have a maximum bandwidth tens of KHz due to the usage of electrical devices, our proposed imaging system has a bandwidth as high as 10 GHz, which is around 6 to 7 orders higher. Beside, by the implementation of PTS, our CS 2D imaging method can have a frame time the same as one pulse time, while the other CS-based imaging methods, such as in OCT or STEAM, need to repeat hundreds of times to get one frame. Thus our presented imaging system has an even higher bandwidth compared to the other time-domain CS-based imaging systems. To present the state-of-art of our imaging system, a combination of demonstration with computation and experiment is presented. The imaging data compression ratio from 35.11% to 68.59% is illustrated in CS approach and CCDs with same down-sized pixels are used to detect the target imaging to compare the effect of the CS approach. Also the FFT spatial resolution is analyzed according to the all-optical random speckle patterns and the result in our system is 42 × 42 pixels. The calibration of all-optical random speckle patterns is demonstrated in experiment. Besides, other elements that could affect the proposed imaging system, which

includes temporal stability of random optical pattern and mode dispersion of MMF, are investigated in our proposed system.

CHAPTER 6: CONCLUSION AND FUTURE WORK

6.1. Conclusions

The demanding of ultrafast speed of SPI system has motivated various imaging techniques with unprecedented speed, while the counter-part issues such as low efficiency, low stability, expensive equipment, large volume and big data are left behind.

The main conclusions of this thesis are as follows:

- A high efficient, low cost, diffraction limited and miniature SEI system using 45° TFG is presented. The 45° TFG, which is performed as the high efficient in-line diffractive grating, is computationally and experimentally confirmed to be the perfect target for undertaking uniform one-to-one mapping between space and wavelength. The performance of this SEI system is analyzed and this paved the way for potential PTS based ultrafast SEI system.

- A fibre-compatible, low cost, and diffraction limited PTS based ultrafast SEI system using 45° TFG is theoretically analysed and experimentally demonstrated. The resolution of the proposed system is investigated. 50 million frames per second imaging of fast moving object at 46 m/s with a field of view of 0.7 mm and diffraction-limited resolution of 42.5 μm has been experimentally demonstrated. This conceptually new in-fibre diffraction design opens the way towards cost-effective, compact and high-resolution imaging systems for high-throughput detection and measurement.

- A new approach for highly-efficient, compact and fibre compatible laser beam steering using an in-fibre diffraction grating has been proposed and experimentally demonstrated in an indoor free-space optical wireless communication system. The in-fibre diffraction grating, namely 45° TFG,

performs as wavelength-controlled mechanical-free laser beam steering device. The wavelength-dependent lateral scattering of 45° TFG is obtained due to the strongly tilted grating structure. Experimental result shows free-space transmission over 1.4 m serving three remote users with data rate of 9.6 Gbps per beam using 2.4 GHz bandwidth signals.

- A full-duplex indoor free-space optical wireless communication system is proposed and experimentally demonstrated for the first time using 45° TFG. Here 45° TFG functions as an in-fibre passive diffraction device for wavelength steered light emission and reception, which enables full-duplex optical wireless transmission. The unique advantages of using an in-fibre TFG device for beam steering include high diffraction efficiency, low cost, high stability and simplicity, compactness and inherent compatibility with existing fibre links. In a proof-of-concept experiment, free-space full-duplex transmission over 1.4 m with data rate of 12 Gbps per beam has been demonstrated using 2.4 GHz bandwidth signals.

- A novel spectrum-encoded and time-stretch (SETS) based CS imaging system using a spatial mask as the passive optical random pattern generator is proposed and experimentally demonstrated for the first time. This system can reduce the cost of the traditional ultrafast CS imaging system without compensating speed. As a proof-of-principle experiment, an 81 points line scanning of resolution target using 45 measurement is performed (compression ratio of 55.6%) in our proposed high speed CS imaging system.

- As joint work, data compression in high-throughput PTS based OCT has been analysed and experimentally demonstrated using CS method. A data compression ratio of 66% has been obtained in high-throughput OCT measurements with 1.51-MHz axial scan rate and sampling rate of 50 MS/s.

- A PTS based ultrafast SPI system using CS method is presented for the first time with the advantages of overcoming the trade-off between high cost and high speed / large bandwidth. This is made possible via stretching broadband pulse in MMF, thus an ultrafast low cost random optical speckle pattern generator is formed. The performance of MMF as all-optical random speckle

pattern generator is experimentally analysed. A 27 × 27 pixels image is reconstructed within 500 measurements is performed in our proposed imaging system. Also, the fast Fourier transform (FFT) spatial resolution, which is a combination of multiple Gaussians, is analyzed to be 42 × 42 pixels.

6.2. Future Work

Future work to improve the performance of PTS based ultrafast SPI systems are as follows.

- The polarization feature of 45° TFG can be utilized and explored to perform CS imaging based STEAM structure using a polarization modulator (PolM). The 45° TFG has a polarization dependent loss as high as ~40 dB due to the largely tilted structure. Hence, a highly efficient CS imaging based STEAM structure can be performed. The schematic diagram is shown in Figure 6.1.

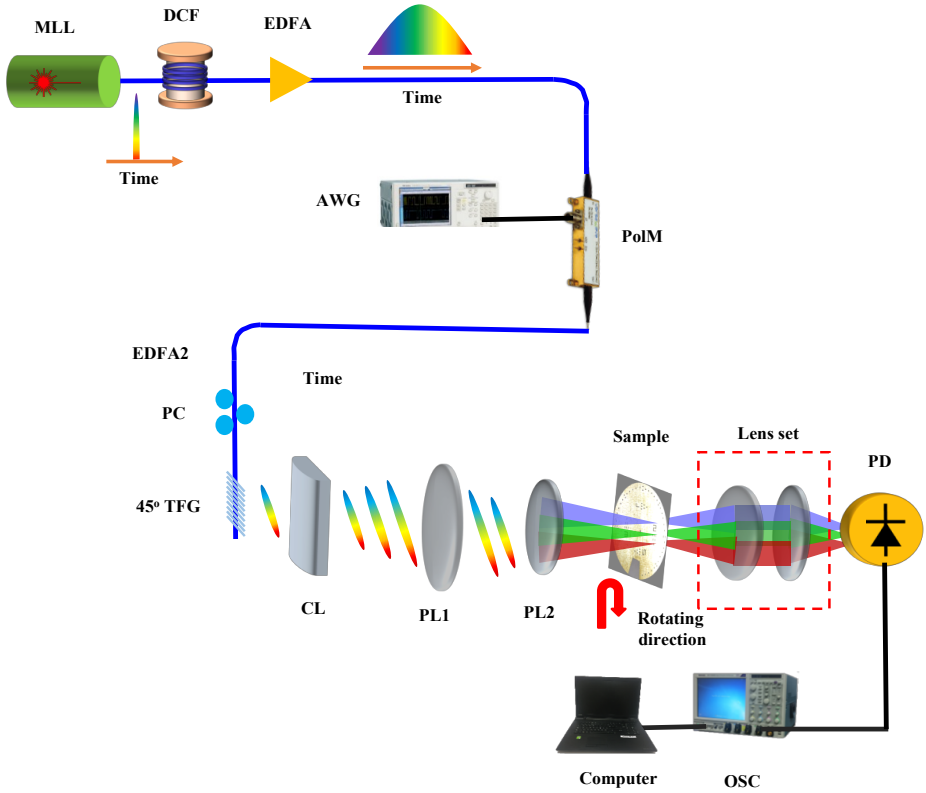

Figure 6.1 Schematic diagram of CS imaging based PTS and SEI using 45° TFG and PolM.

- An indoor free-space optical wireless communication system can be performed based the on polarization feature of 45° TFG for beam steering using a polarization modulator. As a polarization sensitive device, 45° TFG with polarization modulation in the wireless communication system is presented for the first time.The schematic diagram is shown in Figure 6.2.

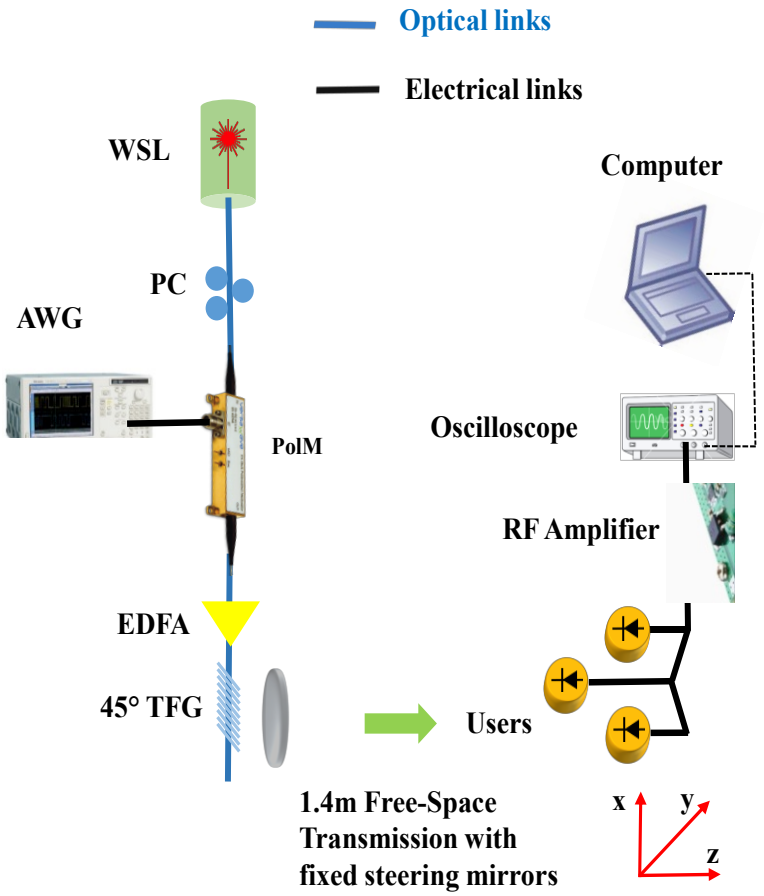

Figure 6.2 Schematic diagram of indoor free-space wireless communication system based on 45° TFG using PolM.

- Modal dispersion in MMF with imaging application have not been fully investigated. With proper alignment in the setup, the mode dispersion in MMF can be used to perform one-to-one mapping between wavelength / spectrum and time. Thus, a low cost chromatic dispersion device is achieved used MMF, substituting the traditional expensive DCF. Hence, a STEAM system is presented via the usage of low-cost MMF. The experimental setup of the proposed system is described in Figure 6.3.

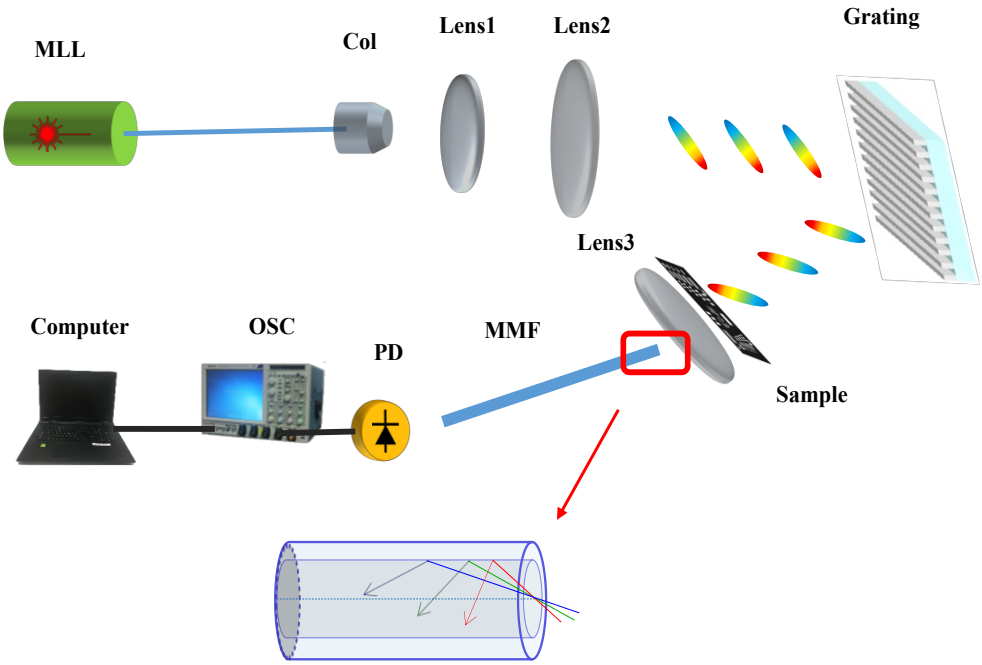

Figure 6.3 The experimental setup of PTS based ultrafast SEI system with MMF as the PTS device.

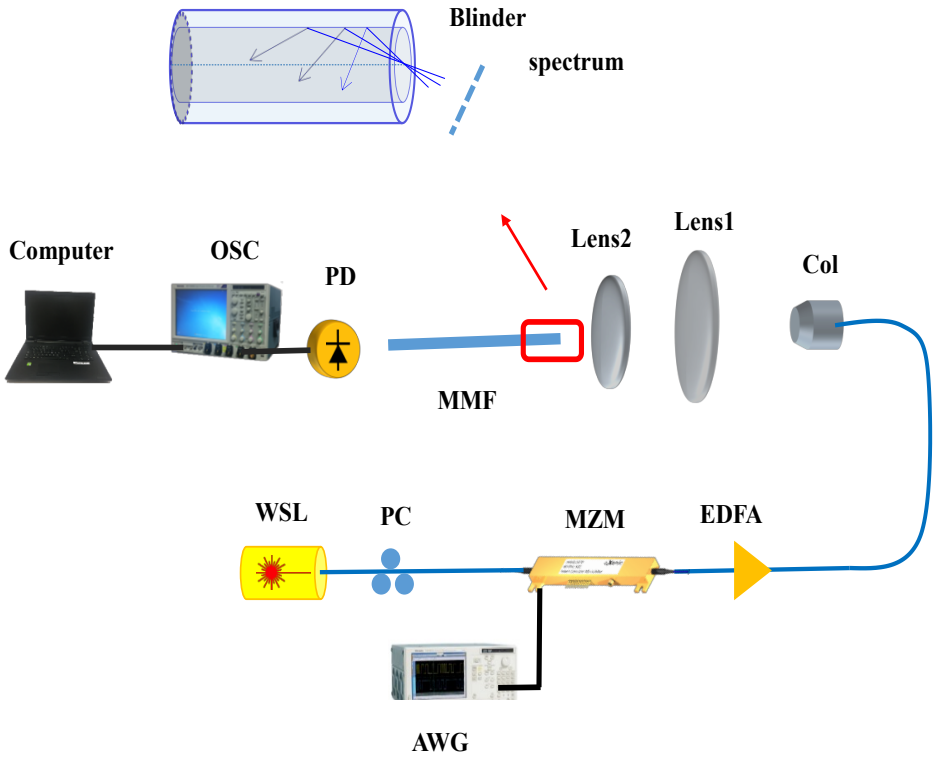

Figure 6.4 Principle diagram of single wavelength filter taper system using mode dispersion in MMF.

- Modal dispersion in MMF has different applications, one of it is used to make single wavelength filter taper. In such situation, the mode dispersion of MMF is utilized to build a low-cost, simplified filter tapper. The principle diagram of the system is depicted in Figure 6.4.

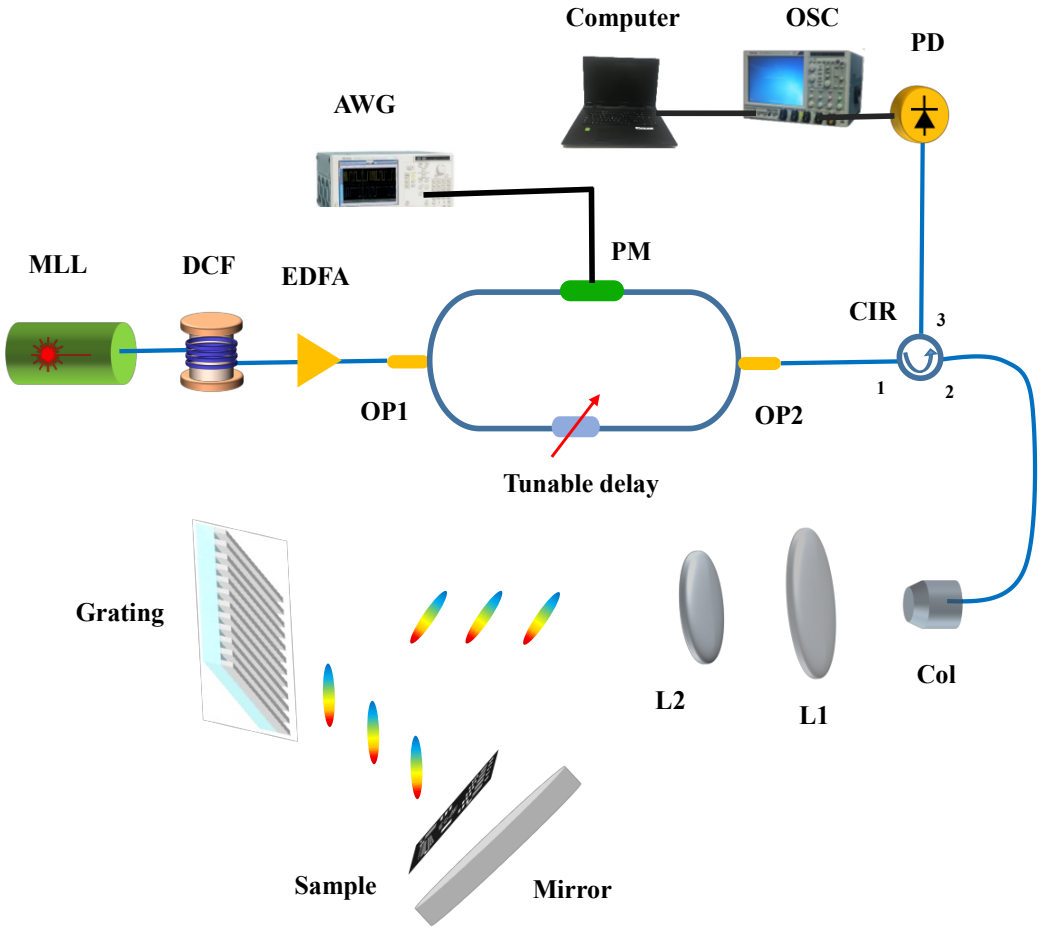

Figure 6.5 Scheme of novel CS imaging system based on 4 phase-shifting Fourier spectrum acquisition method.

- A SPI system based on Fourier spectrum acquisition using four-step phase-shifting method with the advantages of data compression can be explored with the combination of STEAM. This opens a new way of CS with new data compressed algorithm. The proposed system scheme is shown in Figure 6.5.

REFERENCE

1. Z. Zhang, X. Wang, G. Zheng, and J. Zhong, "Hadamard single-pixel imaging versus Fourier single-pixel," Sci. Rep. **25**, 19619–19639 (2017).

2. D. Huang, E. A. Swanson, C. P. Lin, J. S. Schuman, W. G. Stinson, W. Chang, M. R. Hee, T. Flotte, K. Gregory, C. A. Puliafito, A. Et, and et al., "Optical coherence tomography," Science (80). **254**, 1178–1181 (1991).

3. W. R.H., "Confocal optical microscopy," Rep. Prog. Phys **59**, 427–471 (1996).

4. T. I. L. L. M. Ohr, A. N. H. Erdt, and W. O. E. Lsässer, "2D tomographic terahertz imaging using a single pixel detector," Opt. Express **26**, 844–847 (2018).

5. B. Sun, S. S. Welsh, M. P. Edgar, J. H. Shapiro, and M. J. Padgett, "Normalized Ghost Imaging," Opt Express **20**, 16892–16901 (2012).

6. K. Goda, A. Mahjoubfar, C. Wang, A. Fard, J. Adam, D. R. Gossett, A. Ayazi, E. Sollier, O. Malik, E. Chen, Y. Liu, R. Brown, N. Sarkhosh, D. Di Carlo, and B. Jalali, "Hybrid Dispersion Laser Scanner," Sci. Rep. **2**, 445 (2012).

7. "https://www.pco.de/," .

8. M. F. Duarte, M. A. Davenport, D. Takhar, J. N. Laska, T. Sun, K. F. Kelly, and R. G. Baraniuk, "Single-Pixel Imaging via Compressive Sampling," IEEE Signal Process. Mag. **25**, 83–91 (2008).

9. Z. Zhang, X. Ma, and J. Zhong, "Single-pixel imaging by means of Fourier spectrum acquisition," Nat. Commun. **6**, 6225 (2015).

10. J. Shin, B. T. Bosworth, and M. A. Foster, "Single-pixel imaging using compressed sensing and wavelength-dependent scattering," Opt. Lett. **41**, 886–889 (2016).

11. G. Wang, C. Wang, Z. Yan, and L. Zhang, "Highly efficient spectrally encoded imaging using a 45° tilted fiber grating," Opt. Lett. **41**, 2398–2401

(2016).

12. G. Wang and C. Wang, "Diffraction Limited Optical Time-Stretch Microscopy Using an In-Fibre Diffraction Grating," Front. Opt. Sci. FF2A.5 (2016).

13. K. Goda and B. Jalali, "Dispersive Fourier transformation for fast continuous single-shot measurements," Nat. Photonics **7**, 102–112 (2013).

14. K. K. Tsia, K. Goda, D. Capewell, and B. Jalali, "Performance of serial time-encoded amplified microscope," Opt. Express **18**, 10016–10028 (2010).

15. B. Jalali, D. R. Solli, K. Goda, K. Tsia, and C. Ropers, "Real-time measurements, rare events and photon economics," Eur. Phys. J. Spec. Top. **185**, 145–157 (2010).

16. K. Goda, K. K. Tsia, and B. Jalali, "Serial time-encoded amplified imaging for real-time observation of fast dynamic phenomena," Nature **458**, 1145–1149 (2009).

17. K. Nakagawa, A. Iwasaki, Y. Oishi, R. Horisaki, A. Tsukamoto, A. Nakamura, K. Hirosawa, H. Liao, T. Ushida, K. Goda, F. Kannari, and I. Sakuma, "Sequentially timed all-optical mapping photography (STAMP)," Nat. Photonics **8**, 695–700 (2014).

18. G. J. Tearney, M. Shishkov, and B. E. Bouma, "Spectrally encoded miniature endoscopy," Opt. Lett. **27**, 412–414 (2002).

19. A. C. S. Chan, A. K. S. Lau, K. K. Y. Wong, E. Y. Lam, and K. K. Tsia, "Arbitrary two-dimensional spectrally encoded pattern generation—a new strategy for high-speed patterned illumination imaging," Optica **2**, 1037–1044 (2015).

20. K. Goda, K. K. Tsia, and B. Jalali, "Amplified dispersive Fourier-transform imaging for ultrafast displacement sensing and barcode reading," Appl. Phys. Lett. **93**, 131109 (2008).

21. G. Wang, Z. Yan, L. Yang, L. Zhang, and C. Wang, "Improved Resolution Optical Time Stretch Imaging Based on High Efficiency In-Fiber

Diffraction," Sci. Rep. **8**, 1–9 (2018).

22. Y. Wang, Q. Guo, H. Chen, M. Chen, S. Yang, and S. Xie, "Time-encoded structured illumination microscopy: toward ultrafast superresolution imaging," Opt. Lett. **41**, 3755 (2016).

23. C. Lei, Y. Wu, A. C. Sankaranarayanan, S. M. Chang, B. Guo, N. Sasaki, H. Kobayashi, C. W. Sun, Y. Ozeki, and K. Goda, "GHz optical time-stretch microscopy by compressive sensing," IEEE Photonics J. **9**, 3900308 (2017).

24. C. Lei, H. Chen, F. Xing, M. Chen, S. Yang, and S. Xie, "Time-stretch high-speed microscopic imaging system based on temporally and spectrally shaped amplified spontaneous emission," Opt. Lett. **40**, 946–949 (2015).

25. H. Chen, C. Lei, F. Xing, Z. Weng, M. Chen, S. Yang, and S. Xie, "Multiwavelength time-stretch imaging system," Opt. Lett. **39**, 2202–2205 (2014).

26. A. K. S. Lau, T. T. W. Wong, K. K. Y. Ho, M. T. H. Tang, A. C. S. Chan, X. Wei, E. Y. Lam, H. C. Shum, K. K. Y. Wong, and K. K. Tsia, "Interferometric time-stretch microscopy for ultrafast quantitative cellular and tissue imaging at 1 μ m," J. Biomed. Opt. **19**, 76001 (2014).

27. A. M. Fard, A. Mahjoubfar, K. Goda, D. R. Gossett, D. Di Carlo, and B. Jalali, "Nomarski serial time-encoded amplified microscopy for high-speed contrast-enhanced imaging of transparent media," Biomed. Opt. Express **2**, 3387–3392 (2011).

28. F. Xing, H. Chen, S. Xie, and J. Yao, "Ultrafast surface imaging with an increased spatial resolution based on polarization-division multiplexing," J. Light. Technol. **33**, 396–402 (2015).

29. B. Dai, D. Wang, Q. Wang, R. Hong, D. Zhang, S. Zhuang, and X. Wang, "Ultrafast three-dimensional imaging system based on phase-shifting method and hybrid dispersion laser scanning," IEEE Photonics J. **7**, 6900509 (2015).

30. F. Xing, H. Chen, C. Lei, Z. Weng, M. Chen, S. Yang, and S. Xie, "Serial wavelength division 1 GHz line-scan microscopic imaging," Photonics Res. **2**, B31 (2014).

31. S. Xiao and A. Weiner, "2-D wavelength demultiplexer with potential for >1000 channels in the C-band.," Opt. Express **12**, 2895–2902 (2004).

32. S. Xiao, A. M. Weiner, and C. Lin, "A dispersion law for virtually-imaged phased-array spectral dispersers based on paraxial-wave theory," IEEE J. Quantum Electron. **40**, 420–426 (2004).

33. D. Kang, B. E. Bouma, and G. J. Tearney, "Spectrally encoded imaging," FIO/LS FML6 (2011).

34. C. Palmer, *Diffraction Grating Handbook* (2005).

35. A. M. WEINER, *Ultrafast Optics* (2009).

36. M. H. Asghari and B. Jalali, "Anamorphic transformation and its application to time-bandwidth compression," Appl. Opt. **52**, 6735–6743 (2013).

37. F. Xing, H. Chen, M. Chen, S. Yang, H. Yu, and S. Xie, "World's fastest real-time line scan microscopic imaging system with 1GHz frame rate," CLEO - PR PD1b-2 (2013).

38. T. T. W. Wong, A. K. S. Lau, K. K. Y. Wong, and K. K. Tsia, "Optical time-stretch confocal microscopy at 1 μm," Opt. Lett. **37**, 3330–3332 (2012).

39. Q. Guo, H. Chen, Y. Wang, Y. Guo, P. Liu, X. Zhu, Z. Cheng, Z. Yu, S. Yang, M. Chen, and S. Xie, "High-Speed Compressive Microscopy of Flowing Cells Using Sinusoidal Illumination Patterns," IEEE Photonics J. **9**, (2017).

40. G. Meltz, W. Morey, and W. Glenn, "In-fiber Bragg grating tap," Opt. Fiber Commun. Conf. TUG1 (1990).

41. T. Erdogan and J. Sipe, "Tilted fiber phase gratings," J. Opt. Soc. Am. a-Optics Image Sci. Vis. **13**, 296–313 (1996).

42. K. O. Hill and G. Meltz, "Fiber Bragg Grating Technology Fundementals and Overview," IEEE J. Light. Technol. **15**, 1263–1276 (1997).

43. A.Kersey, M.Davis, H.Patrick, M.LeBlanc, and K.Koo, "Fiber grating Sensors," J. Light. Tech. **15**, 1442–1451 (1997).

44. C. Wang and J. Yao, "Fiber Bragg gratings for microwave photonics subsystems," Opt. Express **21**, 22868–22884 (2013).

45. Y. Zhao, Q. I. Wang, and H. E. Huang, "Characteristics and applications of tilted fiber Bragg gratings," J. Optoelectrics Adv. Mater. **12**, 2343–2354 (2010).

46. X. Dong, H. Zhang, B. Liu, and Y. Miao, "Tilted fiber bragg gratings: Principle and sensing applications," Photonic Sensors **1**, 6–30 (2011).

47. F. Liu, T. Guo, J. G. Liu, X. Y. Zhu, Y. Liu, B. O. Guan, and J. Albert, "High-sensitive and temperature-self-calibrated tilted fiber grating biological sensing probe," Chinese Sci. Bull. **58**, 2611–2615 (2013).

48. B. Jiang, K. Zhou, C. Wang, Y. Zhao, J. Zhao, and L. Zhang, "Temperature-calibrated high-precision refractometer using a tilted fiber Bragg grating," Opt. Express **25**, 25910–25918 (2017).

49. K. Zhou, L. Zhang, X. Chen, and I. Bennion, "Low thermal sensitivity grating devices based on ex-45° tilting structure capable of forward-propagating cladding modes coupling," J. Light. Technol. **24**, 5087–5094 (2006).

50. H. Qin, Z. Yan, Q. Sun, G. Wang, C. Wang, D. Liu, and L. Zhang, "Theoretical analysis of diffraction grating based on 45 ° -tilted fiber gratings," Proc. IEEE 1–2 (2017).

51. K. Zhou, X. Cheng, Z. Yan, A. Adedotun, and L. Zhang, "Optical Spectrum Analyzer using a 45-degree tilted fiber grating," Adv. Photonics Congr. BW2E.7 (2012).

52. Z. Yan, H. Wang, C. Wang, Z. Sun, G. Yin, K. Zhou, Y. Wang, W. Zhao, and L. Zhang, "Theoretical and experimental analysis of excessively tilted fiber gratings," Opt. Express **24**, 12107–12115 (2016).

53. Z. Y. An, Q. S. Un, C. W. Ang, Z. S. Un, C. M. Ou, K. Z. Hou, L. Iu, and L. Z. Hang, "Refractive index and temperature sensitivity characterization of excessively tilted fiber grating," Opt. Express **25**, 3819–3821 (2017).

54. J. Albert, L. Shao, and C. Caucheteur, "Tilted fiber Bragg grating sensors," Laser Photon. Rev. **7**, 83–108 (2013).

55. B. Zhou, A. P. Zhang, S. He, B. Gu, B. Zhou, and S. He, "Cladding-Mode-Recoupling-Based Tilted Fiber Bragg Grating Sensor With a Core-Diameter-Mismatched Fiber Section," IEEE Photonics J. **2**, 152–157 (2010).

56. C. S. Yongxing Jin, Xinyong Dong, Huaping Gong, "Refractive-index sensor based on tilted fiber Bragg grating interacting with multimode fiber," Microw. Opt. Technol. Lett. **52**, 1375–1377 (2010).

57. C. Chen and J. Albert, "Strain-optic coefficients of individual cladding modes of singlemode fibre theory and experiment," ELECTRONCS Lett. **42**, 1027–1028 (2006).

58. L. Y. Shao, L. Xiong, C. Chen, A. Laronche, and J. Albert, "Directional bend sensor based on re-grown tilted fiber bragg grating," J. Light. Technol. **28**, 2681–2687 (2010).

59. Y. Miao, B. Liu, and Q. Zhao, "Simultaneous measurement of strain and temperature using single tilted fibre Bragg grating," ELECTRONCS Lett. **44**, 1242–1243 (2008).

60. Y. M. Y. Miao, B. L. B. Liu, H. Z. H. Zhang, Y. L. Y. Li, H. Z. H. Zhou, H. S. H. Sun, W. Z. W. Zhang, and Q. Z. Q. Zhao, "Relative Humidity Sensor Based on Tilted Fiber Bragg Grating With Polyvinyl Alcohol Coating," IEEE Photonics Technol. Lett. **21**, 441–443 (2009).

61. T. Guo, H.-Y. Tam, P. a Krug, and J. Albert, "Reflective tilted fiber Bragg grating refractometer based on strong cladding to core recoupling.," Opt. Express **17**, 5736–5742 (2009).

62. F. Liu, T. Guo, C. Wu, B.-O. Guan, C. Lu, H.-Y. Tam, and J. Albert, "Wideband-adjustable reflection-suppressed rejection filters using chirped and tilted fiber gratings," Opt. Express **22**, 24430–24438 (2014).

63. H. S. Park, S. H. Yun, I. K. Hwang, S. B. Lee, and B. Y. Kim, "All-fiber add-drop wavelength-division multiplexer based on intermodal coupling," IEEE Photonics Technol. Lett. **13**, 460–462 (2001).

64. Z. Yan, K. Zhou, and L. Zhang, "In-fiber linear polarizer based on UV-inscribed 45° tilted grating in polarization maintaining fiber," Opt. Lett. **37**, 3819–3821 (2012).

65. Z. Yan, C. Mou, K. Zhou, X. Chen, and L. Zhang, "UV-inscription, polarization-dependant loss characteristics and applications of 45° tilted fiber gratings," J. Light. Technol. **29**, 2715–2724 (2011).

66. C. Mou, H. Wang, B. G. Bale, K. Zhou, L. Zhang, and I. Bennion, "All-fiber passively mode-locked femtosecond laser using a 45^{o}-tilted fiber grating polarization element.," Opt. Express **18**, 18906–18911 (2010).

67. C. Mou, K. Zhou, L. Zhang, and I. Bennion, "Characterization of 45°-tilted fiber grating and its polarization function in fiber ring laser," J. Opt. Soc. Am. B Opt. Phys. **26**, 1905–1911 (2009).

68. S. Remund, A. Bossen, X. Chen, L. Wang, A. Adebayo, L. Zhang, B. Považay, and C. Meier, "Cost-effective optical coherence tomography spectrometer based on a tilted fiber Bragg grating," SPIE BiOS **8938**, 89381E (2014).

69. G. Wang, C. Wang, Z. Yan, and L. Zhang, "A fiber-compatible spectrally encoded imaging system using a 45° tilted fiber grating," Proc. SPIE **9896**, 98960J (2016).

70. X. Chen, K. Zhou, L. Zhang, and I. Bennion, "In-fiber twist sensor based on a fiber Bragg grating with 81° tilted structure," IEEE Photonics Technol. Lett. **18**, 2596–2598 (2006).

71. S. Rui and et al., "In-fibre directional transverse loading sensor based on excessively tilted fibre Bragg gratings," Meas. Sci. Technol. **20**, 34015 (2009).

72. Z. Yan, Z. Sun, K. Zhou, B. Luo, J. Li, H. Wang, Y. Wang, W. Zhao, and L. Zhang, "Numerical and Experimental Analysis of Sensitivity-Enhanced RI Sensor Based on Ex-TFG in Thin Cladding Fiber," J. Light. Technol. **33**, 3023–3027 (2015).

73. B. Luo, Z. Yan, Z. Sun, Y. Liu, M. Zhao, and L. Zhang, "Biosensor based on

excessively tilted fiber grating in thin-cladding optical fiber for sensitive and selective detection of low glucose concentration," Opt. Express **23**, 32429–32440 (2015).

74. Z. Yan, C. Mou, Z. Sun, K. Zhou, H. Wang, Y. Wang, W. Zhao, and L. Zhang, "Hybrid tilted fiber grating based refractive index and liquid level sensing system," Opt. Commun. **351**, 144–148 (2015).

75. Y. Choi, C. Yoon, M. Kim, T. D. Yang, C. Fang-Yen, R. R. Dasari, K. J. Lee, and W. Choi, "Scanner-free and wide-field endoscopic imaging by using a single multimode optical fiber," Phys. Rev. Lett. **109**, 203901 (2012).

76. E. E. Morales-delgado, D. Psaltis, and C. Moser, "Two-photon imaging through a multimode fiber," Opt. Express **22**, 32158–32170 (2015).

77. R. N. Mahalati, R. Y. Gu, and J. M. Kahn, "Resolution limits for imaging through multi-mode fiber," Opt. Express **21**, 1656–1668 (2013).

78. T. Čižmár and K. Dholakia, "Shaping the light transmission through a multimode optical fibre: complex transformation analysis and applications in biophotonics," Opt. Express **19**, 18871–18884 (2011).

79. M. Plöschner, T. Tyc, and T. Čižmár, "Seeing through chaos in multimode fibres," Nat. Photonics **9**, 529–535 (2015).

80. D. Loterie, D. Psaltis, and C. Moser, "Bend translation in multimode fiber imaging," Opt. Express **25**, 6263–6273 (2017).

81. T. Čižmár and K. Dholakia, "Exploiting multimode waveguides for pure fibre-based imaging," Nat. Commun. **3**, 1027 (2012).

82. D. J. Richardson, J. M. Fini, and L. E. Nelson, "Space-division multiplexing in optical fibres," Nat. Photonics **7**, 354–362 (2013).

83. L. G. Wright, Z. Liu, D. A. Nolan, M.-J. Li, D. N. Christodoulides, and F. W. Wise, "Self-organized instability in graded-index multimode fibres," Nat. Photonics **10**, 771–776 (2016).

84. H. Frostig, E. Small, A. Daniel, P. Oulevey, S. Derevyanko, and Y. Silberberg, "Focusing light by wavefront shaping through disorder and

nonlinearity," Optica **4**, 1073–1079 (2017).

85. R. Florentin, V. Kermene, J. Benoist, A. Desfarges-Berthelemot, D. Pagnoux, A. Barthélémy, and J.-P. Huignard, "Shaping the light amplified in a multimode fiber," Light Sci. Appl. **6**, e16208 (2016).

86. L. G. Wright, D. N. Christodoulides, and F. W. Wise, "Controllable spatiotemporal nonlinear effects in multimode fibres," Nat. Photonics **9**, 306–310 (2015).

87. H. K. Chandrasekharan, F. Izdebski, I. Gris-Sánchez, N. Krstajić, R. Walker, H. L. Bridle, P. A. Dalgarno, W. N. MacPherson, R. K. Henderson, T. A. Birks, and R. R. Thomson, "Multiplexed single-mode wavelength-to-time mapping of multimode light," Nat. Commun. **8**, 14080 (2017).

88. D. Rontani, D. Choi, C.-Y. Chang, A. Locquet, and D. S. Citrin, "Compressive Sensing with Optical Chaos," Sci. Rep. **6**, 35206 (2016).

89. A. Liutkus, D. Martina, S. Popoff, G. Chardon, O. Katz, G. Lerosey, S. Gigan, L. Daudet, and I. Carron, "Imaging With Nature: Compressive Imaging Using a Multiply Scattering Medium," Sci. Rep. **4**, 5552 (2015).

90. Z. Zhu, H. Chi, T. Jin, S. Zheng, X. Jin, and X. Zhang, "Photonic compressive sensing for analog-to-information conversion with a delay-line based microwave photonic filter," Opt. Commun. **371**, 83–88 (2016).

91. G. C. Valley, G. A. Sefler, and T. J. Shaw, "Compressive sensing of sparse radio frequency signals using optical mixing," Opt. Lett. **37**, 4675–4677 (2012).

92. C. K. Mididoddi, F. Bai, G. Wang, J. Liu, S. Gibson, and C. Wang, "High-Throughput Photonic Time-Stretch Optical Coherence Tomography with Data Compression," IEEE Photonics J. **9**, 3901015 (2017).

93. X. Liu and J. U. Kang, "Compressive SD-OCT: the application of compressed sensing in spectral domain optical coherence tomography," Opt. Express **18**, 22010–22019 (2010).

94. E. Lebed, P. J. Mackenzie, M. V Sarunic, and M. F. Beg, "Rapid volumetric

OCT image acquisition using compressive sampling.," Opt. Express **18**, 21003–21012 (2010).

95. Q. Guo, H. Chen, M. Chen, S. Yang, and S. Xie, "Analysis of detection bandwidth limitations in time-stretch-based single-pixel imaging systems," Appl. Opt. **56**, 1327–1332 (2017).

96. Z. Zhu, H. Chi, T. Jin, S. Zheng, X. Jin, and X. Zhang, "Single-pixel imaging based on compressive sensing with spectral-domain optical mixing," Opt. Commun. **402**, 119–122 (2017).

97. B. T. Bosworth, J. R. Stroud, D. N. Tran, T. D. Tran, S. Chin, and M. A. Foster, "High-speed flow microscopy using compressed sensing with ultrafast laser pulses," Opt. Express **23**, 10521–10532 (2015).

98. Q. Guo, H. Chen, Z. Weng, M. Chen, S. Yang, and S. Xie, "Compressive sensing based high-speed time-stretch optical microscopy for two-dimensional image acquisition," Opt. Express **23**, 29639–29646 (2015).

99. B. T. Bosworth and M. A. Foster, "High-speed flow imaging utilizing spectral-encoding of ultrafast pulses and compressed sensing," Cleo ATh4P.3 (2014).

100. H. Chen, Z. Weng, Y. Liang, C. Lei, F. Xing, M. Chen, and S. Xie, "High speed single-pixel imaging via time domain compressive sampling," Cleo JTh2A.132 (2014).

101. J. Tropp, J. N. Laska, M. F. Duarte, J. K. Romberg, and R. G. Baraniuk, "Beyond Nyquist: Efficient sampling of bandlimited signals," IEEE Trans. Info. Theory **56**, 520–544 (2010).

102. Z. Zhu, H. Chi, S. Zheng, T. Jin, X. Jin, and X. Zhang, "Analysis of compressive sensing with optical mixing using a spatial light modulator," Appl. Opt. **54**, 1894–1899 (2015).

103. C. L. Chen, A. Mahjoubfar, and B. Jalali, "Optical data compression in time stretch imaging," PLoS One **10**, e0125106 (2015).

104. B. Jalali and M. H. Asghari, "The Anamorphic Stretch Transform: Putting

the Squeeze on “Big Data,”" Opt. Photonics News **25**, 24–31 (2014).

105. K. Zhou, G. Simpson, X. Chen, L. Zhang, and I. Bennion, "High extinction ratio in-fiber polarizers based on 45 ° tilted fiber Bragg gratings," Opt. Lett. **30**, 1285–1287 (2005).

106. "https://www.thorlabs.com/newgrouppage9.cfm?objectgroup_id=9026," .

107. J. Adam, A. Mahjoubfar, E. D. Diebold, B. W. Buckley, and B. Jalali, "Spectrally encoded angular light scattering," Opt. Express **21**, 28960–28967 (2013).

108. C. Zhang, Y. Xu, X. Wei, K. K. Tsia, and K. K. Y. Wong, "Time-stretch microscopy based on time-wavelength sequence reconstruction from wideband incoherent source," Appl. Phys. Lett. **105**, 41113 (2014).

109. T. T. W. Wong, A. K. S. Lau, K. K. Y. Ho, M. Y. H. Tang, J. D. F. Robles, X. Wei, A. C. S. Chan, A. H. L. Tang, E. Y. Lam, K. K. Y. Wong, G. C. F. Chan, H. C. Shum, and K. K. Tsia, "Asymmetric-detection time-stretch optical microscopy (ATOM) for ultrafast high-contrast cellular imaging in flow," Sci. Rep. **4**, 3656 (2015).

110. S. Cherry, "Edholm’s law of bandwidth," IEEE Spectr. **41**, 58–60 (2004).

111. H. Elgala, R. Mesleh, and H. Haas, "Indoor optical wireless communication: Potential and state-of-the-art," IEEE Commun. Mag. **49**, 56–62 (2011).

112. C. W. Oh, "Free-space transmission with passive two-dimensional beam steering for indoor optical wireless networks," Opt. Express **24**, 19211–19227 (2016).

113. C. Wang, "Dispersive Fourier Transformation for Versatile Microwave Photonics Applications," Photonics **1**, 586–612 (2014).

114. J. Xu, C. Zhang, J. Xu, K. K. Y. Wong, and K. K. Tsia, *Megahertz All-Optical Swept-Source Optical Coherence Tomography Based on Broadband Amplified Optical Time-Stretch* (2014), Vol. 39.

115. J. M. Nichols and F. Bucholtz, "Beating Nyquist with light: a compressively sampled photonic link," Opt. Express **19**, 7339–7348 (2011).

116. Y. Chen, H. Chi, T. Jin, S. Zheng, X. Jin, and X. Zhang, "Sub-Nyquist sampled analog-to-digital conversion based on photonic time stretch and compressive sensing with optical random mixing," J. Light. Technol. **31**, 3395–3401 (2013).

117. C. Wang and N. J. Gomes, "Photonics-enabled sub-Nyquist radio frequency sensing based on temporal channelization and compressive sensing," 2014 Int. Top. Meet. Microw. Photonics / 9th Asia-Pacific Microw. Photonics Conf. MWP/APMP 2014 - Proc. 335–338 (2014).

118. Y. Liang, M. Chen, H. Chen, C. Lei, P. Li, and S. Xie, "Photonic-assisted multi-channel compressive sampling based on effective time delay pattern," Opt. Express **21**, 25700–25707 (2013).

119. G. C. Valley, G. A. Sefler, and T. Justin Shaw, "Multimode waveguide speckle patterns for compressive sensing," Opt. Lett. **41**, 2529–2532 (2016).

120. K. Goda, A. Ayazi, D. R. Gossett, J. Sadasivam, C. K. Lonappan, E. Sollier, A. M. Fard, S. C. Hur, J. Adam, C. Murray, C. Wang, N. Brackbill, D. Di Carlo, and B. Jalali, "High-throughput single-microparticle imaging flow analyzer," Proc. Natl. Acad. Sci. **109**, 11630–11635 (2012).

121. A. Mahjoubfar, C. L. Chen, and B. Jalali, "Design of Warped Stretch Transform," Sci. Rep. **5**, 17148 (2015).

122. E. Candès and T. Tao, "Decoding by Linear Programming," IEEE Trans. Inf. Theory **51**, 4203–4215 (2005).

123. M. J. Marques, A. Bradu, and A. G. Podoleanu, "Towards simultaneous Talbot bands based optical coherence tomography and scanning laser ophthalmoscopy imaging," Biomed. Opt. Express **5**, 1428–1444 (2014).

124. J. Zhang, W. Jung, J. Nelson, and Z. Chen, "Full range polarization-sensitive Fourier domain optical coherence tomography.," Opt. Express **12**, 6033–6039 (2004).

125. M. Q. Tong, M. M. Hasan, S. S. Lee, M. R. Haque, D.-H. Kim, M. S. Islam, M. E. Adams, and B. H. Park, "OCT intensity and phase fluctuations correlated with activity-dependent neuronal calcium dynamics in the

Drosophila CNS [Invited]," Biomed. Opt. Express **8**, 726–735 (2017).

126. T. Klein and R. Huber, "High-speed OCT light sources and systems [Invited]," Biomed. Opt. Express **8**, 828–859 (2017).

127. K. V. Larin and D. D. Sampson, "Optical coherence elastography – OCT at work in tissue biomechanics [Invited]," Biomed. Opt. Express **8**, 1172–1202 (2017).

128. J. Stritzel, M. Rahlves, and B. Roth, "Refractive-index measurement and inverse correction using optical coherence tomography," Opt. Lett. **40**, 5558–5561 (2015).

129. P. Ossowski, A. Raiter-Smiljanic, A. Szkulmowska, D. Bukowska, M. Wiese, L. Derzsi, A. Eljaszewicz, P. Garstecki, and M. Wojtkowski, "Differentiation of morphotic elements in human blood using optical coherence tomography and a microfluidic setup," Opt. Express **23**, 27724–27738 (2015).

130. E. Bo, X. Liu, S. Chen, X. Yu, X. Wang, and L. Liu, "Spectral-domain optical coherence tomography with dual-balanced detection for auto-correlation artifacts reduction," Opt. Express **23**, 28050–28058 (2015).

131. R. Leitgeb, C. K. Hitzenberger, and A. Fercher, "Performance of fourier domain vs. time domain optical coherence tomography," Opt Express **11**, 889–894 (2003).

132. D. Choi, H. Hiro-Oka, H. Furukawa, R. Yoshimura, M. Nakanishi, K. Shimizu, and K. Ohbayashi, "Fourier domain optical coherence tomography using optical demultiplexers imaging at 60,000,000 lines/s.," Opt. Lett. **33**, 1318–1320 (2008).

133. A. G. Podoleanu and A. Bradu, "Master–slave interferometry for parallel spectral domain interferometry sensing and versatile 3D optical coherence tomography," Opt. Express **21**, 19324–19338 (2013).

134. S. Moon and D. Y. Kim, "Ultra-high-speed phase-sensitive optical coherence reflectometer with a stretched pulse supercontinuum source," Opt. Express **14**, 11575–11584 (2006).

135. K. Goda, A. Fard, O. Malik, G. Fu, A. Quach, and B. Jalali, "High-throughput optical coherence tomography at 800 nm," Opt. Express **20**, 19612–19617 (2012).

136. J. Xu, X. Wei, L. Yu, C. Zhang, J. Xu, K. K. Y. Wong, and K. K. Tsia, "High-performance multi-megahertz optical coherence tomography based on amplified optical time-stretch," Biomed. Opt. Express **6**, 1340–1350 (2015).

137. E. Candes, E. Candes, J. Romberg, and J. Romberg, "l1-magic : Recovery of Sparse Signals via Convex Programming," (2005).

138. E. D. Diebold, N. K. Hon, Z. Tan, J. Chou, T. Sienicki, C. Wang, and B. Jalali, "Giant tunable optical dispersion using chromo-modal excitation of a multimode waveguide," Opt. Express **19**, 23809–23817 (2011).

139. E. E. Morales-Delgado, S. Farahi, I. N. Papadopoulos, D. Psaltis, and C. Moser, "Delivery of focused short pulses through a multimode fiber," Opt. Express **23**, 9109–9120 (2015).

140. J. Sun, Z. Tan, T. Li, and M. Wang, "All-optical correlator based on modal dispersion in multimode fiber," Opt. Eng. **55**, 31119 (2015).

APPENDIX A

A.1 Image correlation

```
for i = 1:1:5
     str = int2str(i);
  str2 = '.jpg';
  s=strcat(str,str2);
  I(k,:,:) = rgb2gray(imread(s));
  k=k+1;
end

for j=1:4
   for jj=1:4
   temp1(:,:) = I(j,:,:);
   temp2(:,:) = I(jj,:,:);
  r(j,jj) = (corr2(temp1,temp2));
   end
end
```

A.2 Random pattern generation in SLM

```
a=randi([0 1],1,128);
  k=1;
  for j=1:length(a)
   aa(k:1:k+3)=a(j);
   k=k+4;
  end
```

```
  for i=1:512
   d(i,:)=aa;
  end

 imshow(d)
  filename = '71.xlsx';
xlswrite(filename,a,1,'')

 %Now make an RGB image that matches display from IMAGESC:
C = colormap;  % Get the figure's colormap.
L = size(C,1); % Scale the matrix to the range of the map.
ds = round(interp1(linspace(min(d(:)),max(d(:)),L),1:L,d));
H = reshape(C(ds,:),[size(ds) 3]); % Make RGB image from scaled.

 imwrite(H,'X:\p71.bmp','bmp');

% d, Say this is the given matrix:
subplot(1,2,1)
imagesc(d);
title('IMAGESC (MxN)')
% Now make an RGB image that matches display from IMAGESC:
C = colormap;  % Get the figure's colormap.
L = size(C,1); % Scale the matrix to the range of the map.
ds = round(interp1(linspace(min(d(:)),max(d(:)),L),1:L,d));
H = reshape(C(ds,:),[size(ds) 3]); % Make RGB image from scaled.
subplot(1,2,2)
image(H)  % Does this image match the other one?
title('IMAGE (MxNx3)')
imwrite(H,'X:\DVI_Matal.bmp','bmp');
```

A.3 Compressed sensing----imaging reconstruction

```
In=imread('Ma.bmp');
In = (rgb2gray(In));  % Converting Colour image to grayscale image

%load('matlab.mat');
x = double(In(:)); %Converts 2D data to 1D coloumn wise
 res = 10;
n = length(x);   %Calulates the length of total image
k = 1;
for i = 1:1:500   %for first set of wavelengths
    s3 = '1 (';
     s2 = int2str(i);
     s1 = ').png';
     s = strcat(s3,s2,s1);
     I=rgb2gray(imread(s));
 start_x=512-130;end_x=512+140-1;start_y=640-140;end_y=640+130-1;
I1_down = I(start_x:res:end_x,start_y:res:end_y);
I2 = I(start_x:10:end_x,start_y:10:end_y);
 %  I2 = im2bw(I2,0.5);
A1(k,:) = double(I1_down(:));
  %A1(k,:) = A1(k,:)*255/(max(A1(k,:))-min(A1(k,:)));
    A(k,:) = double(I2(:));                % Each radom pattern image is converted to
1D and is assigned a column
   k = k+1;
 %  imshow(I2);
end

y = A*x;% measurement matrix
Theta = zeros(k-1,n);          %Size same as matrix A
for ii = 1:n
  if (rem(ii,1000) == 0)
      ii
  end
    ek = zeros(1,n);
```

```
    ek(ii) = 1;
    psi = idct(ek)';
    Theta(:,ii) = A1*psi;
end

s2 = pinv(Theta)*y;%l2 norm solution
s1 = tveq_logbarrier(s2,Theta,Theta',y, 1e-1, 2, 1e-8, 600);

x1 = zeros(n,1);
for ii = 1:n
     if (rem(ii,1000) == 0)
     ii
  end
    ek = zeros(1,n);
    ek(ii) = 1;
    psi = idct(ek)';
    x1 = x1+psi*s1(ii);
end
 imagesc(reshape(x1,sqrt(n),sqrt(n)))%colormap gray

figure;
subplot(2,2,1);
B1=imresize(In,[22 22]);
imagesc(B1);
subplot(2,2,2);
B2=imresize(In,[16 16]);
imagesc(B2);
```

A.4 EVM Patch

```
b=[40 60 80 100];
a=[1 2 3 4 5 6];
```

```
c1=[11.53 10.35 10.18  10.57  17.75  10.9; 10.48  16.67  10.99  10.12  11.49  9.43;
16.55  10.85  10.96  10.99 9.18 9.27; 10.57  12.85  11.02  9.04  9.3  8.95];
c2=[12.1  10.18  10.51  10.64  8.97  9.6; 10.43  11.13  9.58  13.8  9.82  10.85; 11.91
9.94 9.84 9.63 9.24 8.78; 15.14 10.22 10.65 7.42 8.46 9.01];
d1=transpose(c1);
d2=transpose(c2);

figure;
width=0.3;
bar3(d1,width);
title('EVM at Different User Locations for different Antenna Separations');
%xlabel('Transmitter antenna separation');
ylabel('USER LOCATIONS');
zlabel('EVM %');
 set(gca,'yTickLabel',{'A';'B';'C';'D';'E';'F'});
 set(gca,'xTickLabel',{'40cm';'60cm';'80cm';'100cm'});

h=patch([0 5 5 0],[0 0 7 7],[12 12 12 12],'r');
h.FaceAlpha = .5;

figure;
width=0.3;
bar3(d2,width);
title('EVM at Different User Locations for different Antenna Separations');
%xlabel('Transmitter antenna separation');
ylabel('USER LOCATIONS');
zlabel('EVM %');
 set(gca,'yTickLabel',{'A';'B';'C';'D';'E';'F'});
 set(gca,'xTickLabel',{'40cm';'60cm';'80cm';'100cm'});

h=patch([0 5 5 0],[0 0 7 7],[12.5 12.5 12.5 12.5],'r');
h.FaceAlpha = .5;
```

A.5 Ultrafast imaging reconstruction

```
function [out_descript, outdata, timedata] = wfm_ascii_dpo(fname, data_start,
data_stop)

% Converts TSD5/6/7k and DPO7k/70k .wfm file to ASCII format with time array.
% data_start and data_stop input arguments are optional and can be used to read
parts of file
%To do: implement fast frame, pixel maps

out = [];
if nargin==0
   fname='';
end

if isempty(fname)
   [filename,pname]=uigetfile({'*.wfm', 'Tektronix Waveform Files (*.wfm)';'*.*',
'All Files (*.*)'},'Choose Tektronix WFM file');
   fname=[pname filename];
end

%---Open file
fd = fopen(fname,'r');
if fd==-1
   error('Problem opening file "%s"',fname)
end
 %---Determine byte ordering, then close and reopen with proper byte ordering
ByteOrder = fread(fd,1,'ushort');
if ByteOrder==61680
   fclose(fd);
   fd = fopen(fname,'r','ieee-be');
else
   fclose(fd);
```

```
    fd = fopen(fname,'r','ieee-le');
end

%---WFM static file information
out.ByteOrder             = fread(fd, 1,'ushort' );
out.VersionNum             = fread(fd, 8,'*char'  )';
if ~any(strcmp(out.VersionNum,{':WFM#001';':WFM#002';':WFM#003'}))
    fclose(fd);
    error('File "%s" is not a valid WFM file',fname)
end
out.NumDigitsInByteCount    = fread(fd, 1,'char'   );
out.NumBytesToEOF           = fread(fd, 1,'long'   );
out.NumBytesPerPoint        = fread(fd, 1,'char'   );
out.ByteOffsetToCurveBuffer = fread(fd, 1,'long'   );
out.HorZoomScale            = fread(fd, 1,'long'   );
out.HorZoomPos              = fread(fd, 1,'float32');
out.VerZoomScale            = fread(fd, 1,'double' );
out.VerZoomPos              = fread(fd, 1,'float32');
out.WaveformLabel           = fread(fd,32,'*char'  )';
out.N                    = fread(fd, 1,'ulong'  );
out.HeaderSize              = fread(fd, 1,'ushort' );

%---WFM header
out.SetType                 = fread(fd, 1,'int'    );
out.WfmCnt                  = fread(fd, 1,'ulong' );
jnk                      = fread(fd,36,'uchar' ); % Skip these for now
out.DataType                = fread(fd, 1,'int'    );
jnk                      = fread(fd,28,'uchar' ); % Skip these for now
switch out.VersionNum
case {':WFM#002' ':WFM#003'}
    jnk                  = fread(fd, 1,'ushort'); % Skip these for now
end
jnk                      = fread(fd,12,'uchar' ); % Skip these for now
```

```
%---Explicit Dimension 1/2
s = [];
for n=1:2
   s.DimScale            = fread(fd, 1,'double');
   s.DimOffset           = fread(fd, 1,'double');
   s.DimSize             = fread(fd, 1,'ulong' );
   s.Units               = fread(fd,20,'*char' );
   s.DimExtentMin        = fread(fd, 1,'double');
   s.DimExtentMax        = fread(fd, 1,'double');
   s.DimResolution       = fread(fd, 1,'double');
   s.DimRefPoint         = fread(fd, 1,'double');
   s.Format              = fread(fd, 1,'int'   );
   s.StorageType         = fread(fd, 1,'int'   );
   jnk                   = fread(fd,20,'uchar' ); % Skip these for now
   s.UserScale           = fread(fd, 1,'double');
   s.UserUnits           = fread(fd,20,'*char' );
   s.UserOffset          = fread(fd, 1,'double');
   switch out.VersionNum
   case ':WFM#003'
      s.PointDensity     = fread(fd, 1,'double');
   otherwise
      s.PointDensity     = fread(fd, 1,'ulong' );
   end
   s.HRef                = fread(fd, 1,'double');
   s.TrigDelay           = fread(fd, 1,'double');
   out.ExplicitDimension(n) = s;
end

%---Implicit Dimension 1/2
s=[];
for n=1:2
   s.DimScale            = fread(fd, 1,'double');
```

```
    s.DimOffset          = fread(fd, 1,'double');
    s.DimSize            = fread(fd, 1,'ulong' );
    s.Units              = fread(fd,20,'*char' )';
    jnk                  = fread(fd,16,'uchar' ); % Skip these for now
    s.DimResolution      = fread(fd, 1,'double');
    jnk                  = fread(fd,12,'uchar' ); % Skip these for now
    s.UserScale          = fread(fd, 1,'double');
    s.UserUnits          = fread(fd,20,'*char' );
    s.UserOffset         = fread(fd, 1,'double');
    switch out.VersionNum
    case ':WFM#003'
       s.PointDensity    = fread(fd, 1,'double');
    otherwise
       s.PointDensity    = fread(fd, 1,'ulong' );
    end
    s.HRef               = fread(fd, 1,'double');
    s.TrigDelay          = fread(fd, 1,'double');
    out.ImplicitDimension(n) = s;
end

%---Time Base 1/2 Information
s=[];
for n=1:2
    s.RealPointSpacing   = fread(fd, 1,'ulong' );
    s.Sweep              = fread(fd, 1,'int'   );
    s.TypeOfBase         = fread(fd, 1,'int'   );
    out.TimeBase(n) = s;
end

%---WFM Update Spec
jnk                  = fread(fd,24,'uchar'); % Skip these for now

%---WFM Curve Information
```

```
jnk                     = fread(fd,10,'uchar'); % Skip these for now
PrechargeStartOffset    = fread(fd, 1,'ulong');
DataStartOffset         = fread(fd, 1,'ulong');
PostchargeStartOffset   = fread(fd, 1,'ulong');
PostchargeStopOffset    = fread(fd, 1,'ulong');
EndOfCurveBufferOffset  = fread(fd, 1,'ulong');
 %---FastFrame Frames
%OPTIONAL

%---Curve Buffer
out.CurveSizeInBytes = PostchargeStartOffset - DataStartOffset;
out.CurveSize = out.CurveSizeInBytes / out.NumBytesPerPoint;
jnk = fread(fd,DataStartOffset,'uchar'); % Skip precharge
 if nargin<3
    data_start = 1;
    data_stop = out.CurveSize;
end
switch out.NumBytesPerPoint
    case 1
        if data_start > 1
        jnk = fread(fd,data_start-1,'*int8');
        out.CurveData = fread(fd,data_stop-data_start+1,'*int8');
        else
        out.CurveData = fread(fd,data_stop,'*int8');
        end
    case 2
        if data_start > 1
        out.CurveData = fread(fd,data_start-1,'*int16');
        out.CurveData = fread(fd,data_stop-data_start+1,'*int16');
        else
        out.CurveData = fread(fd,data_stop,'*int16');
        end
end
```

```
%---Close file
fclose(fd);
%E_DimOffset = out.ExplicitDimension(1,1).DimOffset;
%E_DimScale = out.ExplicitDimension(1,1).DimScale;
%E_CurveData = out.CurveData;
%I_DimOffset = out.ImplicitDimension(1,1).DimOffset
%I_DimScale = out.ImplicitDimension(1,1).DimScale

y = (out.ExplicitDimension(1,1).DimOffset) +
(out.ExplicitDimension(1,1).DimScale)*double(out.CurveData);
t = out.ImplicitDimension(1,1).DimOffset +
out.ImplicitDimension(1,1).DimScale*(data_start:data_stop);
out_descript.Fs = 1/out.ImplicitDimension(1,1).DimScale;
out_descript.Ts = out.ImplicitDimension(1,1).DimScale;
out_descript.N = out.CurveSize;
out_descript.byte = out.NumBytesPerPoint;
out_descript.fname = fname;
outdata = y;
timedata = t;
```

A.6 Lens focus simulation

```
% This program predicts the profile of a beam when the initial spot size
% and radius of curvature are given.
% initial conditions

% wavelength in vacuum
lambda = 1550e-9;

% input spot size and radius of curvature
w0 = 2e-3;
```

```
R0 = inf;
q0 = (1/R0 - i*lambda/(pi*w0^2))^(-1);

% lenses
f(1) = 75e-3
f(2) = -100e-3;
f(3) = 7e-3;

x = 250e-3;
y = 110e-3;

% distances
conversion = 25.4e-3;
d(1) = 20e-3;
d(2) = NaN;
d(3) = x;
d(4) = NaN;
d(5) = y;
d(6) = NaN;
d(7) = 20e-3;

% supply matrix elements
% M = [selection of channel, n1,n2, A,B,C,D]
% 1 = space element
% 2 = transition element

M1 = [1, 1,1, 1,d(1)/1,0,1];
M2 = [2, 1,1, 1,0,-1/f(1),1];
M3 = [1, 1,1, 1,d(3)/1,0,1];
M4 = [2, 1,1, 1,0,-1/f(2),1];
M5 = [1, 1,1, 1,d(5)/1,0,1];
M6 = [2, 1,1, 1,0,-1/f(3),1];
M7 = [1, 1,1, 1,d(7)/1,0,1];
```

```
M = [M1;M2;M3;M4;M5;M6;M7];

% calculate beam profiles and spot sizes
for k = 1:size(M,1)
    [q,w,x] = ABCD(lambda,M(k,:),d(k),q0);
    distance(k,:) = x;
    spotsize(k,:) = w;
    q0 = q(size(q,2));
    clear q w x
end

% (1) chain the distances and spotsizes
% (2) lens locations
[distance,spotsize,lens] = shift(M,distance,spotsize);

% unit conversions
conv1 = 1000;
conv2 = 1e3;
distance = distance*conv1;
spotsize = spotsize*conv2;

xmin = min(distance);
xmax = max(distance);
ymin = -1.1*max(spotsize);
ymax = 1.1*max(spotsize);

figure
 e1 = plot(distance,spotsize,distance,-spotsize);
hold on
e2 = plot(distance,lens);

set(e1,'LineWidth',1.5,'Color',[1 0 0]),
```

```
set(e2,'LineWidth',1.5,'Color',[0 0.3 1]),

xlabel('Distance (mm)'),
ylabel('Spot Size (mm)'),

% axis([300 xmax -0.2 0.2]),
axis([xmin xmax ymin ymax]),
grid

x = distance(end)
y = spotsize(end)
```